6-15-2017

Design, Synthesis and Characterization of Advanced Nanomaterials for Environmental and Energy Applications

Mohammad S. Seraji
University of Connecticut, mohammad.seraji@uconn.edu

Design, Synthesis and Characterization of Advanced Nanomaterials for Environmental and Energy Applications

Mohammad Saiful Islam Seraji, Ph. D.

University of Connecticut, 2017

The research work presented in this thesis is focused on design, synthesis, and characterization of transition metal oxide nanomaterials for environmental and energy applications. New synthetic techniques are designed and optimized for improved catalytic activity of the prepared materials over the conventional techniques. The nanomaterials were thoroughly characterized and used in various chemical reactions.

There are five chapters in this thesis. Chapter one provides background information and significance about four research projects presented in this thesis. Chapter two explains the catalyst design and single step synthesis of mesoporous sulfated zirconia using inverse micelle templated method for biodiesel production. This inverse micelle templated single step synthesis method for sulfated metal oxide solid acid is novel and provides high thermal stability and better catalytic activity than nonporous sulfated materials. Chapter three describes the synthesis of artificial antibody-like binding sites on silica nanoparticle using molecular imprinting technique. Human serum albumin (HSA) and glucose oxidase (GOx) proteins were used as templates to

Mohammad Saiful Islam Seraji, Ph. D.

University of Connecticut, 2017

prepare artificial antibodies. Our results showed that the template proteins, HAS and GOx, bind much more strongly to their respective artificial antibodies than other non-templated proteins. Chapter four discusses a facile synthesis of cobalt oxide/cobalt sulfide carbon (carbon nanotube or graphene oxide) hybrid material for electrocatalytic hydrogen production. Finally, chapter five suggests the mild transformation of mesoporous titanium dioxide (TiO_2) into black titanium dioxide nanomaterial with H_2/Ar under ambient pressure. Reduced of the prepared TiO_2 material also led to different colored TiO_2 (yellow, gray, black) depending on reaction time and temperature. The correlation between color, structure, and reactivity of these materials was presented in this chapter.

Design, Synthesis and Characterization of Advanced Nanomaterials for Environmental and Energy Applications

Mohammad Saiful Islam Seraji

B.Sc., University of Dhaka, 2006

M.Sc. University of Dhaka, 2008

A Dissertation

Submitted in Partial Fulfillment of the

Requirement for the Degree of

Doctor of Philosophy

University of Connecticut

2017

APPROVAL PAGE

Doctor of Philosophy Dissertation

Design, Synthesis and Characterization of Advanced Nanomaterials for Environmental and Energy Applications

Presented by

Mohammad Saiful Islam Seraji

Major Advisor _____

Steven L. Suib

Major Advisor _____

Amy R. Howell

Associate Advisor _____

Alfredo Angeles-Boza

University of Connecticut

2017

Dedicated to

My Family

ACKNOWLEDGEMENTS

First, I would like to express my sincere gratitude to my advisors Dr. Steven Suib and Dr. Amy Howell for their guidance, encouragements and continuous support throughout my graduate studies. They gave me immense opportunities to grow in other areas such as communication, administration, and leadership. I would also like to thank my associate advisors Dr. Alfredo Angeles-Boza, Dr. Jose Gascon and Dr. Fatma Selampinar for their advice, support, and encouragement during my whole graduate career.

I would like to express my thanks and gratitude to Mrs. Bonnie Suib for her consideration and hospitality. I am also very thankful to my colleagues and group members Drs. Altug Poyraz, Chung-Hao Kuo, Homer Genuino, Lakshitha Pahalagedara, Madhavi Pahalagedara, Sourav Biswas, Wenqiao Song, Curt Guild, Christian Malapit, Kaddy Camara for all their help and support. My appreciation also goes Mahbubur Shakil, Habiba Tasnim, Shanka Dissanayke, Biswanath Dutta, Junkai He, Tahereh Jafari, Andrew Meguerdician, Niluka Wasalanthanthri, Chandima Weerakkody, Yang Wu, Dave Kriz and all present & past group members of Suib and Howell groups.

I am grateful to the Department of Chemistry and Institute of Material Science, University of Connecticut and their employees for their support during my graduate studies. I would like to thank all teaching faculties and laboratory technicians in Chemistry, and Physics departments for their help and support during my teaching. I would also like to acknowledge the financial support of the United States Department of Energy, and the Department of Chemistry, Department of Physics and Graduate School of the University of Connecticut.

Finally, I would like to express my heartiest gratitude to my beautiful wife Tamanna Taznin, who has been very supportive and stood beside me during my graduate studies. Lastly, I especially thank my parents and my family for their sacrifice and continuous support throughout my life. Without their unconditional love and care, I would not be the person I am today.

Table of Contents

Chapter 1. Introduction

Chapter-2. Facile Synthesis of a Mesoporous Sulfated Zirconia: Efficient Heterogeneous Catalysis for Biodiesel Production

Chapter 3. Synthesis and Characterization of Silica Nanoparticle-Based Artificial Antibody-like Binding Sites Using Surface Molecular Imprinting

Chapter-4: Cobalt Oxide-Cobalt Sulfide/Carbon Hybrids as Efficient Bifunctional Electrocatalyst for Oxygen and Hydrogen Evolution Reaction

Chapter 5. Synthesis of Black Titania (TiO2) Nanomaterials for Visible Light Photocatalytic Activity

List of Figures

List of Schemes

List of Tables

CHAPTER 1. INTRODUCTION

1.1. Overview

Metal oxides represent a wide class of compounds, incorporating cationic metal ions and oxygen anions, arranged into various crystalline and amorphous forms. The properties of metal oxides are different based on their synthesis method, crystallinity, particle sizes etc. These oxides are being used as catalysts for various environmental and energy related applications. Metal oxides with nanometer length scales, also known as nanomaterials, have remarkably different properties from analogous bulk matter.[1] The focus of this work is to develop metal oxide based nanomaterials for environmental and energy related catalytic applications.

Transition metal oxide (TMO) materials have been widely studied materials in recent years because of their excellent catalytic abilities for various reactions. In addition, they are cost effective, abundant, and environmentally benign. These materials are stable in most gas and liquid phase reactions, and their physical and chemical properties are easily controllable through synthesis methods. Among transition metal oxides, mesoporous TMO materials have opened a new window in heterogeneous catalysis since the discovery of mesoporous materials by Mobil Company in 1992.[2] Enhancement of catalytic activity by tuning the intrinsic properties of mesoporous materials has become the most interesting field of research in past two decades. Tuning the size, shape, and volume of the pores, and different morphology of the materials has a significant effect on the catalytic activity. A significant number of research papers related to mesoporous materials have published for numerous applications, such as photocatalysis, biofuel production, sensors, batteries, and energy production.[3-7] However, controlling the mesoporosity

by facile synthesis, tunable properties for various applications, and overall designing of the mesoporous nanomaterials for different applications has remain challenging.

The synthesis of mesoporous materials using traditional sol-gel methods still suffers from several difficulties. Low crystallinity, thermal instability, mesostructure collapse, and the template removal step are the common limitations of synthesizing mesoporous materials with desired properties. To overcome these problems, a different approach by inverse micelle templated sol-gel synthesis of mesoporous materials has already been studied for a group of metal oxides. The group of these mesoporous materials are named as University of Connecticut (UCT) mesoporous materials, and they have been proven to have unique catalytic activities.[3,8-10] In this approach, zirconium oxide, sulfated zirconium oxide, titanium oxide materials have been studied in this thesis. The synthesized materials were applied for biodiesel synthesis and photocatalytic reactions which are presented in chapter 2 and chapter 5.

1.2. Background and significance

1.2.1. Mesoporous solid acid catalyst for biodiesel production

Historically, fossil fuels such as petroleum, coal and natural gas were main source of energy in transportation, industrial, and residential uses. However, fossil fuels are finite and have been shown to be harmful to the environment after extensive use. According to the U.S. Energy Information Administration, in 2015, about 81% of the total consumed energy came from fossil fuels (petroleum 36%, natural gas 29% and coal 16%).[11] Burning of these fossil fuels produces greenhouse gases with long-term consequences, such as acid rains, ozone layer depletion, and climate change. After electric power, transportation (about 28% of total energy consumption) is the second highest area of energy consumption.[2] Therefore, making an alternative renewable

energy source for transportation would reduce the dependency on fossil fuels and further decrease environmental pollution. Diesel synthesized from vegetable oil, also known as biodiesel, would offer a better substitute to petroleum diesel. However, the production cost needs to be decreased to make biodiesel a viable alternative.

The liquid green fuel, biodiesel (FAME, fatty acid methyl ester) is a transesterification product of long chain (C_{14} – C_{20}) fatty acid triglycerides and has similar properties to petroleum-based diesel, such as densities, viscosities and heating values. Hence, biodiesel can be used in existing diesel engines and can also be mixed with petroleum diesel in varying proportions.[12] In addition, biodiesel is biodegradable, non-toxic, has higher oxygen content by weight and has more burning efficiency than petro-diesel.[13,14] Moreover, biodiesel produces fewer greenhouse gases because of its closed CO_2 cycle; hence it reduces environmental pollution.

Various vegetable oils, such as canola oil, soybean oil or animal fats are used as the fatty acid triglyceride sources.[15] The stepwise processes of converting the fatty acid triglyceride to diglyceride and then monoglyceride are transesterification reactions,[16] which can be catalyzed by acid catalysts,[17] base catalysts[18], or enzyme catalysts.[19] Moreover, various alkali and alkaline earth metal oxides and hydroxides, as well as different layered materials,[13,20] are also being used as heterogeneous catalysts for biodiesel production.

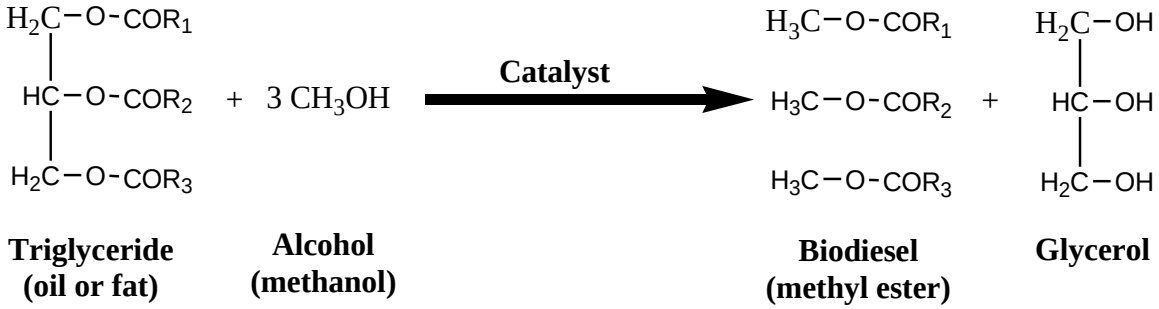

Scheme 1.1. Transesterification reaction of vegetable oil (modified from Leung et al.[15]).

Commercially, the most preferred catalysts are homogeneous base catalysts; among them potassium or sodium methoxide, sodium hydroxide, and potassium hydroxide are common.[21] However, the main disadvantage of a base catalysis is the side reaction of free fatty acids (FFA) in feedstock vegetable oil.

$$\text{R-COOH (aq)} + \text{NaOH (aq)} \rightarrow \text{R-COONa (aq)} + H_2O\ (l)$$

These free fatty acids react with base catalysts and form a side product which causes biodiesel separation to be more difficult and costly. Therefore, for base catalysts, the feed stock should be pure (less than 0.5% by weight, FFAs) or need to be pretreated to make it fatty acid free.[15,22,23] Sulfuric acid, hydrochloric acid, and aluminum chloride are well-known acid catalysts and struggle with slow reaction rates and high reaction temperatures, although they are tolerant to the free fatty acids of the vegetable oils. Zirconia, sulfated zirconia, and titania are well studied heterogeneous catalysts in biodiesel production because of their Brønsted and Lewis acid sites,[24,25] and they exhibit promising activities.[26,27] Hence, to overcome the existing problems in biodiesel production, acid catalysts with high surface area and high concentration of acid sites which can catalyze both esterification and transesterification reactions are needed.

The transesterification reaction can be catalyzed by both Brønsted and Lewis acid sites. A high concentration of acid sites is important for good turn-over. Strong Brønsted acid sites and weak Lewis acid sites can catalyze this reaction. The mechanism of transesterification reactions by heterogeneous Brønsted and Lewis acid catalysts is as follows:

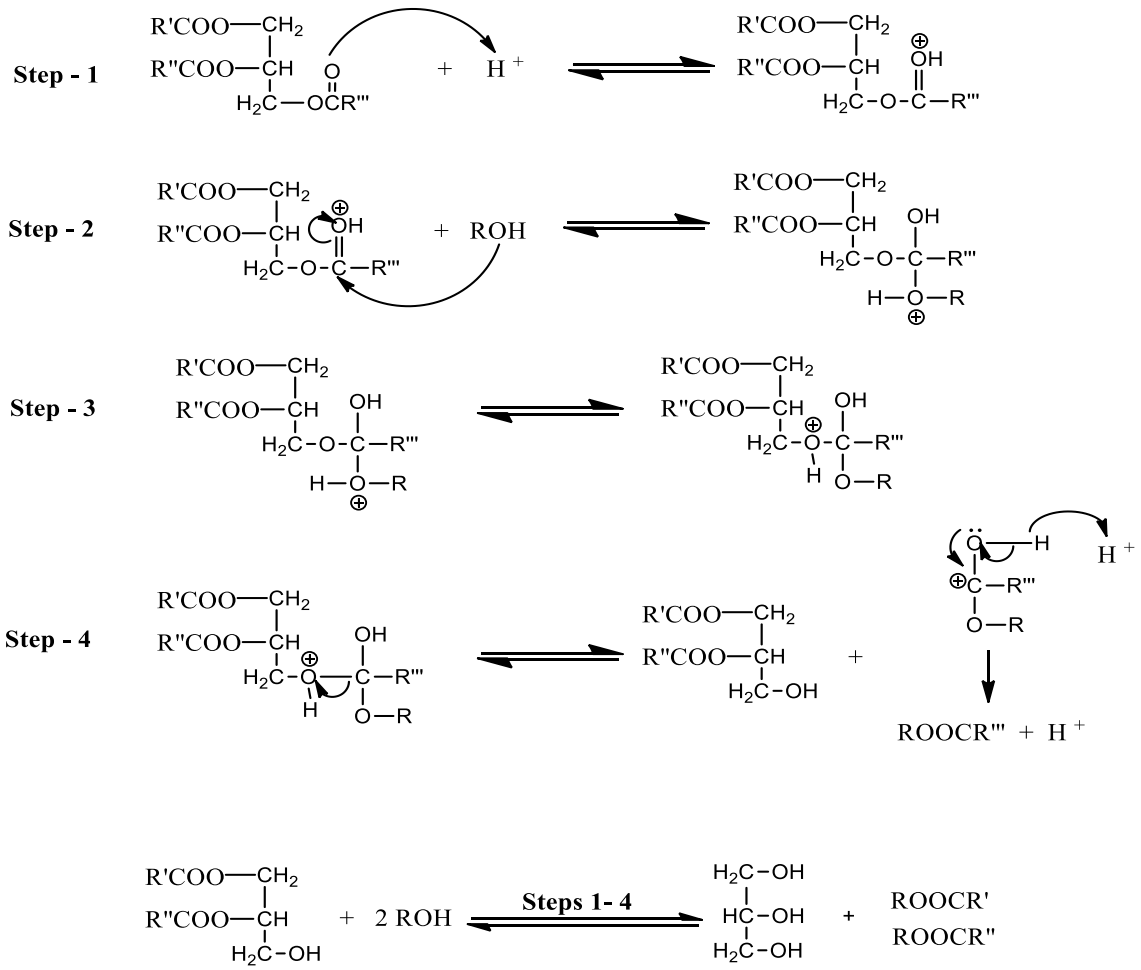

Scheme 1.2. Acid catalyzed transesterification reaction (modified from Schuchardt, et al.[28])

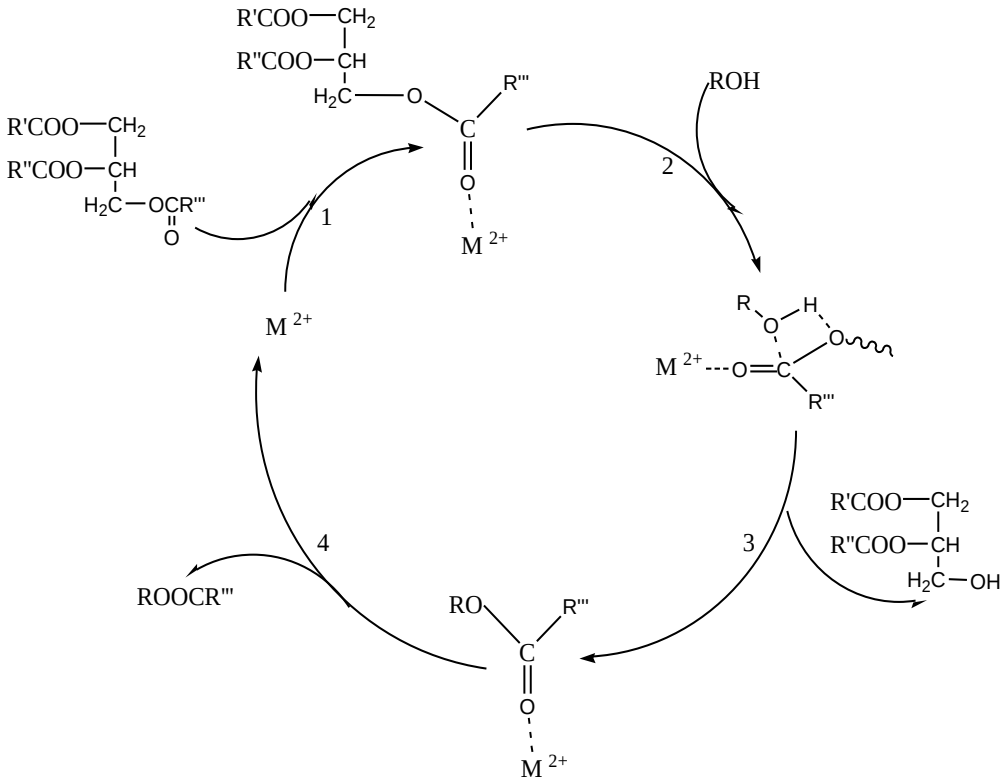

Scheme 1.3. Lewis acid catalyzed transesterification reaction (modified from Serio, et al.[22])

If the strength of the Lewis acid site is extremely high, the product desorption step (step 4) is not favored and results in a slower reaction rate. Brønsted acid sites are good for esterification, while Lewis acid sites are more active for transesterification.[22] The free fatty acids in the feedstocks will be catalyzed by Brønsted acid sites and the transesterification reaction of triglyceride will be catalyzed by both Brønsted and Lewis acid sites. In this work, sulfated mesoporous zirconia is proposed for biodiesel production. Sulfate groups play a dual role for this material: first, stabilizing the active tetragonal phase of zirconia and second, enhancing the number of acid sites.[29,30]

1.2.2. Artificial antibody by molecular imprinting

Molecular imprinting is a very important technique for synthesizing functional materials with template specific binding sites. Recently, this technique has aroused extensive attention in making artificial antibodies to replace natural antibodies for different applications.[31,32] In this method, binding sites of the specific molecule are made on the surface of the nanoparticle with the memory of the shape, size and functional groups of the template molecule.[33] We have synthesized antibody-like protein imprinted nanoparticles using different proteins as the template molecule.[34] The antibody-like nanoparticles were tested for binding affinity with different proteins and showed a higher binding affinity for the template protein. Artificial binding sites for human serum albumin (HSA) and glucose oxidase (GO) proteins were prepared on silica nanoparticles. First, the silica nanoparticles were functionalized with amine groups, the template protein was attached to the functionalized silica, and finally a mixture of four organosilanes was used to make the recognition site layer.

The selectivity of the prepared nanoparticles was tested for binding to human serum albumin (HSA), glucose oxidase (GO), bovine serum albumin (BSA), hemoglobin (Hb) and lysozyme. The results showed that the template proteins, HAS and GOx, bind much more strongly to their respective artificial antibodies than other proteins.

1.2.3. Nanomaterials for dye degradation and hydrogen production

TiO_2 nanomaterials have been recognized as one of the best photocatalysts because of their outstanding properties and promising applications in dye degradation, hydrogen generation, and environmental pollution removal.[35] The electronic bandgap of white TiO_2 is 3.0 – 3.2 eV,

which limits its optical absorption in the ultraviolet (UV) region.[36] However, the UV part is less than 5% in entire solar energy.[37] The photocatalytic activity of the material depends on the number of holes in the valence band and electrons in the conduction band, which are generated from the absorption process. Therefore, higher optical absorption can enhance photocatalytic activity. Modified TiO_2 can absorb light from the visible region and create more active charges on the surface of the material. TiO_2 can be modified by doping with metal or non-metal. Doping creates Ti^{3+} or oxygen vacancies, which reduce the bandgap of the TiO_2 and also changes the color of the white TiO_2 to yellow, blue, or gray. However, hydrogenation is an effective approach to shift the bandgap to around 1 – 1.5 eV and change the color of the material to black.[38]

TiO_2 can be reduced by hydrogen using different techniques, including hydrogen thermal technique, high or low pressure pure hydrogen treatment, hydrogen argon treatment, hydrogen nitrogen treatment, and hydrogen plasma.[39] However, most of the reduction processes are carried out at high temperatures and high pressures. Under these conditions, for porous materials, the main challenge is to retain the porosity during the hydrogenation process.[39,40] Mesoporous titanium dioxide material, synthesized by inverse micelle synthesis method (UCT material synthesis), shows visible light photocatalytic activity.[3] In this work, mesoporous UCT-TiO_2 nanomaterial has been synthesized and reduced with H_2/Ar under ambient pressure. The reduced material changed to different colors (yellow, gray) depending on reaction time and temperature.

Reference list

(1) Vayssieres, L. *Int. J. Nanotechnol.* **2004**, *1*, 1.

(2) Kresge, C.; Leonowicz, M.; Roth, W.; Vartuli, J.; Beck, J. *Nature* **1992**, *359*, 710.

(3) Luo, Z.; Poyraz, A. S.; Kuo, C.-H.; Miao, R.; Meng, Y.; Chen, S.-Y.; Jiang, T.; Wenos, C.; Suib, S. L. *Chem. Mater.* **2014**, *27*, 6.

(4) Stöcker, M. *Angew. Chem. Int. Ed.* **2008**, *47*, 9200.

(5) Ren, Y.; Ma, Z.; Bruce, P. G. *Chem. Soc. Rev.* **2012**, *41*, 4909.

(6) Jiao, F.; Bruce, P. G. *Adv. Mater.* **2007**, *19*, 657.

(7) Wang, G.; Liu, H.; Horvat, J.; Wang, B.; Qiao, S.; Park, J.; Ahn, H. *Chem. Eur. J.* **2010**, *16*, 11020.

(8) Poyraz, A. S.; Kuo, C.-H.; Biswas, S.; King'ondu, C. K.; Suib, S. L. *Nature commun.* **2013**, *4*.

(9) Song, W.; Poyraz, A. S.; Meng, Y.; Ren, Z.; Chen, S.-Y.; Suib, S. L. *Chem. Mater.* **2014**, *26*, 4629.

(10) Biswas, S.; Dutta, B.; Mullick, K.; Kuo, C.-H.; Poyraz, A. S.; Suib, S. L. *ACS Catal.* **2015**, *5*, 4394.

(11) Web of knowledge http://www.eia.gov/totalenergy/data/monthly/pdf/flow/css_2014_energy.pdf (Accessed November, 2015).

(12) Van Gerpen, J. *Fuel process. Technol.* **2005**, *86*, 1097.

(13) Zhang, Y.; Jin, L.; Sterling, K.; Luo, Z.; Jiang, T.; Miao, R.; Guild, C.; Suib, S. L. *Green Chem.* **2015**, *17*, 3600.

(14) Demirbas, A. *Energy Pol.* **2007**, *35*, 4661.

(15) Leung, D. Y.; Wu, X.; Leung, M. *Appl. Energ.* **2010**, *87*, 1083.

(16) Ma, F.; Hanna, M. A. *Bioresour. Technol.* **1999**, *70*, 1.

(17) Kiss, A. A.; Dimian, A. C.; Rothenberg, G. *Adv. Synth. Catal.* **2006**, *348*, 75.

(18) Keera, S.; El Sabagh, S.; Taman, A. *Fuel* **2011**, *90*, 42.

(19) Stamenković, O. S.; Lazić, M. L.; Veljković, V. B.; Skala, D. U. *Hem. Ind.* **2005**, *59*, 49.

(20) Jin, L.; Zhang, Y.; Dombrowski, J. P.; Chen, C.-H.; Pravatas, A.; Xu, L.; Perkins, C.; Suib, S. L. *Appl. Catal., B.* **2011**, *103*, 200.

(21) Kouzu, M.; Hidaka, J. S. *Fuel* **2012**, *93*, 1.

(22) Di Serio, M.; Tesser, R.; Pengmei, L.; Santacesaria, E. *Energy Fuels* **2007**, *22*, 207.

(23) Avhad, M.; Marchetti, J. *Renew. Sust. Energ. Rev.* **2015**, *50*, 696.

(24) Yaluris, G.; Larson, R.; Kobe, J.; Gonzalez, M.; Fogash, K.; Dumesic, J. *J. Catal.* **1996**, *158*, 336.

(25) Su, F.; Ma, L.; Song, D.; Zhang, X.; Guo, Y. *Green Chem.* **2013**, *15*, 885.

(26) Garcia, C. M.; Teixeira, S.; Marciniuk, L. L.; Schuchardt, U. *Bioresour. Technol.* **2008**, *99*, 6608.

(27) de Almeida, R. M.; Noda, L. K.; Gonçalves, N. S.; Meneghetti, S. M.; Meneghetti, M. R. *Appl. Catal., A.* **2008**, *347*, 100.

(28) Schuchardt, U.; Sercheli, R.; Vargas, R. M. *J. Braz. Chem. Soc.* **1998**, *9*, 199.

(29) Kuba, S.; Lukinskas, P.; Grasselli, R. K.; Gates, B. C.; Knözinger, H. *J. Catal.* **2003**, *216*, 353.

(30) Baertsch, C. D.; Komala, K. T.; Chua, Y.-H.; Iglesia, E. *J. Catal.* **2002**, *205*, 44.

(31) Yin, D.; Ulbricht, M. *J. Mater. Chem. B.* **2013**, *1*, 3209.

(32) Takeuchi, T.; Mori, T.; Kuwahara, A.; Ohta, T.; Oshita, A.; Sunayama, H.; Kitayama, Y.; Ooya, T. *Angew. Chem. Int. Ed.* **2014**, *53*, 12765.

(33) Chen, L.; Xu, S.; Li, J. *Chem. Soc. Rev.* **2011**, *40*, 2922.

(34) Bhakta, S.; Seraji, M. S. I.; Suib, S. L.; Rusling, J. F. *ACS Appl. Mater. Interfaces* **2015**, *7*, 28197.

(35) Pelaez, M.; Nolan, N. T.; Pillai, S. C.; Seery, M. K.; Falaras, P.; Kontos, A. G.; Dunlop, P. S.; Hamilton, J. W.; Byrne, J. A.; O'shea, K. *Appl. Catal. B: Environ.* **2012**, *125*, 331.

(36) Ma, Y.; Wang, X.; Jia, Y.; Chen, X.; Han, H.; Li, C. *Chem. Rev.* **2014**, *114*, 9987.

(37) Chen, X.; Burda, C. *J. Am. Chem. Soc.* **2008**, *130*, 5018.

(38) Chen, X.; Liu, L.; Peter, Y. Y.; Mao, S. S. *Science* **2011**, *331*, 746.

(39) Chen, X.; Liu, L.; Huang, F. *Chem. Soc. Rev.* **2015**, *44*, 1861.

(40) Zhou, W.; Li, W.; Wang, J.-Q.; Qu, Y.; Yang, Y.; Xie, Y.; Zhang, K.; Wang, L.; Fu, H.; Zhao, D. *J. Am. Chem. Soc.* **2014**, *136*, 9280.

CHAPTER-2. FACILE SYNTHESIS OF A MESOPOROUS SULFATED ZIRCONIA: EFFICIENT HETEROGENEOUS CATALYSIS FOR BIODIESEL PRODUCTION

2.1. Overview

Catalysis in biodiesel production enables the economical and environmentally friendly production of fuels for transportation and stationary applications. In this study, mesoporous sulfated zirconia (University of Connecticut (UCT) mesoporous materials, UCT-47) were produced by a single step inverse-micelle templated synthesis. The materials exhibit mesostructure stability up to 600 °C, while 10 mol % sulfate was required to stabilize tetragonal ZrO_2. Pore size could be tuned with sulfate loading (0-10 mol %) with higher Brønsted acidity also attained in the catalyst. Catalytic experiments were performed for microwave-assisted trans-esterification of canola oil with methanol between 100-160 °C with different methanol to oil ratios and catalyst loading. Microwave heating for 45 min at 145 °C and 5 wt% catalyst loading were found to be optimum conditions for 100% conversion to the corresponding fatty acid methyl ester (FAME).

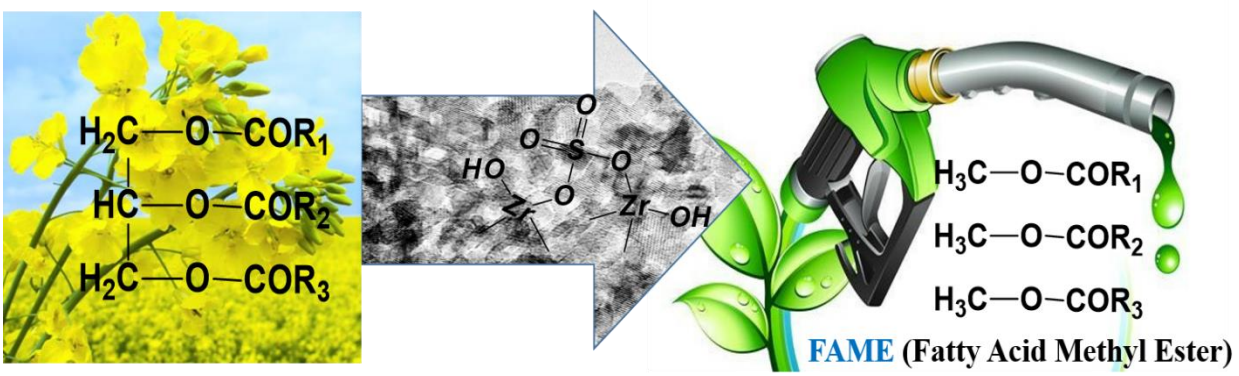

2.2. Background and significance

Liquid and gaseous petroleum-based hydrocarbons have been a primary source of energy for centuries. The world's growing energy demands, diminishing reserves and harmful environmental impacts of these fossil fuels have increased the urgency of identifying sustainable and renewable alternative energy sources.[1] Biodiesel, which is already recognized as a green fuel, can be a promising alternative energy source to substitute petroleum-based diesel in transportation.[2] Having similarity in chemical and physical properties, biodiesel can be used in conventional diesel engines without major modifications.[3] However, the challenges of inefficient existing catalysts, unwanted side reactions, and high production costs have hindered biodiesel becoming a mainstream alternative to fossil fuels.

Biodiesel is the fatty acid methyl ester produced by transesterification of vegetable oils using an acidic or basic catalyst. In industry, homogeneous, basic chemicals, namely NaOH and KOH, are widely used as catalysts because they promote fast reaction at low reaction temperatures.[4] Problematically, they react with free fatty acids of vegetable oils, which results in soap formation, and their use requires high product separation costs. A heterogeneous solid acid catalyst with strong acidic sites can solve these limitations and can reduce the overall production cost of biodiesel. Among various solid acid catalysts, sulfated zirconia has been an extensively studied material since its acidity was revealed by Hino and Arata.[5,6] Sulfated zirconia, a heterogeneous solid acid, is known to have excellent activity, easy separation and, more importantly, can improve the yield of fatty acid methyl ester (FAME) in the transesterification reaction.[7] Moreover, inducing porosity to the material can produce higher surface areas, better adsorption capacity and improve catalytic activity compared to nonporous alternatives.[8,9]

While various heterogeneous catalysts have been studied for biodiesel production, few have been used for direct transesterification of lipid feedstocks into biodiesel.[10,11] Most studies are done with model fatty acids, rather than direct use of commercially available vegetable oils.[12,13] The importance of this area of research can be assumed from the huge number of review articles explaining various aspects of different solid acid catalysts for biodiesel production.[4,14-17] Because of high activity, mesoporous sulfated zirconias have been synthesized by different research groups for various applications.[18-21] Chen and co-workers synthesized mesoporous sulfated zirconia for biodiesel production via esterification of fatty acids.[13] Garcia et al. synthesized sulfated zirconia by a solvent-free method and used this material for transesterification of soybean oil.[7] Sulfated zirconia is also being used as a solid acid catalyst for alkane isomerism, for sugar conversion, and in other acid catalyzed reactions.[22-27] Sulfated titania, other metal oxides, and layered materials are also being used as catalysts in biodiesel production.[28-32]

The types and strengths of the acidic sites of the sulfated zirconia are highly dependent on the synthetic approach. Most reported synthetic methods are two-step processes involving post-treatment of zirconia with a sulfating agent.[33,34] In typical synthesis processes, mesoporous zirconia is synthesized in the first step followed by sulfate impregnation in the second.[35] These chemical treatments can produce nonuniform wall thicknesses, as well as sulfates blocking the pores, which reduces the catalytic activity.[36,37] Many studies have developed syntheses of mesoporous zirconia with uniform porous structures by using different surfactants as structure directing agents. However, high-temperature calcination destroys delicate pore walls. The unique facet of UCT (University of Connecticut Mesoporous Materials) is that robust pores are formed through inter-particle voids.[38] A large variety of materials made by this method have drawn attention due to their high catalytic activity and tunable properties.[39-42] In this study, we

modified the typical synthesis process and here present a single-step route to mesoporous sulfated zirconia using sulfuric acid as a sulfating agent. As a result, the materials exhibit various types of acid sites and excellent catalytic activity for the transesterification of Canola oils, suggesting promise as active catalysts for biodiesel production.

2.3 Experimental

2.3.1 Catalyst synthesis

All reagents were purchased from Sigma-Aldrich and used as received. In a typical synthesis, 16.0 g (0.22 mol) of 1-butanol, 2.0 g (0.032 mol) of concentrated nitric acid and 10 g (0.02 mol) of zirconium butoxide were combined in a 150 mL beaker. To this 2.0 g (3.4×10^{-4} mol) of poly(ethylene glycol)-*block*-poly(propylene glycol)-*block*-poly(ethylene glycol), PEO_{20}-PPO_{70}-PEO_{20} (Pluronic P123, molar mass 5750 $gmol^{-1}$) was added, and the reaction mixture was stirred at room temperature to obtain a transparent gel. In another vial, a certain amount of concentrated sulfuric acid was diluted in 4 g of 1-butanol. The sulfuric acid amounts are 1, 3, 5, 7, and 10 mol % ($mol_{Sulfate}/mol_{Zirconia} \times 100$). The diluted acid was then added to the gel under vigorous magnetic stirring at room temperature. The mixture was stirred for 1 h and then placed in a ventilated oven at 120 °C for 5 to 6 h. The resulting material was ground in an agate mortar and calcined in a programmable oven at various temperatures (500°, 600°, and 700 °C) for 1 h with a heating rate of 1 °C/min. Catalysts were labeled as X% SZ-Y, where X was 1, 3, 5, 7, or 10 depending on the percent of the sulfate loading. SZ was sulfated zirconia, and Y stands for the calcination temperature. For example, 10% SZ-600 means 10 mol % sulfated zirconia sample calcined at 600 °C.

2.3.2 Characterization

Low-angle and wide-angle powder X-ray diffraction (PXRD) analyses were performed on a Rigaku Ultima IV diffractometer (Cu Kα radiation, λ = 1.5406 Å) with an operating voltage of 40 kV and a current of 44 mA. Low-angle PXRD were collected over a 2θ range of 0.5-8° with a continuous scan rate of 0.5° per minute. Wide-angle diffraction was collected from 5-75° 2θ with a continuous scan rate of 2° per minute. N_2 sorption studies were performed with a Quantachrome Autosorb-1-1C automated adsorption system. Samples were degassed at 250 °C for 6 h prior to the measurement. Surface areas were calculated using the Brunauer-Emmett-Teller (BET) method while pore size and volume were calculated using the Barrett-Joyner-Halenda (BJH) method. A Zeiss DSM 982 Gemini field emission scanning electron microscope (FE-SEM) with a Schottky emitter at an accelerating voltage of 2.0 kV and a beam current of 1.0 mA was used to determine the surface morphology of the materials. The samples were dispersed in ethanol and mounted on silica. High-resolution transmission electron microscopy (HR-TEM) studies were carried out on a JEOL 2010 transmission electron microscope with an accelerating voltage of 200 kV. Thermogravimetric analyses (TGA) were performed on a Hi-Res TA 2950 thermogravimetric analyzer with 60 mL/min air flow from 25 to 900 °C at a heating rate of 10 °C/min. Temperature programmed desorption (TPD) was performed in a tube furnace with a quadrupole MS residual gas analyzer (MKS eVision RGA). The catalyst (300 mg) was loaded into a quartz tube and then preheated in argon flow (20 mL/min) at 120 °C for 1.5 h to dry the catalyst. After the pretreatment, argon gas was passed at a flow rate of 10 mL/min as the sample was ramped from room temperature to 950 °C. The M/Z = 64 signal was followed to check the decomposition of sulfate ion to SO_2. Pyridine adsorption studies were done with 13 mm diameter self-supporting pellets. The pellets were cleaned in a tubular furnace at 200 °C for 1.5 h under

dry air flow. A 1 M pyridine solution in methanol was dropped on pellets, and physisorbed pyridine was removed in a tubular furnace running at 150 °C for 90 min under dry air flow. FTIR spectra of the pellets were collected using a Thermo Scientific Nicolet 8700 spectrometer equipped with an MCT/A detector. Sixty four scans were collected with a 4 cm^{-1} spectral resolution in the absorption mode. The number of catalytically available Brønsted acid sites was determined by a titration method, which involved an ion-exchange step between H^+ and Na^+ ions.[41,43] In a typical experiment, 160 mg of catalyst material was added to 10 mL of 3.4 M aqueous NaOH, and the mixture was stirred for 24 h at room temperature. The resultant liquid was filtered and titrated to pH 7 with an NaOH solution.[44] Concurrently the acidity of the materials was also determined by potentiometric titration methods.[45,46] The catalyst (100 mg) was added to 10 mL of acetonitrile and 100 µL amine, and the mixture was stirred for 3 h. Then the suspension was titrated with n-butylamine at a rate of 50 µL/min. The electrode potential variation was measured with a Corning 430 digital pH meter.

2.3.3 Catalytic reaction

Catalytic reactions were performed in a Biotage™ Initiator 2.5 microwave reactor. In a typical reaction, 2.24 mL of canola oil, 2.56 mL of methanol (1:1 mass ratio) and 5 wt% (200 mg) of catalyst were loaded in a 5 mL vial and were sealed with a PTFE lined cap. The reaction temperature and pressure were controlled during the experiment. After the reaction was finished, reaction mixtures were filtered, and the oil products were dissolved in THF and heptane. Product mixtures were analyzed by HP 5890 Series II gas chromatograph with a Restek Biodiesel TG column (14 m × 0.53 mm × 0.16 µm) coupled with a FID detector. The conversion and yield of FAME were calculated using the following equations:

$$\% \text{ Conversion} = \frac{(FAME + MG + DG)}{FAME+MG+DG+TG} \times 100\% \quad [1]$$

$$\% \text{ Yield of FAME} = \frac{FAME}{FAME + MG + DG + TG} \times 100\% \quad [2]$$

2.4. Results

2.4.1. Catalyst characterization

2.4.1.1. Powder Diffraction

Figure 1(A) shows low angle and Figure 1(B) shows wide angle X-ray diffraction patterns of different sulfated zirconia materials (X% SZ-600) calcined at 600 °C. The low angle diffraction lines (Figure 1A) indicate the mesostructure of these materials. The wide-angle PXRD pattern (Figure 1B) of 10% SZ indicates the tetragonal phase of zirconia (PDF card no. 01-081-1544), whereas all other materials (1%, 3%, 5%, and 7%) are cubic. The major cubic phase (111) peak has 2θ value at around 30.33°, while the major peak for the tetragonal phase (101) has the 2θ value at 30.18°, making their analysis difficult. Figure 1(C) is a comparison between the 1% and 10% SZ-600 samples, where we can see the peak around 35° split into two different peaks, and we can also see a similar pattern for the peak around 60° of the 2θ value (Figure 1D). This peak splitting starts at 7% sulfated material, which is cubic, then transitions to tetragonal with the 10% sulfated sample. Figure 2 (A) & (B) shows the detail peak splitting with different amounts of sulfate loading, while figure 2 (C) & (D) like figure 1 (C) & (D) are the comparison between 1% and 10% SZ samples around 35° and 60° of 2θ value.

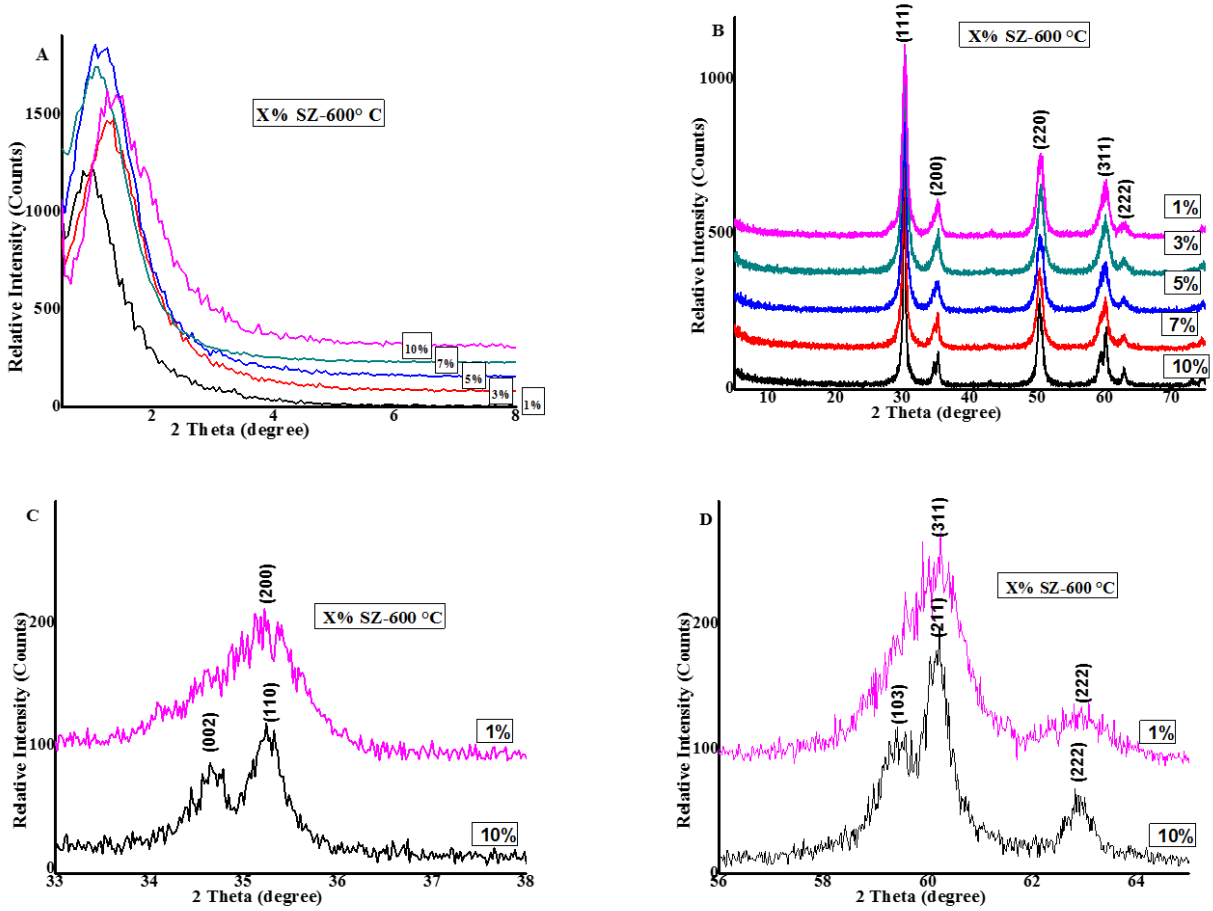

Figure 2.1. (A) Low angle (0.5° - 8°) PXRD patterns, (B) wide angle (5° - 75°) PXRD patterns of 1-10% SZ-600 samples. (C) & (D) are the comparisons of wide angel PXRD patterns between 1% and 10% SZ samples around 35° and 60° of 2θ value.

The 10% sulfated sample calcined at 500° and 700 °C also have a mixed cubic/tetragonal phase with the prominent crystal structure being cubic. Figure 3 (A) shows the wide angle PXRD pattern of 10% SZ-500 °C and 10% SZ-700 °C. X-ray analysis indicates the dominant cubic phase for both 10% SZ-500 °C (PDF card no. 01-089-9069) and 10% SZ-700 °C (PDF card no. 00-022-0540) materials.

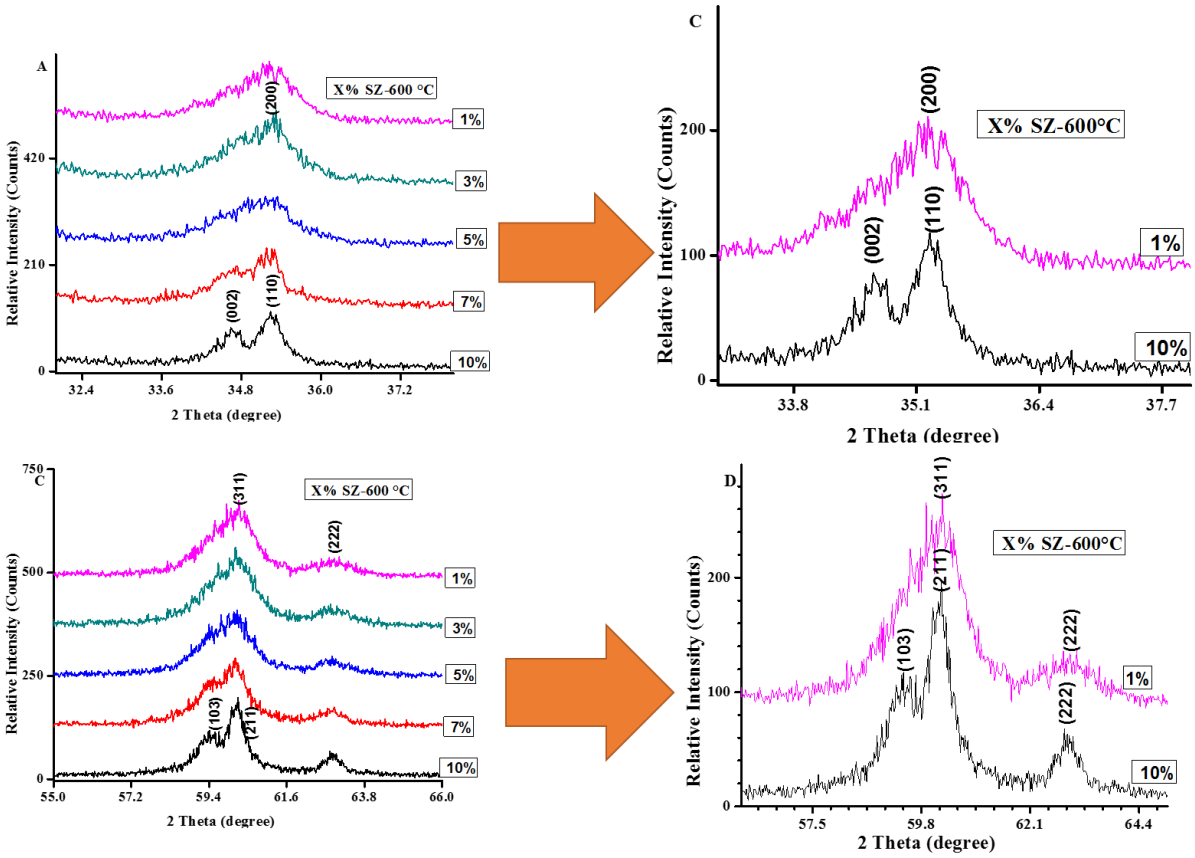

Figure 2.2. (A) & (B) are the wide angle PXRD patterns of 1-10% SZ-600 samples, showing how the peak splits with increasing sulfate amounts, and (C) & (D) are the comparisons of wide angel PXRD patterns between 1% and 10% SZ samples around 35° and 60° of 2θ value.

The low angle peak position varies with the different amounts of sulfate loading. With increasing sulfate loading the d values (inter-planer spacing) decrease. Figure 3 (B) indicates the change of inter-planer spacing with sulfate loading; with increasing sulfate loading the distance between planes decreases.

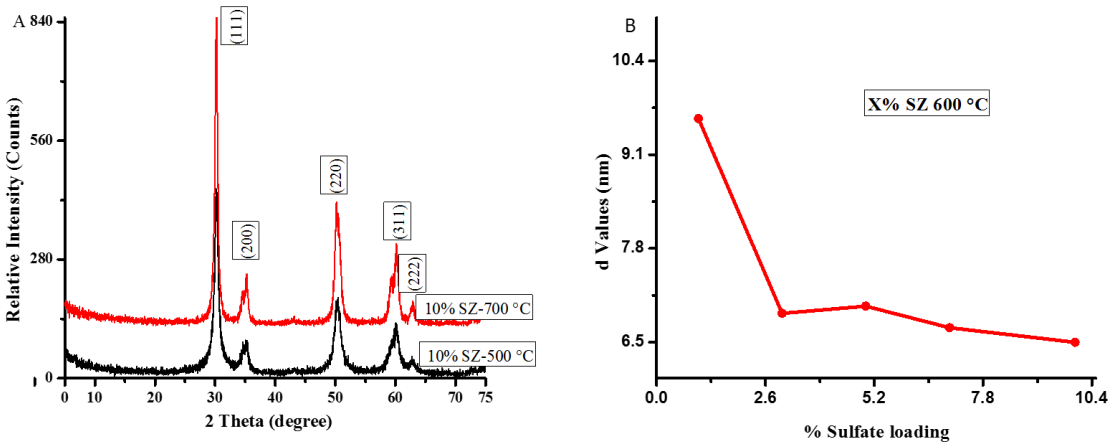

Figure 2.3. (A) Wide angle XRD patterns of 10% SZ samples calcined at 500° and 700 °C. (B) Change of inter-planer spacing (d values) with different sulfate amounts plot.

2.4.1.2. Microscopy

The morphological properties of the mesoporous sulfated zirconia materials were investigated by field emission scanning electron microscope (FE-SEM) and high resolution transmission electron microscopy (HR-TEM). In figure 4 (A-E), FE-SEM images of various sulfated zirconia materials (X% SZ-600, where X = 1 - 10) show very similar features with no distinguishable differences. Figure 4 (F) shows big chunks of a film-like material at lower magnification for the image of 10% SZ-600 material. Other materials also show a similar morphology at lower magnification.

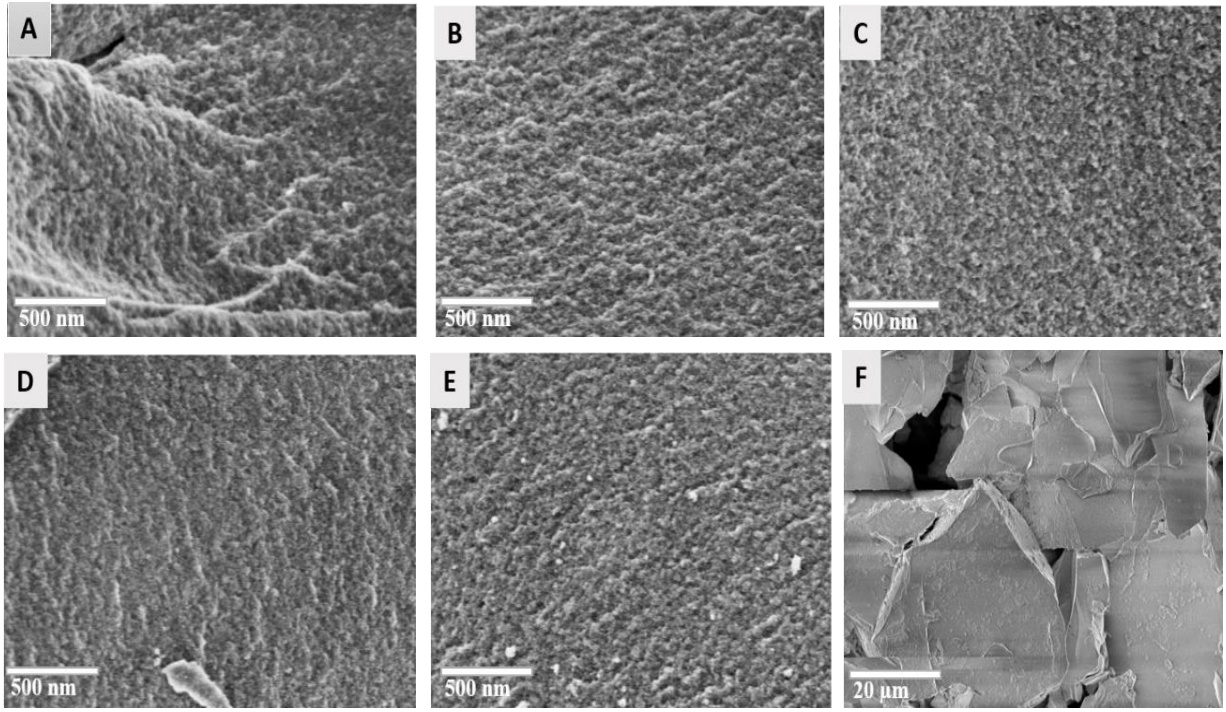

Figure 2.4. FE-SEM images of (A) 1% SZ-600, (B) 3% SZ-600, (C) 5% SZ-600, (D) 7% SZ-600 and (E) 10% SZ-600 materials. (F) FE-SEM image of as prepared 10% SZ-600 material before grinded.

HR-TEM images (Figure 5 A-B) show that aggregated nanoparticles form a porous network between the particles. A low-magnification image (Figure 5A) shows representative characteristics of UCT materials (aggregates of monodispersed particles). Fiure 5(B) shows a high resolution image of the material and indicates that the nanoparticles are crystalline. The lattice fringes of 0.3 nm can be indexed to the (111) crystal phase for cubic or (101) for the tetragonal phase of zirconia.

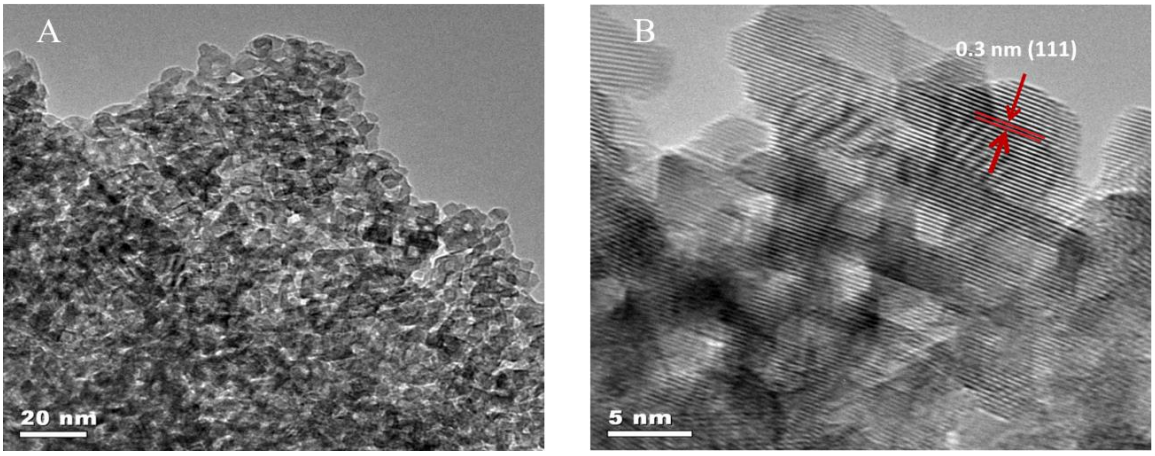

Figure 2.5. (A) Transmission electron microscopic (HR-TEM) image of 10% SZ-600 material at low magnification and (B) HR-TEM image of 10% SZ-600 material at high magnification.

2.4.1.3. Micromeritics and Textural Properties

N_2 adsorption and desorption isotherms in figure 6 (A) show a typical type IV adsorption isotherm along with a type I hysteresis loop, indicating the regular mesoporous structure of all the materials. The surface area of the materials ranges from 74 to 109 m^2g^{-1} while pore diameters are within the mesoporous range (3.4 to 2.2 nm). The surface area increases with increasing sulfate loading; the highest surface area (109 m^2g^{-1}) was obtained for 10% sulfate loading. There was no significant change in pore diameter for the 1%, 3%, and 5% sulfated samples, though pore diameter decreased for higher sulfate loading (7% and 10%).

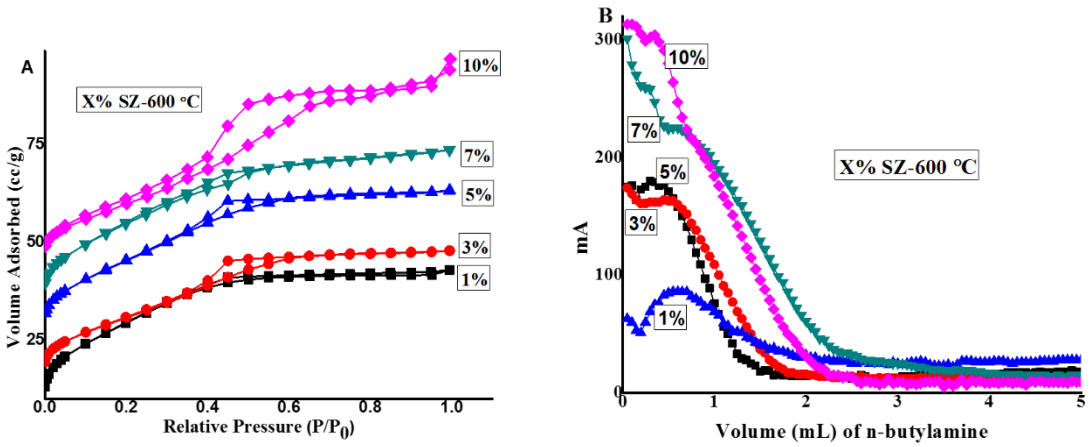

Figure 2.6. (A) Nitrogen sorption isotherm of different sulfated zirconia samples (X% SZ-600) and (B) Potentiometric titration of 1-10% SZ-600 samples.

Table 2.1. Structural parameters (surface area, pore size distribution) and the number of acidic sites of the mesoporous sulfated zirconia materials (X% SZ-600) calcined at 600 °C for 1h.

Materials (X% SZ-600)	BET surface area (m^2g^{-1})	BJH pore diameter (nm)	Acid sites (µmol/g) from potentiometric titration	Brønsted acid sites (µmol/g) from titration method
1% SZ-600	74	3.4	290	63
3% SZ-600	77	3.4	360	94
5% SZ-600	94	3.4	380	125
7% SZ-600	94	2.2	450	235
10% SZ-600	109	2.2	460	375

2.4.1.4. Acid sites

Potentiometric titrations with n-butylamine were performed to compare the relative strength and the number of acid sites of the synthesized materials. The first reading point of the electrode potential (E) of the titration is the maximum strength of the acid sites which is expressed in millivolts (mV). The number of acid sites of the material can be determined by the amount of base used (milliequivalents of titrant used per gram of solid), and the value is usually obtained from where the plateau is reached. The acid strength can be explained by the following scale reported by Pizzio et al. (2001) [45]: for very strong acid sites $E > 100$ mV; for strong acid sites $0 < E < 100$ mV; for weak sites $-100 < E < 0$ mV and for very weak acid sites $E < -100$ mV. Figure 6 (B) shows the neutralization profile of the acid sites present in the prepared materials by potentiometric titrations with n-butylamine. The figure indicates that a higher amount of sulfate ion incorporation correlates with increased acidity of the material. The 1% sulfated zirconia material has strong acid sites, whereas all other synthesized materials (3, 5, 7, and 10%) have very strong acid sites. The number of acid sites is also higher for the 7% and 10% sulfated samples compared to the 1%, 3%, and 5% sulfated zirconia samples.

Table 1 summarizes the number of Brønsted acid sites in the materials from titration methods. From the table, we can see the number of Brønsted acid sites increase significantly for the 7% and 10% SZ materials. We can also see the types and relative ratios of the acid sites for the 7% and 10% SZ materials by pyridine adsorption experiments, which is a widely used method for the characterization of different types of acid sites in solid acid materials.[20,41,47] Figure 7 shows the results of the pyridine experiments, the 7% and 10% SZ materials have significant number of Brønsted acid sites.

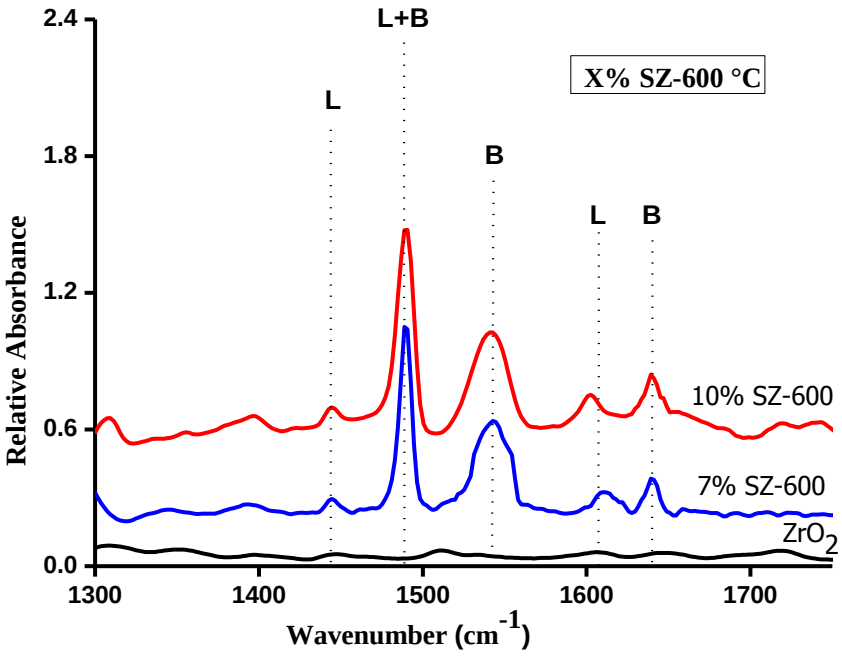

Figure 2.7. Pyridine adsorption study results for ZrO_2, 7% and 10% SZ-600 °C materials.

2.4.1.5. Thermal Characterization: Gravimetric and Desorption Experiments

The thermal stabilities of the materials were studied using thermogravimetric analysis (TGA). All the synthesized materials were heated from room temperature to 900 °C, and two characteristic weight loss bands were observed for most of the materials (Figure 8A). The first weight loss peak between 50° and 100 °C could be attributed to physisorbed water, and the second loss at ~800 °C is due to the decomposition of the sulfate group to sulfur dioxide. This was confirmed by temperature programmed desorption (TPD) experiments, showing SO_2 evolution by mass spectroscopy (Figure 8B).

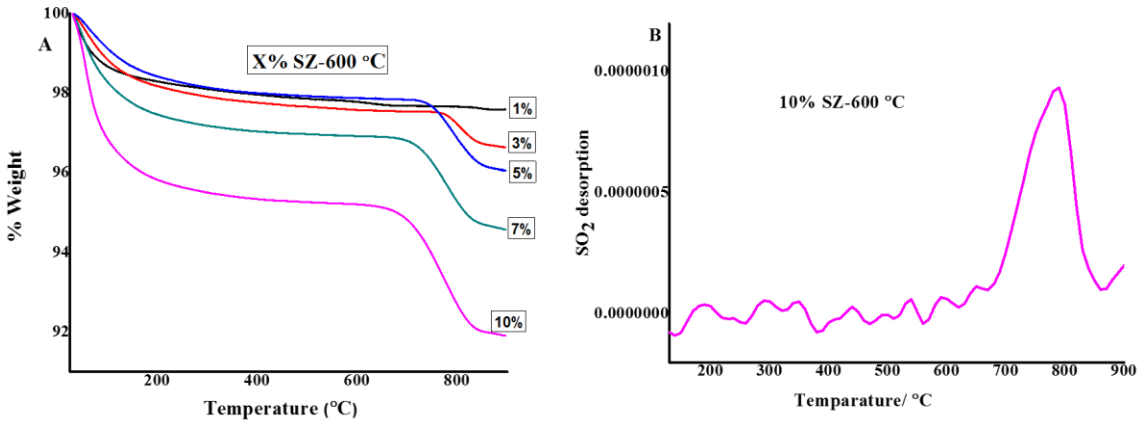

Figure 2.8. (A) TGA profile of different sulfated zirconia samples (X% SZ-600), and (B) TPD of 10% SZ-600 material.

2.4.2. Catalytic Study

The catalytic activity of the synthesized materials has been evaluated by the transesterification reaction of canola oil with methanol in the presence of the prepared catalysts (X% SZ-600). Figure 9 represents the relative conversion of triglyceride to diglyceride, monoglyceride and fatty acid methyl ester (FAME) with different materials. The 10% sulfated zirconia gives 100% conversion at 145 °C in 45 min, whereas the 1%, 3%, and 5% sulfated zirconia materials gave very low (below 10%) or no conversion. The reaction was run for different time and temperature variations. With 10% sulfated zirconia at 145 °C and 45 min, 100% conversion to fatty acid methyl ester (FAME, biodiesel) was obtained. Then, the other materials were also run under the same conditions, and 1%, 3%, and 5% sulfated materials gave mixtures of diglyceride and monoglyceride products. The 7% sulfated material gave a mixture of FAME and mono and diglycerides, while 10% SZ-600 gave only biodiesel (FAME). The equation for calculating conversion is given in the section 2.3.3.

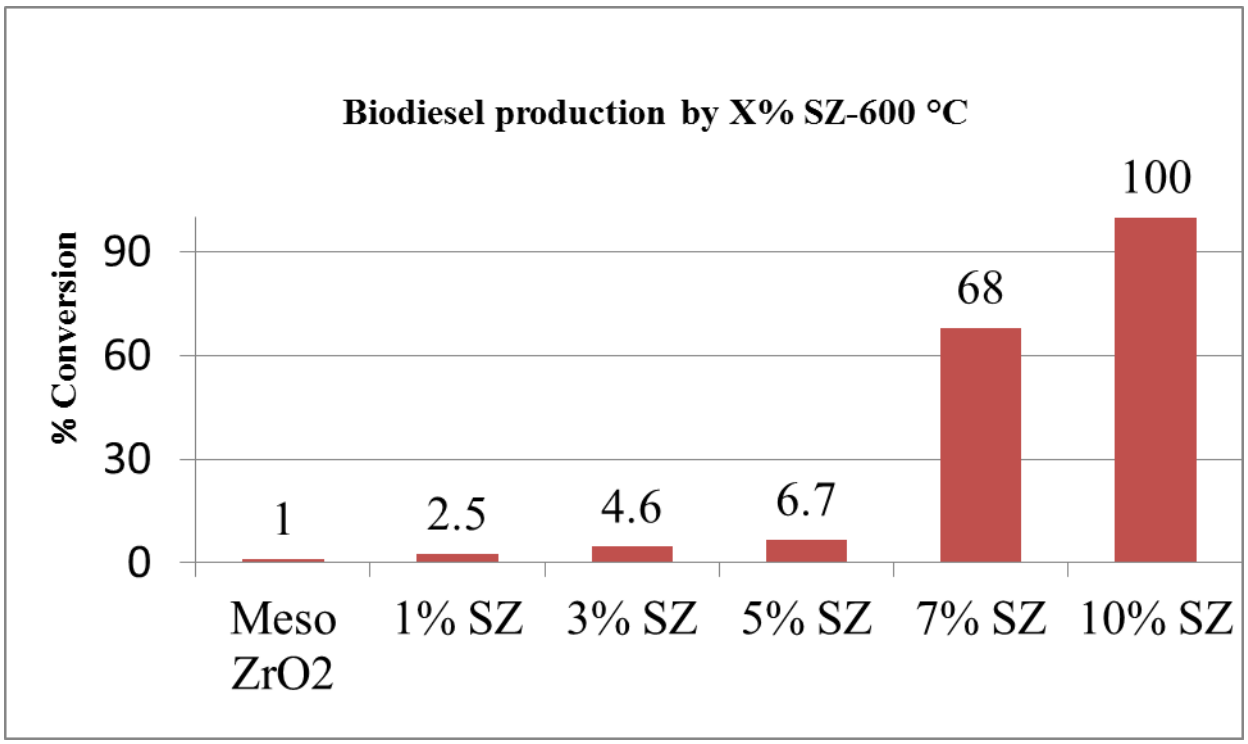

Figure 2.9. Relative conversions of canola oil to diglyceride, monoglyceride and fatty acid methyl ester (FAME) with different materials.

2.5. Discussion

In the sulfated zirconia solid acid catalyst system, the strength and distribution of the acidic sites are rather complex depending on the method of preparation and type of reactions. However, there is controversy in explaining the acidic properties of these materials. In this section, we would like to discuss some of the possible origins of the excellent catalytic behavior of sulfated zirconia for the transesterification reactions.

In this synthesis, metal precursors and other ionic sources are confined in inverse surfactant micelles, which then randomly pack to form mesoporous materials. The detailed mechanism of the formation of the UCT materials has been reported.[40] In this work, the sulfating agent (H_2SO_4), along with the metal precursors, is added during the synthesis, which

results in strong bonding of the surface sulfate group to the zirconia, rather than simple physical adsorption by the impregnation method. From the thermogravimetric analysis and temperature programmed desorption, the catalyst is stable up to 800 °C. Conversely, sulfate decomposes around 600°C in typical sulfated zirconia materials.[48] As the mesopores are created from interparticle voids, sulfate groups are expected inside the pores as well as expressed on the surface. From surface area data, pore diameters decrease with increasing sulfate content, suggesting incorporation of sulfate in the pores. This is supported by the shifting of low angle peak positions, where the higher sulfate contents lower the interplanar spacing (d values) of the materials and affect the mesostructure.

The tetragonal phase of zirconia is mentioned as the catalytically active phase of zirconia in the literature,[21,49] and the sulfate group is known to stabilize the metastable tetragonal phase at low temperature. However, the amount of sulfate required to stabilize the tetragonal phase has not been observed previously. In this study, at 600 °C, 10 mol % of sulfate can stabilize the active tetragonal phase of zirconia. The tetragonal phase of sulfated zirconia is an important factor for the formation of Brønsted acid sites in the material.[50] In the tetragonal phase of sulfated zirconia, there is a mixture of Lewis (zirconium center) and Brønsted acid sites, which are important for the transesterification of triglyceride molecules. In triglyceride molecules, there are three ester groups that are in close proximity, so a mixture of Lewis and Brønsted acid sites facilitates to complete the reactions and form three molecules of fatty acid methyl esters from one molecule of triglyceride. The 10% SZ-600 samples show the strongest activity among those studied. The relative amounts of two different types of acid sites were evaluated by pyridine adsorption studies, where both Lewis and Brønsted acid sites are present in the 10% SZ

and 7% SZ materials. In titration experiments, a significant amount of Brønsted acid sites in the 10% SZ material is observed.

The strength of the acid sites is another important parameter for the activity of the catalysts. The relative strength and amount of acid sites were investigated by amine titration experiments. Results showed an increasing trend in the acid strength with an increasing amount of sulfate groups. Sulfate groups are usually bonded to the Zr center through S-O-Zr bonds, whereas two other oxygens are bonded to the sulfur atoms. Oxygen being more electronegative pulls the bonding electron density towards itself and makes the zirconium center more positive and results in stronger Lewis acidic centers. The 7% SZ and 10% SZ samples have very strong acid sites compared to the other sulfated zirconia samples studied. As we have seen before, the active tetragonal phase started to form from the 7% SZ sample, and the tetragonal phase Brønsted acid centers are created along with Lewis acid centers. Therefore, the total number of acid sites are higher for the 7% SZ and 10% SZ materials, compared to the 1% SZ, 3% SZ, and 5% SZ materials. This higher number of strong acid sites make the 10% SZ-600 sample very active for biodiesel production.

2.6. Conclusion

Mesoporous sulfated zirconia was successfully synthesized by a single step inverse micelle templated method using sulfuric acid as the sulfating agent. Sulfuric acid (10 mol %) was needed to achieve the tetragonal phase of zirconia at 600 °C, while at lower amounts, mixed tetragonal/cubic materials were obtained. The 10% SZ material was found to have the highest number of strong acid sites among the synthesized materials and also demonstrated the highest activity (100% conversion in 45 min at 145 °C reaction temperature). The yields of biodiesel

were observed to be related to the crystal phase of the material, the amount of sulfate loading, and the strength of the acid sites. A facile single step synthesis, high activity in transesterification reaction, and strongly acidic nature establish UCT-47 material as a promising acid catalyst for biodiesel production.

Reference list

(1) Georgianna, D. R.; Mayfield, S. P. *Nature* **2012**, *488*, 329.

(2) Demirbas, A. *Biodiesel*, Springer London, 2008.

(3) Cheng, J. J.; Timilsina, G. R. *Renew. Energy* **2011**, *36*, 3541.

(4) Mardhiah, H. H.; Ong, H. C.; Masjuki, H.; Lim, S.; Lee, H. *Renew. Sust. Energ. Rev.* **2017**, *67*, 1225.

(5) Hino, M.; Kobayashi, S.; Arata, K. *J. Am. Chem. Soc.* **1979**, *101*, 6439.

(6) Song, X.; Sayari, A. *Catal. Rev.* **1996**, *38*, 329.

(7) Garcia, C. M.; Teixeira, S.; Marciniuk, L. L.; Schuchardt, U. *Bioresour. Technol.* **2008**, *99*, 6608.

(8) Pal, N.; Bhaumik, A. *RSC Adv.* **2015**, *5*, 24363.

(9) Liu, R.; Wang, X.; Zhao, X.; Feng, P. *Carbon* **2008**, *46*, 1664.

(10) Lotero, E.; Liu, Y.; Lopez, D. E.; Suwannakarn, K.; Bruce, D. A.; Goodwin, J. G. *Ind. Eng. Chem. Res.* **2005**, *44*, 5353.

(11) Su, F.; Guo, Y. *Green Chem.* **2014**, *16*, 2934.

(12) Saravanan, K.; Tyagi, B.; Bajaj, H. *Catal. Sci. Technol.* **2012**, *2*, 2512.

(13) Chen, X.-R.; Ju, Y.-H.; Mou, C.-Y. *J. Phys. Chem. C* **2007**, *111*, 18731.

(14) Sani, Y. M.; Daud, W. M. A. W.; Aziz, A. A. *Appl. Catal. A Gen.* **2014**, *470*, 140.

(15) Zabeti, M.; Daud, W. M. A. W.; Aroua, M. K. *Fuel Process. Technol.* **2009**, *90*, 770.

(16) Avhad, M.; Marchetti, J. *Catal. Rev.* **2016**, *58*, 157.

(17) Lam, M. K.; Lee, K. T.; Mohamed, A. R. *Biotechnol. Adv.* **2010**, *28*, 500.

(18) Antonelli, D. M. *Adv. Mater.* **1999**, *11*, 487.

(19) McIntosh, D. J.; Kydd, R. A. *Microp. Mesop. Mater.* **2000**, *37*, 281.

(20) Sinhamahapatra, A.; Sutradhar, N.; Ghosh, M.; Bajaj, H. C.; Panda, A. B. *Appl. Catal. A Gen.* **2011**, *402*, 87.

(21) Huang, Y.-Y.; McCarthy, T. J.; Sachtler, W. M. *Appl. Catal. A Gen.* **1996**, *148*, 135.

(22) Yang, X.; Jentoft, F. C.; Jentoft, R. E.; Girgsdies, F.; Ressler, T. *Catal. Lett.* **2002**, *81*, 25.

(23) Risch, M.; Wolf, E. *Appl. Catal. A Gen.* **2001**, *206*, 283.

(24) Stojkovic, N.; Vasic, M.; Marinkovic, M.; Randjelovic, M.; Purenovic, M.; Putanov, P.; Zarubica, A. *Chem. Ind. Chem. Eng. Q.* **2012**, *18*, 209.

(25) Wang, P.; Zhang, J.; Wang, G.; Li, C.; Yang, C. *J. Catal.* **2016**, *338*, 124.

(26) Qi, X.; Guo, H.; Li, L. *Ind. Eng. Chem. Res.* **2011**, *50*, 7985.

(27) Ahmed, A.; El-Hakam, S.; Samra, S.; El-Khouly, A.; Khder, A. *Colloids Surf. A.* **2008**, *317*, 62.

(28) Jin, L.; Zhang, Y.; Dombrowski, J. P.; Chen, C.-H.; Pravatas, A.; Xu, L.; Perkins, C.; Suib, S. L. *Appl. Catal. B Environ.* **2011**, *103*, 200.

(29) Zhang, Y.; Jin, L.; Sterling, K.; Luo, Z.; Jiang, T.; Miao, R.; Guild, C.; Suib, S. L. *Green Chem.* **2015**, *17*, 3600.

(30) de Almeida, R. M.; Noda, L. K.; Gonçalves, N. S.; Meneghetti, S. M.; Meneghetti, M. R. *Appl. Catal. A Gen.* **2008**, *347*, 100.

(31) Shao, G. N.; Sheikh, R.; Hilonga, A.; Lee, J. E.; Park, Y.-H.; Kim, H. T. *Chem. Eng. J.* **2013**, *215*, 600.

(32) Marinković, D. M.; Stanković, M. V.; Veličković, A. V.; Avramović, J. M.; Miladinović, M. R.; Stamenković, O. O.; Veljković, V. B.; Jovanović, D. M. *Renew. Sust. Energ. Rev.* **2016**, *56*, 1387.

(33) Yadav, G. D.; Nair, J. J. *Microp. Mesop. Mater.* **1999**, *33*, 1.

(34) Shi, G.; Yu, F.; Wang, Y.; Pan, D.; Wang, H.; Li, R. *Renew. Energy* **2016**, *92*, 22.

(35) Das, S. K.; Bhunia, M. K.; Sinha, A. K.; Bhaumik, A. *J. Phys. Chem. C* **2009**, *113*, 8918.

(36) Krishnan, C. K.; Hayashi, T.; Ogura, M. *Adv. Mater.* **2008**, *20*, 2131.

(37) Chang, B.; Fu, J.; Tian, Y.; Dong, X. *Appl. Catal. A Gen.* **2012**, *437*, 149.

(38) Wang, Y.; Lee, K.-Y.; Choi, S.; Liu, J.; Wang, L.-Q.; Peden, C. H. *Green Chem.* **2007**, *9*, 540.

(39) Biswas, S.; Poyraz, A. S.; Meng, Y.; Kuo, C.-H.; Guild, C.; Tripp, H.; Suib, S. L. *Appl. Catal. B Environ.* **2015**, *165*, 731.

(40) Poyraz, A. S.; Kuo, C.-H.; Biswas, S.; King'ondu, C. K.; Suib, S. L. *Nat Commun* **2013**, *4*.

(41) Poyraz, A. S.; Kuo, C.-H.; Kim, E.; Meng, Y.; Seraji, M. S.; Suib, S. L. *Chem. Mater.* **2014**, *26*, 2803.

(42) Song, W.; Poyraz, A. S.; Meng, Y.; Ren, Z.; Chen, S.-Y.; Suib, S. L. *Chem. Mater.* **2014**, *26*, 4629.

(43) Lopez, D. E.; Suwannakarn, K.; Bruce, D. A.; Goodwin, J. G. *J. Catal.* **2007**, *247*, 43.

(44) López, D. E.; Goodwin, J. G.; Bruce, D. A. *J. Catal.* **2007**, *245*, 381.

(45) Pizzio, L.; Vázquez, P.; Cáceres, C.; Blanco, M. *Catal. Lett.* **2001**, *77*, 233.

(46) Cid, R.; Pecchi, G. *Appl. Catal.* **1985**, *14*, 15.

(47) Mallesham, B.; Sudarsanam, P.; Raju, G.; Reddy, B. M. *Green Chem.* **2013**, *15*, 478.

(48) Kuo, C.-H.; Poyraz, A. S.; Jin, L.; Meng, Y.; Pahalagedara, L.; Chen, S.-Y.; Kriz, D. A.; Guild, C.; Gudz, A.; Suib, S. L. *Green Chem.* **2014**, *16*, 785.

(49) Morterra, C.; Cerrato, G.; Pinna, F.; Signoretto, M. *J. Catal.* **1995**, *157*, 109.

(50) Sun, Y.; Ma, S.; Du, Y.; Yuan, L.; Wang, S.; Yang, J.; Deng, F.; Xiao, F.-S. *J. Phys. Chem. B* **2005**, *109*, 2567.

CHAPTER 3. SYNTHESIS AND CHARACTERIZATION OF SILICA NANOPARTICLE-BASED ARTIFICIAL ANTIBODY LIKE BINDING SITES USING SURFACE MOLECULAR IMPRINTING

3.1. Overview

Artificial antibody-like binding sites have been prepared on silica nanoparticle (SiNP) using molecular imprinting techniques with a protein as a template molecule. Antibodies are important biological molecules that have a wide range of applications in biomedical analysis, cancer therapy, and drug delivery. However, natural antibodies are expensive, and they have limited stability. In this study, artificial antibody-like nanomaterials of human serum albumin (HSA) and glucose oxidase (GOx) were synthesized by molecular imprinting. Four different organosilane monomers with amino acid-like side chains were used to provide hydrophobic, hydrophilic and H-bonding interactions with the target proteins. The artificial antibodies made by this approach offer a relatively low-cost synthesis along with good selectivity and specificity to binding domains on target proteins. The morphology of the synthesized nanomaterials was characterized by Scanning Electron Microscopy (SEM). Bradford assay and Surface Plasmon Resonance (SPR) were performed to understand the binding affinity of the artificial antibody with respective template protein. The results show that the antibodies were quite selective towards native proteins when compared with other proteins (e.g. bovine serum albumin (BSA), lysozyme, and hemoglobin).

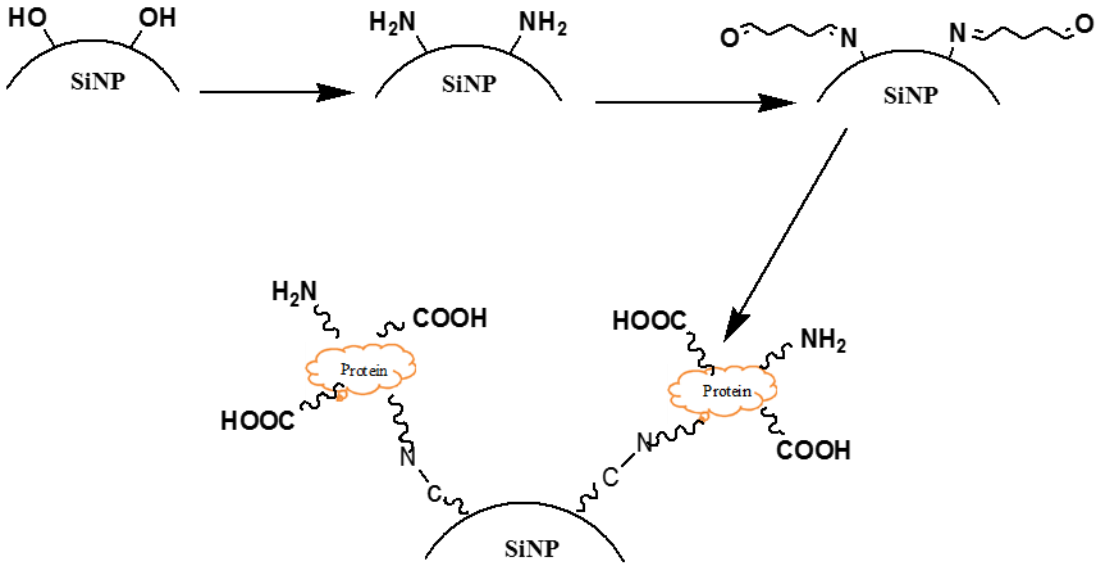

Scheme 3.1. Overview of different steps of grafting the protein molecules on silica nanoparticles.

Abbreviations:

HSA: Human Serum Albumin

GO: Glucose Oxidase

BSA: Bovine Serum Albumin

SiNP: Silica Nanoparticle

AA_{HSA}: Artificial Antibody of HSA

AA_{GO}: Artificial Antibody of GO

MIP: Molecular Imprinted Particles

TEM: Transmission Electron Microscopy

SEM: Scanning Electron Microscopy

DLS: Dynamic Light Scattering

3.2. Background and significance

3.2.1. Molecular imprinting

Molecular imprinting is a generic technology for the creation of three dimensional binding sites in the polymer matrix with the memory of size, shape and functional groups of the template molecules. Although this technique has received significant attention over the past few decades, the concept of molecular imprinting was first proposed back in 1931 by Polyakov.[1] He reported unusual adsorption properties of silica particles prepared by novel synthesis procedure, and subsequently these 'unusual adsorption properties' have been shown by many polymers and named as molecularly imprinted polymers (MIPs).[2] Among various types of molecular imprinting processes, surface imprinting has several advantages over other traditional molecular imprinting techniques. In surface imprinting, the template molecule is attached to the surface of the material, which facilitates the template removal step and results in higher binding capacities.[3] Molecular imprinted particles (MIPs) are synthesized by copolymerization of functional monomers on the surface of the template grafted nanoparticles. The template is subsequently removed from the surface, leaving cavities having similar size, shape and functional groups which would preferentially bind the specific target molecules.

Over the past years, a variety of synthetic strategies have been developed to synthesize molecularly imprinted particles.[4,5] However, there are two major paths to form molecular imprinting, based on the interaction between the particle and the template molecule. One of the paths relies on reversible covalent bonds which were introduced by Wulff,[6] and the other, involving non-covalent interactions, was proposed by Mosbach.[7] In covalent imprinting, the template molecules are bound to the appropriate monomers by covalent bonds. After polymerization, the templates are removed by cleaving the covalent linkage between polymer

and templates. Due to the high stability of the covalent bonds, the template removal step is difficult, and this method is less flexible. However, covalent imprinting yields more homogeneous binding sites on the imprinted particles. In contrast, in the non-covalent process, the template-monomer complexes are formed by different interactions, such as hydrogen bonding, ionic interactions, van der Walls forces, and π - π interactions. Therefore, currently non-covalent imprinting has become a more popular synthetic strategy for molecular imprinting techniques because of the moderate interactions between template and polymer and due to easy template removal.

3.2.2. Artificial antibody

Antibodies are one of the most important protein molecules in our immune system. When antigens (harmful foreign protein molecules) enter in the body, antibodies are produced and specifically bind with those antigens.[8] As antibodies are part of the human immune system and have high affinity and specificity towards antigens, they have been used in various scientific, medical, and research disciplines.[9-11] Applications of antibodies also include their use in immunoassays, modern microfluidic devices, and other bioanalytical techniques.[12-16] Although a wide variety of antibodies is commercially available, isolation and purification make them expensive. Natural antibodies are usually achieved through animal immunization or cellular techniques, which are time consuming and expensive too. The storage stability of antibodies is another important issue for natural antibodies.[17,18] Both time and cost of natural antibodies have made the scientific community think seriously about an alternative to the natural antibodies. For the last few decades, researchers have made enormous progress towards making artificial antibody-like nanomaterials to replace natural antibodies.[19-21] Among different approaches,

molecular imprinting techniques have drawn attention due to their cost-efficiency, stability, and easy synthetic process. Although, this technique is very successful for small molecules, challenges for macromolecular imprinting for biological molecules remain. Structural complexity and stability in harsh environments have made the large biological molecule challenging for molecular imprinting technique.[22] To minimize these issues, researchers are working on imprinting of large biological templates which require optimization of synthetic strategies because of their large size, complexity, solubility, and conformational flexibility.[23]

3.2.3. Molecular imprinting for proteins

Large size, structural diversity and conformational flexibility have made protein molecules challenging to use as templates for making artificial antibodies. Nnvertheless, several reports of the molecular imprinting of protein templates have approached in the literature.[23-26] The primary model for proteins used as template include: hemoglobin, human serum albumin, bovine serum albumin and lysozyme.[25]

Yin and coworkers reported artificial antibodies for lysozyme on track-etched polyethylene tetraphthalate with selectivity better than for similar sized cytochrome c.[27] Zayats et al. imprinted polyacrylamide hydrogels with maltose binding proteins (MBP) on a glass slide.[28] Shioi and coworkers reported covalent immobilization of template protein on microporous silica and used two different organosilanes to enhance affinity.[28] However, the synthesis of high-affinity, high selectivity binding sites for proteins using this approach is only beginning to be explored.[29] Attempts have been made to synthesize artificial antibody binding sites for proteins using silane reagents on solid surfaces.[30-34] Li et al. showed that hydrophilic and hydrophobic interactions are major factors for recognition of template proteins using four silane monomers on

chitosan microspheres.[32] Abbas et al. synthesized stable, reusable imprinted polymers for proteins on gold nanorods using siloxane copolymerization.[18] Cumbo et al. used multiple polymerizable silane monomers to make virus-binding sites on silica nanoparticles.[35]

In this work, artificial antibody-like binding sites for proteins human serum albumin (HSA) and glucose oxidase (GO) were made on 400 nm silica nanoparticles by a molecular imprinting technique. A mixture of organosilanes was used as monomers providing hydrophobic, hydrophilic, and H-bonding interactions. The binding affinity of the artificial antibodies (AAs) were tested with five different proteins, and the results showed specific and selective binding affinity for the native proteins.

3.3. Experimental

3.3.1. Synthesis

3.3.1.1. Chemicals and materials

Tetraethylorthosilicate (TEOS, ≥99%), (3-aminopropyl)-triethoxysilane (APTES, ≥98%), glutaraldehyde (Grade I, 25% in water), albumin from human serum (lyophilized powder), glucose oxidase (type X-S, lyophilized powder), lysozyme (lyophilized powder), bovine serum albumin (lyophilized powder), hemoglobin (lyophilized powder), ammonium hydroxide solution (ACS reagent, 28.0 – 30% NH_3 Base), ethanol (200 proof), hydrochloric acid (ACS reagent 37%), triton X-100, TWEEN 20, sodium phosphate dibasic and sodium phosphate monobasic, Bradford reagents, EDC (3-(N,N-dimethylamino) propyl-N-ethylcarbodiimide) and NHSS (N-Hydroxysulfosuccinimide), glycine were purchased from Sigma – Aldrich (St. Louis, MO, USA). Hydroxymethyltriethoxysilane (HMTEOS), n-propyltriethoxysilane (PTES),

benzyltriethoxysilane (BTES) were obtained from Gelest, Inc. (Morrisville, PA, USA). All chemicals were used without further purification unless otherwise noted. The SPR (surface plasmon resonance) chip functionalized with polyethylene glycol/carboxyl was purchased from Reichert Technologies Life Sciences (Buffalo, NY, USA). All the solutions were filtered through 0.45 µm PVDF-nonsterile filters (Fisher Scientific, PA, USA) before use. All solutions were prepared using 18 MΩ cm water purified by passing house-distilled water through a Hydro Service and Supplies purification system (Durham, NC, USA).

3.3.1.2. Synthesis of silica nanoparticle (SiNP)

All of the chemicals and solvents were equilibrated at room temperature prior to use. The silica nanoparticles were synthesized by following the Stöber process.[36] In a typical synthesis, 40 mL of ammonium hydroxide (28-30%) was mixed with 345 mL of ethanol in a 1L round bottom flask with continuous stirring at 600 rpm at room temperature. After 10 minutes of stirring, 15 mL of tetraethylorthosilicate, ≥99% (TEOS) was added to the mixture and stirring was continued for 20 h at room temperature. The white, milky suspension of silica nanoparticles was centrifuged at 3220 rpm for 10 minutes and reconstituted in ethanol. The suspended particles were washed twice with ethanol and three times with water and centrifuged under the same conditions. Finally, the silica nanoparticles (SiNPs) were suspended in nanopure water, and the colloidal solution was stored at 4 ºC.

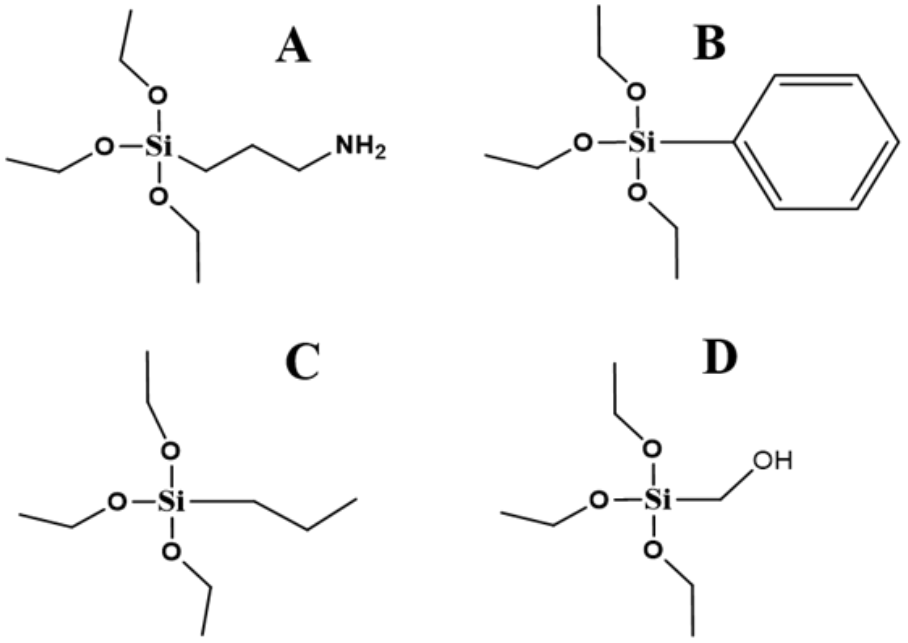

Figure 3.1. Structure of silane monomers used in the imprinting process. **A.** (3-aminopropyl)-triethoxysilane (APTES), **B.** benzyltriethoxysilane (BTES), **C.** n-propyltriethoxysilane (PTES), **D.** Hydroxymethyltriethoxysilane (HMTEOS).

3.3.1.3. Synthesis of protein imprinted particles

The pH of the synthesized silica nanoparticles was adjusted to 7.3 by washing with water and phosphate buffer. To functionalize the silica nanoparticles (SiNPs) with amine groups, 20 mL of 3.0 mg/mL of SiNPs were allowed to react with 22 µL of aminopropyltriethyloxysilane, (APTES) in a round-bottomed flask for 2 h under continuous stirring (400 rpm) at room temperature. The amine-functionalized SiNPs were then washed twice with nanopure water and incubated in 20 mL of 1% (v/v) aqueous glutaraldehyde. After 20 min of incubation, the resultant solution was washed twice with phosphate buffer (10 mM, pH 7.3) and mixed with template protein (50 µg/mL), human serum albumin (HSA) or glucose oxidas (GOx), for 3 h under magnetic stirring. After washing and reconstiting in phosphate buffer, 20 µL of

tetraethylorthosilicate (TEOS) was added, and stirring was continued for 2 h at 10 °C. Then a mixture of four organosilanes [9 µL of benzyltriethoxysilane, (BTES), 9 µL of n-propyltriethoxysilane, (PTES), 18 µL hydroxymethyltriethoxysilane (HMTEOS) and 9 µL of aminopropyltriethoxysilane (APTES)] was added as building blocks for the recognition layer. The organosilane mixture helped to enhance binding affinity by incorporating various binding interactions with the template protein.

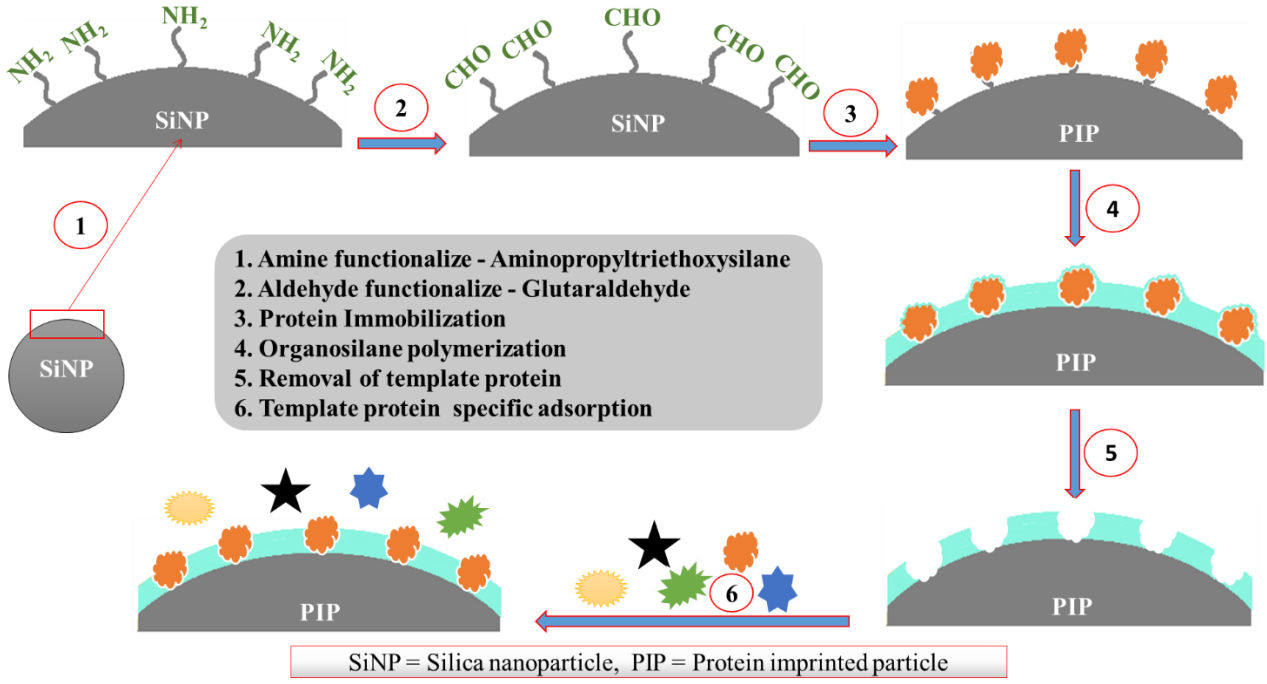

Scheme 3.2. Scheme showing the probable mechanism for the synthesis of artificial antibody. First, the surface was aminated by APTES, followed by addition of glutaraldehyde solution, which helped to bind the protein via imine bond formation between the aldehyde group of glutaraldehyde and a free amine of the protein. Then in step 4, monomers with different amino acid-like functionality were added to generate the binding pockets around the template protein. Then template protein was removed via ultrasonic treatment under acidic medium. Protein rebinding study and selectivity was performed then in presence of other proteins.

3.3.1.4. Removal of the templated protein

After 50 h, the template protein was removed from the product via ultrasonic treatment under acidic condition. The ultrasonic treatment was done for 10 min at 30 °C with 20 mL of 1M HCl containing 0.01% v/v Triton X-100. Resulting products were incubated at 40 °C for 30 min at 600 rpm, and, subsequently, another 30 min of ultrasonic treatment was performed to remove all of the template protein from the system. The probable mechanism for the synthesis of the antibodies is shown in Scheme 3.2. The protein imprinted particles were then washed 4 times and reconstituted in phosphate buffer and stored at 4 °C.

3.3.2. Characterization

3.3.2.1. Scanning electron microscopy

Scanning electron microscopic (SEM) studies were done using Nova NanoSEM 450. A 2.0 kV accelerating voltage and 1.0 mA beam current were used for analysis. The samples were mounted on a gold-plated silica chip. Prior to that, the silica chip was cleaned under plasma treatment to make the surface more hydrophilic so that the sample can be well dispersed onto the chip. After plasma cleaning, 4 µL of a colloidal solution of the sample was put on the chip, and it was kept under vacuum overnight to dry before analysis.

3.3.2.2. Raman

Raman spectra were collected with a Thermo Scientific, NXR FT-Raman Module with a semiconductor laser operating at 976 nm (1.002 W) and equipped with an InGAs detector. 1024

scans were collected with a 4 cm^{-1} spectral resolution in the absorbance mode. In sample preparation, silica nanoparticles were allowed to react with a higher concentration of APTES and glutaraldehyde to obtain a greater number of amine and aldehyde groups attached to the SiNPs. After several washing cycles, the nanoparticles were separated by centrifugation and dried to obtain a powder sample.

3.3.2.3. Zeta potential

Zeta potential measurements were done using ZetaPlus (Brookhaven Instrument Corporation) Zeta potential analyzer. For measuring zeta-potential, 1.5 mL stock solution was taken in a plastic cuvette, and average zeta-potential value was reported based on three measurements.

3.3.2.4. Dynamic light scattering

Dynamic light scattering (DLS) is a physical technique to determine the size of nanoparticles based on Brownian motion. DLS is used to measure the size of colloidal particles, as well as biomolecules, in the solution phase. DLS is also known as Quasi-Elastic light scattering. The measurement depends on the size of the particles, surface properties, solution viscosity, temperature, and particle concentration. If the system is monodispersed, one size distribution is obtained. On the other hand, in a polydispersed system, more than one distribution can be obtained. Dynamic light scattering (DLS) studies were done with an ALV/CGS-3 instrument.

To perform a DLS experiment, the glass tube was cleaned with ethanol and distilled water. All the solvents were filtered using 0.2 µm cut-off filter. Then, 20 µL of 3.2 mg/mL of

sample was taken and 980 µL filtered distilled water was added. DLS was performed at a detector angle of 90° and laser wavelength of 632 nm.

3.3.3. Protein binding studies

The binding nature (selectivity and specificity) of the synthesized artificial antibody with respective template proteins were studied with Bradford assay and surface plasmon resonance techniques. The details of these methods are explained in the following two sections.

3.3.3.1. Bradford assay

The assay is based on the observation that the absorbance maximum for an acidic solution of Coomassie Brilliant Blue G-250 shift from 465 nm to 595 nm when they bind with proteins. Both hydrophobic and ionic interactions stabilize the anionic form of the dye.

A 1:1 ratio of freshly prepared protein solution in 10 mM phosphate buffer (pH 7.3) was mixed with the corresponding artificial antibodies (AAs) and incubated for 2 h in a slow rotation mode. Then the solution was centrifuged at 3200 rpm for 3 min, and the supernatant solution was analyzed by a Bradford assay to determine the amount of protein bound to the antibodies. The selectivity of the AAs was tested using both homogeneous and non-homogeneous proteins. Human serum albumin (HSA), bovine serum albumin (BSA), glucose oxidase (GOx), lysozyme and hemoglobin were tested with AAs under the same conditions. The protein in the solution reacts with the Bradford reagent to form a blue colored compound, and the absorbance at 595 nm was measured to quantify the amount of proteins. The amount of proteins bound was measured using the subtraction method.

3.3.3.2. Surface plasmon resonance

Surface plasmon resonance (SPR) is a technique to measure biomolecular interactions in real time over the surface of a heavy metal like gold or silver. SPR measures the binding events while one reactant is immobilized on the sensor surface, and the other one is allowed to flow over the immobilized reactant in a label-free environment.

The surface plasmon resonance (SPR) experiments were performed using a Reichert SPR700DC dual channel flow SPR spectrometer with gold chips prefunctionalized with a mixed monolayer (10% COOH-$(PEG)_6$-alkanethiol and 90% OH-$(PEG)_3$-alkanethiol) at 20 °C.

3.4. Results

3.4.1. Morphology of silica nanoparticles

The scanning electron microscopic (SEM) images of silica nanoparticles showed a smooth surface for the particles. The average size of the nanoparticles was around 400 nm. The particles were well dispersed in their colloidal solution.

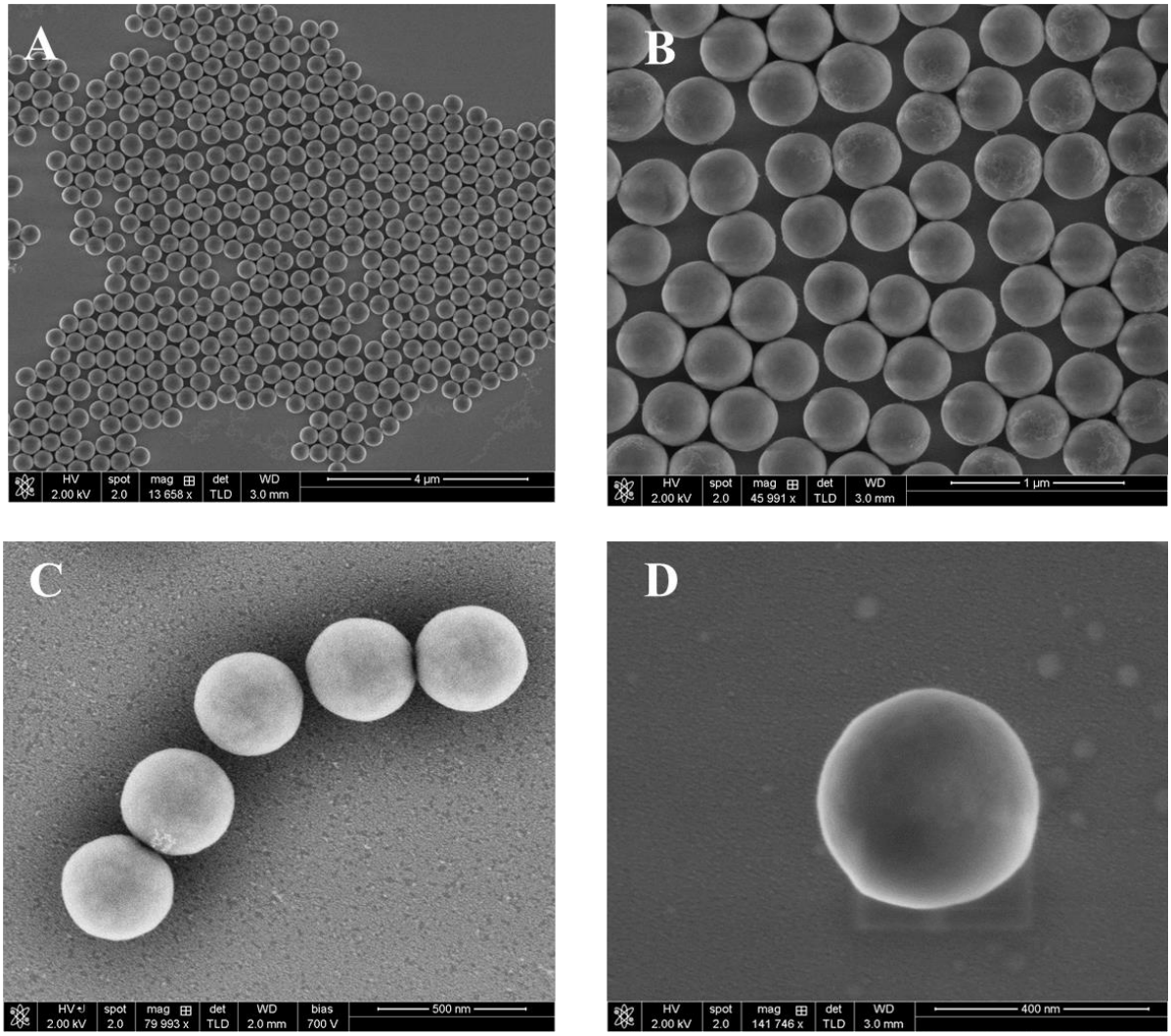

Figure 3.2. Morphology of silica nanoparticles (SiNPs) at different magnifications. SEM image of SiNPs at (A) 4 µm, (B) 1 µm, (C) 500 nm, and (D) 400 nm.

3.4.2. Morphology of the artificial antibody

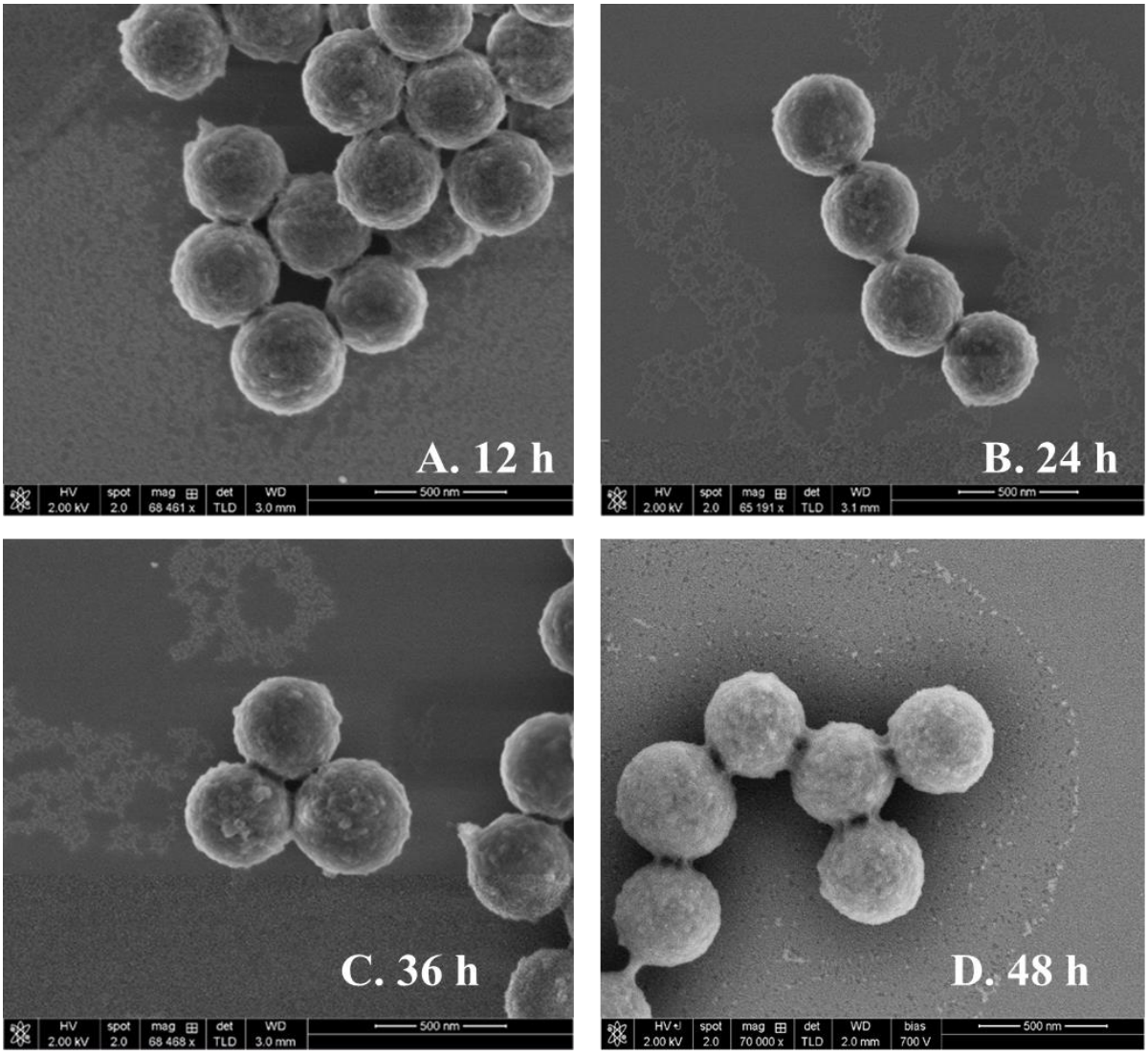

Figure 3.3. Morphology of the nanoparticles at different points during reaction. The growth of polymer coating on SiNP with organosilane mixture at different reaction time, (A) 12 h, (B) 24 h, (C) 36 h, and (D) 48 h.

The surface of the nanoparticles changes with time. The surface of the silica nanoparticles was very smooth initially (Figure 3.2) whereas the surface of the nanoparticles became rough during the propagation of reaction (Figure 3.3). After removal of the template

proteins, the surface roughness increased greatly because of the creation of binding sites on the surface. Figure 3.4 shows the roughness of the surface of the artificial antibody.

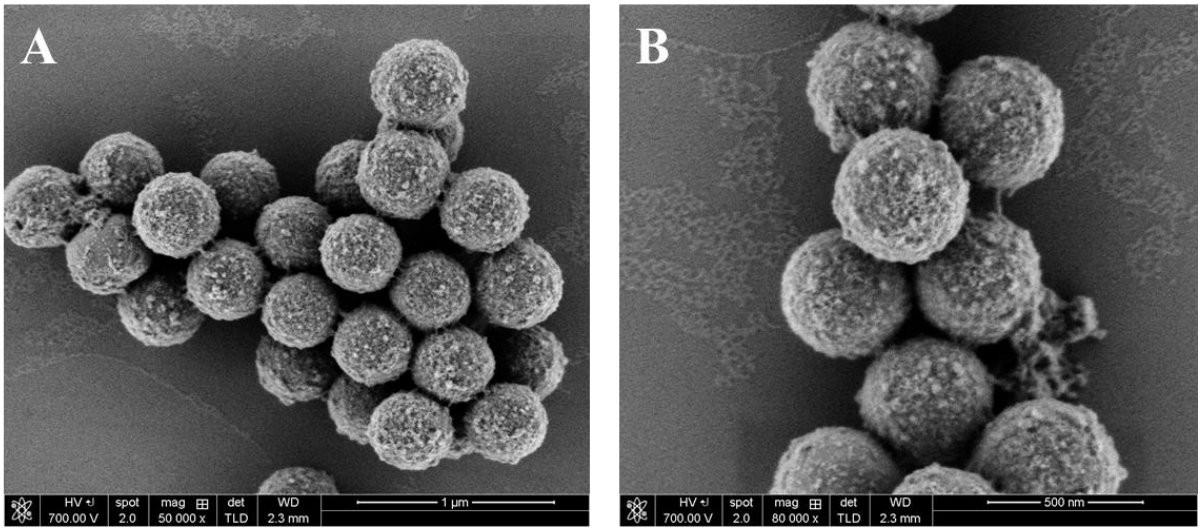

Figure 3.4. SEM images of artificial antibodies at **(A)** 1 µm, **(B)** 500 nm magnification after removal of template protein.

3.4.3. Raman analysis

Raman spectroscopy confirmed the covalent binding of APTES to SiNP in the initial stages of binding site construction. In APTES-SiNP, the NH_2 peaks (for out of plane bending at 895 cm^{-1} and rocking/twisting or bending ~ 1100 cm^{-1})[37] overlap with Si-O peaks in the same region. However, new bands for APTES-SiNPs at 1458 cm^{-1} and 2936 cm^{-1} can be assigned to C-H bending (1458 cm^{-1}) and C-H stretching (2936 cm^{-1})[37,38] from multiple C-H bonds in APTES (Figure 3.5).

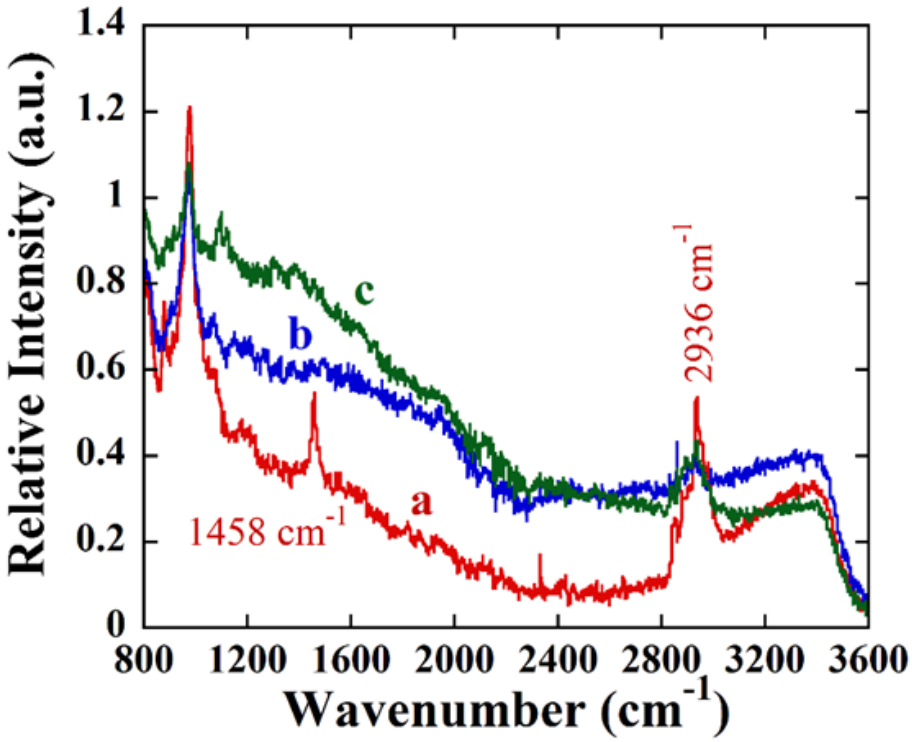

Figure 3.5. Raman spectra of (a) silica-APTES, (b) silica nanoparticle (SiNP) and (c) silica-imine.

After addition of the glutaraldehyde the C=O bond involved in hydrogen bonding and C-H bending of aldehyde group interact with other vibrations and might appear in a wide spectral range of around 1430 – 1200 cm^{-1}.[39] There was hardly any peak after protein binding (data not shown) as the protein has an intrinsic fluorescence nature which embedded all the characteristic peaks.[40]

3.4.4. Surface charge and hydrodynamic radius

Surface charge was measured by zeta-potential measurements. The potential of bare SiNP was about -60 mV, but decreased to ~ -20 mV for the AAs and any particles that have adsorbed protein. The results of zeta potential and hydrodynamic radii are summarized in Table 3.1.

Table 3.1. Zeta-potentials and avg. hydrodynamic radii from dynamic light scattering (DLS) of silica nanoparticles, artificial antibodies and bioconjugates with these particles in 10 mM phosphate buffer pH 7.3.

Particles	Zeta-Potential (mV)	Hydrodynamic radius (nm)
SiNP[a]	-59.3	205
SiNP-HSA[b]	-19.1	245
SiNP-GOx[c]	-22.3	251
AA_{HSA}[d]	-20.4	430
AA_{GO}[e]	-21.4	421
AA_{HSA}-HSA[f]	-17.6	490
AA_{GOx}-GOx[g]	-18.2	454

[*]Solvent: 10 mM phosphate buffer, pH 7.3.

[a]Silica nanopartilces (SiNPs) of 3.0 mg/mL; [b]SiNPs (3.0 mg/mL) and human serum albumin (HSA) conjugates; [c]SiNPs (3.0 mg/mL) and glucose oxidase (GOx) conjugates; [d]Artificial antibodies of HSA (AAHSA); [e]Artificial antibodies of GOx (AAGOx); [f]AAHSA and HSA conjugates in PB; [g]AAGOx and GOx conjugates.

Hydrodynamic radii of the synthesized SiNPs were about 205 nm, which was the smallest of all other studied particles. The radii increased by 40-45 nm when the protein adsorbed to the bare silica nanoparticles. The radii of the synthesized AAs was about 200 nm larger than the SiNPs, and, finally, when the target protein attached to the AAs, a large increase in radii was obtained.

3.4.5. Protein binding studies by Bradford assay

The selectivity of the AAs was tested for binding to human serum albumin (HSA), glucose oxidase (GOx), bovine serum albumin (BSA), lysozyme and hemoglobin (Hb). Bradford assay was done to determine the amount of protein that bind to the antibodies by measuring the absorption at 595 nm. Figure 4.6 (A) shows the adsorption isotherms of an artificial antibody of HSA (AA_{HSA}) bound with different proteins, and figure 4.6 (B) shows the results of an artificial antibody of glucose oxidase (AA_{GO}) with different proteins.

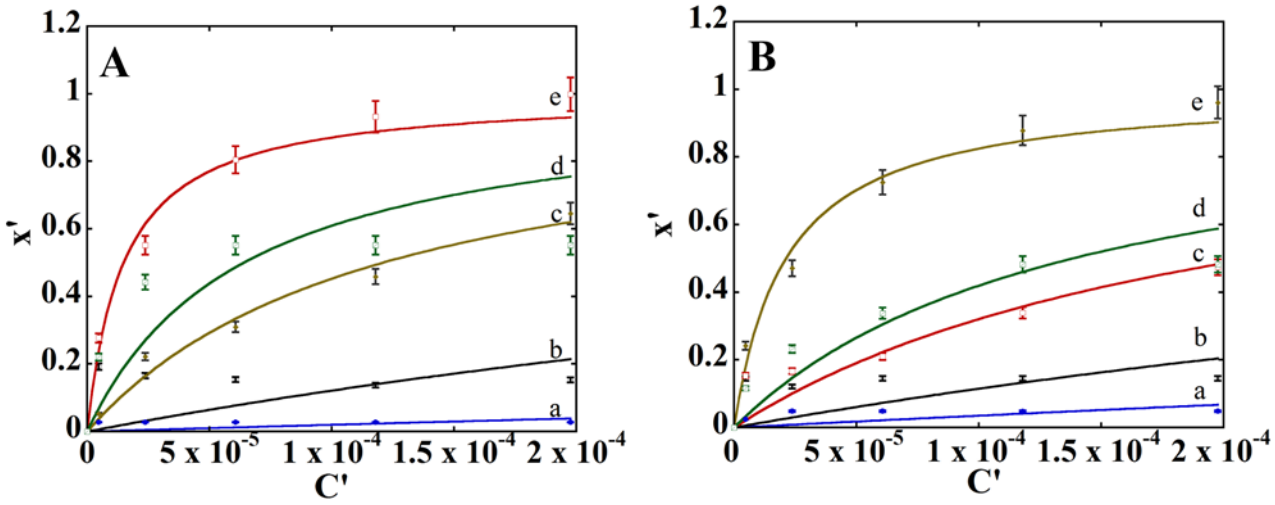

Figure 3.6. Binding isotherm for different proteins with artificial antibodies of human serum albumin (AA_{HSA}) and artificial antibodies of glucose oxidase (AA_{GOx}) to monitor selectivity using a Bradford assay. **(A):** Plot showing binding of AAHSA with **a:** lysozyme; **b:** bovine serum albumin (BSA); **c:** glucose oxidase (GOx); **d:** hemoglobin; **e:** human serum albumin (HSA). **(B):** Plot showing binding of AA_{GOx} with **a:** lysozyme; **b:** BSA; **c:** HSA; **d:** hemoglobin; **e:** GOx.

The results indicate that the template proteins HSA and GOx bind more with their corresponding artificial antibodies compared to other proteins. Both the antibodies of human

serum albumin (AA_{HSA}) and glucose oxidase (AA_{GOx}) showed very weak affinity toward BSA and lysozyme. The molecular weight of these proteins are given in Table 4.2.

Table 3.2. Molecular weight of the proteins used in the Bradford assay.

Protein	Molecular weight (kDa)
Human serum albumin (HSA)	66.5
Bovine serum albumin (BSA)	66.5
Glucose oxidase (GO)	160
Lysozome	14.3
Hemoglobin	64.5

3.4.6. Binding studies by SPR

The SPR responses increased with increasing concentration of AA_{HSA} (Figure 4.7) for both HSA and GOx immobilized on gold surfaces of SPR chips. But the association responses were higher for all the antibody concentrations which signify it's stronger affinity towards the immobilized proteins. After the feed solution was changed to buffer, the signal became flat suggesting little dissociation after 30 min. Maximum binding SPR signals for the antibodies were for their respective template proteins than other proteins. Figures 4.7 and 4.8 show the SPR responses for protein-AA_{HSA} and protein-AA_{GOx} binding.

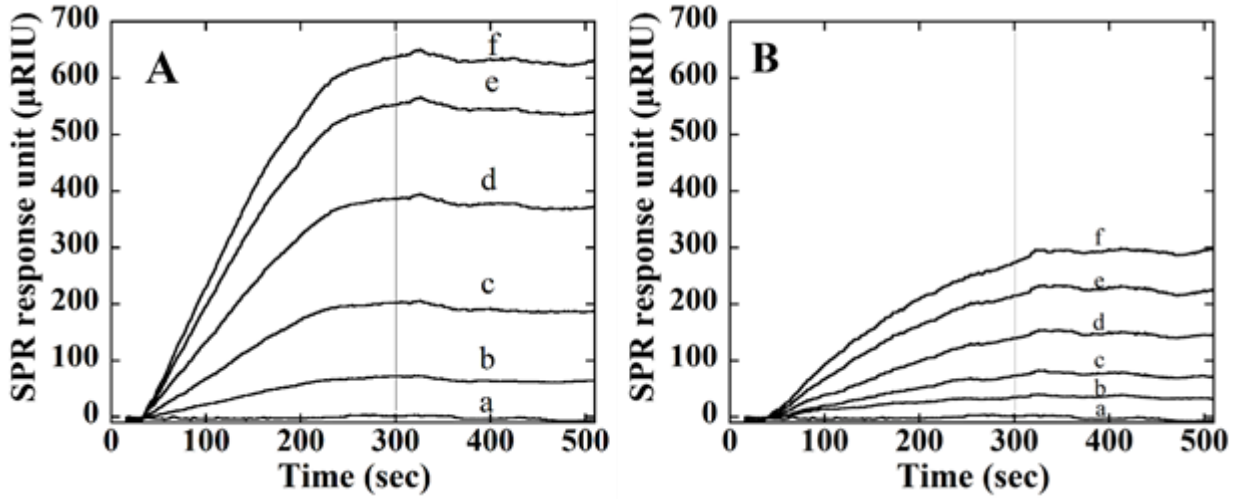

Figure 3.7. SPR responses flow rate 100 µL/min for association (0-300 sec) and dissociation (300-600 sec) of AA_{HSA}. Different [AA_{HSA}] were injected: (a). 0 µg/mL, (b). 0.15 µg/mL, (c). 0.30 µg/mL, (d). 0.60 µg/mL, (e). 1.2 µg/mL and (f). 1.8 µg/mL. Chip surface was immobilized with (A) HAS and (B) GOx.

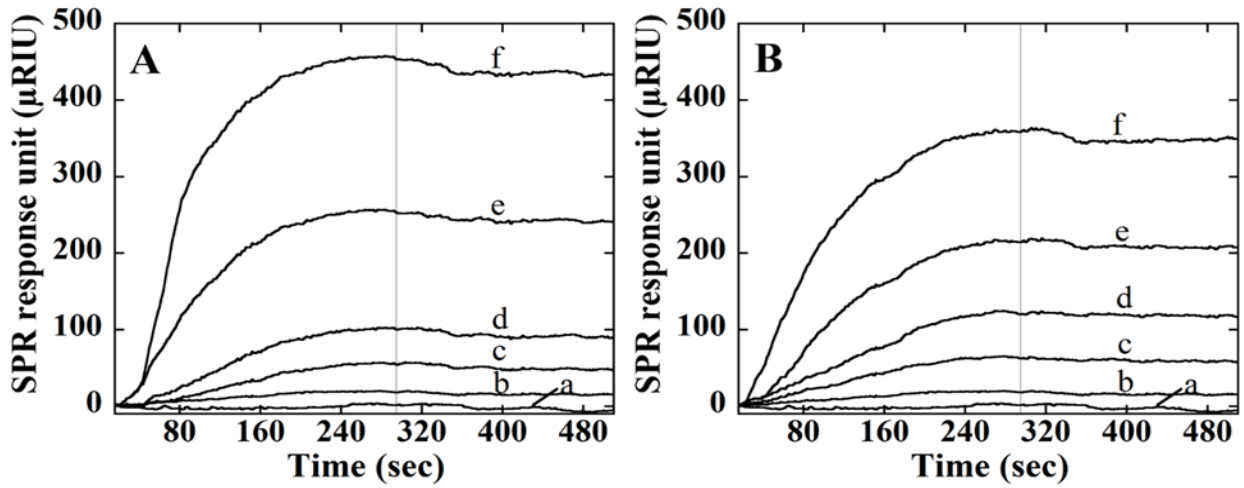

Figure 3.8. SPR responses flow rate 100 µL/min for association (0-300 sec) and dissociation (300-600 sec) of AA_{GOx}. Different concentration of AA_{GOx} was injected: (a). 0 µg/mL, (b). 0.15 µg/mL, (c). 0.30 µg/mL, (d). 0.60 µg/mL, (e). 1.2 µg/mL and (f). 1.8 µg/mL. Chip surface was immobilized with (A) GOx and (B) HSA.

3.5. Discussion

In this study, the synthesis of the artificial antibody of human serum albumin (AA_{HSA}) and glucose oxidase (AA_{GOx}) on the surface of silica nanoparticles (SiNPs) using a molecular imprinting technique was demonstrated. Spherical, 400 nm SiNPs were synthesized and amine groups were incorporated to immobilize template proteins using aminopropyltriethoxysilane (APTES) and glutaraldehyde. Molecular imprinting of proteins is always challenging because of its three dimensional structural orientation and presence of different types binding interactions. To overcome the issue, various silane monomers with different amino-acid-like functional groups were used during the polymerization step.

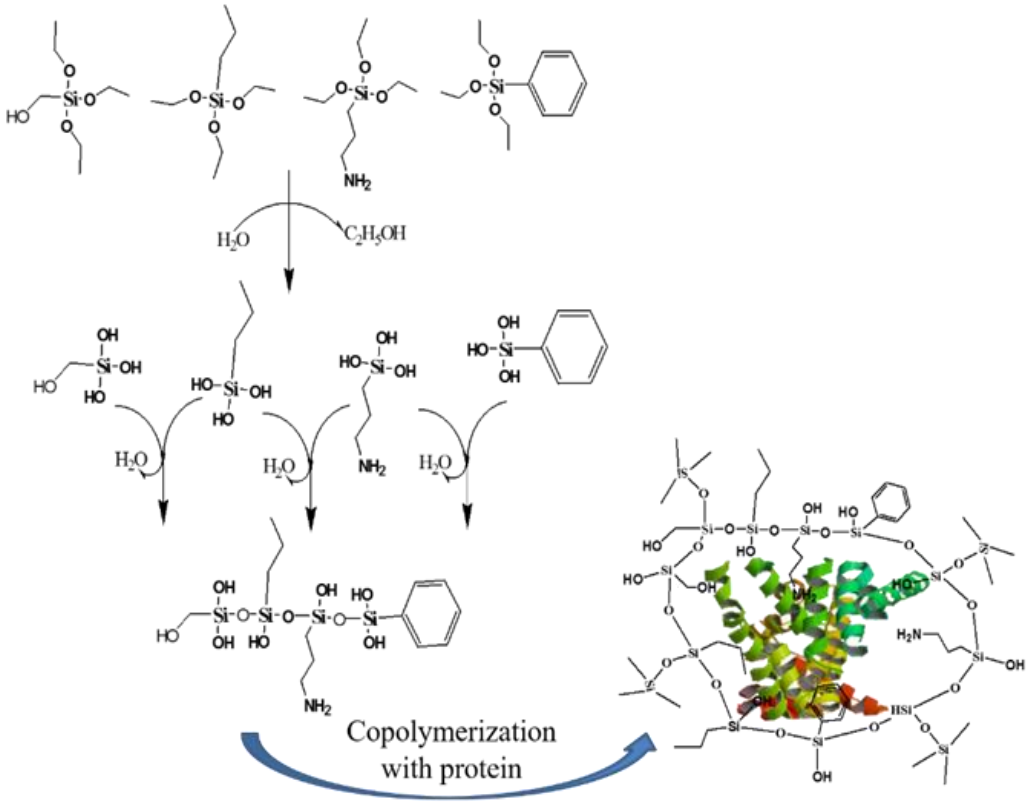

Scheme 3.3. A possible mechanism of the copolymerization of all the organo-silane monomers in the presence of template protein in pH 7.3 buffer at 10 ˚C. The monomers undergo hydrolysis, followed by condensation, to form the siloxane cage surround the template protein by incorporation of amino acid-like functional groups on the surface to maximum the binding efficiency.

Mixtures of benzyltriethoxysilane (BTES), n-propyltriethoxysilane (PTES), hydroxymethyltriethoxysilane (HMTEOS), and aminopropyltriethoxysilane (APTES) were used to tailor the AA-protein interaction. The tentative formation of the polymeric coating on the surface is explained in Scheme 3.3. The growth of polymer was monitored using SEM, DLS and Zeta-potential measurements. The surface morphology was very rough, as shown by microscopy images (Figure 3.3 & 3.4), and the diameter was also found to increase after the imprinting process. The DLS diameter for AA_{HSA} was 490 nm, which is greater than bare SiNPs and signifies the growth of particle size due to polymerization. The increased diameter after binding with proteins might be due to particle aggregation or protein-protein interaction. The intermediate chemistry after the addition of APTES on SiNPs was analyzed using Raman spectroscopy to understand covalent binding with the amine and formation of an imine. Two bands at 1458 cm^{-1} and 2936 cm^{-1} were found for the amination reaction due to the binding of APTES on SiNPs. The binding of the synthesized antibody with the native proteins was quantified by Bradford assays. The selectivity of the artificial antibody was obtained by analyzing with different proteins using the Bradford assay. Both antibodies for HSA and GOx did not bind with small proteins like lysozyme. The incorporation of four monomers helped to enhance binding affinity via different interactions, such as hydrophobic, hydrophilic, and H-bonding, resulting in strong AA-protein binding. Surface plasmon resonance (SPR) experiments also indicated very strong binding of protein HSA with AA_{HSA}, and there was hardly any dissociation. In this case, the surface was first activated with EDC/NHSS chemistry, followed by immobilization of the proteins on the activated Au surfaces. Different concentrations of artificial antibodies in 10 mM phosphate buffer (pH 7.3) were then injected at a flow rate of 100 µL/min for 300 sec, and dissociation events were monitored during the injection period. The selectivity

was higher as the apparent association constant was higher than other protein interaction with AA_{HSA}. In addition, artificial antibodies of glucose oxidase (AA_{GOx}) also showed similar behavior towards its template protein, and that signifies the high selectivity and specificity of the antibodies. Overall, the artificial antibody was very selective, and specificity was very promising.

3.6. Conclusion

Replacement of the natural antibodies in many analytical studies with artificial AAs would be feasible if AAs showed similar binding affinity and selectivity. In this report, we show the synthesis of the AAs of HSA and GO using surface molecular imprinting technique with promising specificity and selectivity. We studied the morphology and binding properties of these artificial antibodies. Four different silane monomers having different amino-acid-like groups were selected to achieve maximum binding by tailoring binding properties, such as H-bonding, ionic interactions, hydrophilic/hydrophobic interactions, etc. The roughness on the surface of the nanoparticles under electron microscopy proved the completion of imprinting process. The incorporation of a mixture of monomers enhanced the affinity of AAs towards the template proteins with promising specificity. The association constant of the AA and its template protein was calculated as 1.26 $(mg/mL)^{-1}sec^{-1}$ by studying the binding events using SPR, which was also higher than other proteins. Similar results were obtained for AAs of GO, which signifies that the antibodies are very specific and selective. This approach could lead to the preparation of many types of AAs for cancer biomarkers and corresponding research.

Reference list

(1) Polyakov, M. *Zh. Fiz. Khim.* **1931**, *2*, 799.

(2) Alexander, C.; Andersson, H. S.; Andersson, L. I.; Ansell, R. J.; Kirsch, N.; Nicholls, I. A.; O'Mahony, J.; Whitcombe, M. J. *J. Mol. Recogn.* **2006**, *19*, 106.

(3) Gao, D.; Zhang, Z.; Wu, M.; Xie, C.; Guan, G.; Wang, D. *J. Am. Chem. Soc.* **2007**, *129*, 7859.

(4) Chen, L.; Xu, S.; Li, J. *Chem. Soc. Rev.* **2011**, *40*, 2922.

(5) Chen, L.; Wang, X.; Lu, W.; Wu, X.; Li, J. *Chem. Soc. Rev.* **2016**, *45*, 2137.

(6) Wulff, G. *Angew. Chem. Int. Ed.* **1995**, *34*, 1812.

(7) Mosbach, K. *Trends Biochem. Sci.* **1994**, *19*, 9.

(8) Voet, D.; Voet, J. *Biochemistry, 3rd Edn. Wiley, New York* **2004**, 356.

(9) Lipman, N. S.; Jackson, L. R.; Trudel, L. J.; Weis-Garcia, F. *ILAR J.* **2005**, *46*, 258.

(10) Adams, G. P.; Weiner, L. M. *Nat. Biotechnol.* **2005**, *23*, 1147.

(11) Payne, W.; Marshall, D.; Shockley, R.; Martin, W. *Clin. Microbiol. Rev.* **1988**, *1*, 313.

(12) Chiarella, P.; Fazio, V. M. *Biotechnol. Lett.* **2008**, *30*, 1303.

(13) Flanagan, J.; Arjomandi, A.; Delanoy, M.; Du Paty, E.; Galea, P.; Laune, D.; Rieunier, F.; Walker, R.; Binder, S. *J. Immunol. Methods* **2014**, *406*, 34.

(14) Zhang, S.; Garcia-D'Angeli, A.; Brennan, J. P.; Huo, Q. *Analyst* **2014**, *139*, 439.

(15) Grange, R.; Thompson, J.; Lambert, D. *Br. J. Anaesth.* **2014**, *112*, 213.

(16) Malhotra, R.; Patel, V.; Chikkaveeraiah, B. V.; Munge, B. S.; Cheong, S. C.;

Zain, R. B.; Abraham, M. T.; Dey, D. K.; Gutkind, J. S.; Rusling, J. F. *Anal. Chem.* **2012**, *84*, 6249.

(17) Zhang, Z.; Guan, Y.; Li, M.; Zhao, A.; Ren, J.; Qu, X. *Chem. Sci.* **2015**, *6*, 2822.

(18) Abbas, A.; Tian, L.; Morrissey, J. J.; Kharasch, E. D.; Singamaneni, S. *Adv. Funct. Mater.* **2013**, *23*, 1789.

(19) Ansell, R. J.; Ramström, O.; Mosbach, K. *Clin. Chem.* **1996**, *42*, 1506.

(20) Li, Y.; Li, X.; Li, Y.; Dong, C.; Jin, P.; Qi, J. *Biomaterials* **2009**, *30*, 3205.

(21) Luan, J.; Liu, K.-K.; Tadepalli, S.; Jiang, Q.; Morrissey, J. J.; Kharasch, E. D.; Singamaneni, S. *ACS Appl. Mater. Interfaces* **2016**, *8*, 23509.

(22) Vasapollo, G.; Sole, R. D.; Mergola, L.; Lazzoi, M. R.; Scardino, A.; Scorrano, S.; Mele, G. *Int. J. Mol. Sci.* **2011**, *12*, 5908.

(23) Turner, N. W.; Jeans, C. W.; Brain, K. R.; Allender, C. J.; Hlady, V.; Britt, D. W. *Biotechnol. Progr.* **2006**, *22*, 1474.

(24) Verheyen, E.; Schillemans, J. P.; van Wijk, M.; Demeniex, M.-A.; Hennink, W. E.; van Nostrum, C. F. *Biomaterials* **2011**, *32*, 3008.

(25) Takeuchi, T.; Hishiya, T. *Org. Biomol. Chem.* **2008**, *6*, 2459.

(26) Janiak, D. S.; Kofinas, P. *Anal. Bioanal. Chem.* **2007**, *389*, 399.

(27) Yin, D.; Ulbricht, M. *J. Mater. Chem. B* **2013**, *1*, 3209.

(28) Zayats, M.; Kanwar, M.; Ostermeier, M.; Searson, P. C. *Macromolecules* **2011**, *44*, 3966.

(29) Hansen, D. E. *Biomaterials* **2007**, *28*, 4178.

(30) Gao, R.; Mu, X.; Hao, Y.; Zhang, L.; Zhang, J.; Tang, Y. *J. Mater. Chem. B* **2014**, *2*, 1733.

(31) Kan, X.; Zhao, Q.; Shao, D.; Geng, Z.; Wang, Z.; Zhu, J.-J. *J. Phys. Chem. B* **2010**, *114*, 3999.

(32) Li, F.; Li, J.; Zhang, S. *Talanta* **2008**, *74*, 1247.

(33) Pradhan, S.; Boopathi, M.; Kumar, O.; Baghel, A.; Pandey, P.; Mahato, T.; Singh, B.; Vijayaraghavan, R. *Biosens. Bioelectron.* **2009**, *25*, 592.

(34) Yang, Y.-Q.; He, X.-W.; Wang, Y.-Z.; Li, W.-Y.; Zhang, Y.-K. *Biosens. Bioelectron.* **2014**, *54*, 266.

(35) Cumbo, A.; Lorber, B.; Corvini, P. F.-X.; Meier, W.; Shahgaldian, P. *Nat. Commun.* **2013**, *4*, 1503.

(36) Stöber, W.; Fink, A.; Bohn, E. *J. Colloid Interface Sci.* **1968**, *26*, 62.

(37) Stewart, J. E. *J. Chem. Phys.* **1959**, *30*, 1259.

(38) Nomura, A.; Jones, C. W. *ACS Appl. Mater. Interfaces* **2013**, *5*, 5569.

(39) Jastrzebska, M.; Wrzalik, R.; Kocot, A.; Zalewska-Rejdak, J.; Cwalina, B. *J. Biomat. Sci. Polym. Ed.* **2003**, *14*, 185.

(40) Hanlon, E.; Manoharan, R.; Koo, T. W.; Shafer, K.; Motz, J.; Fitzmaurice, M.; Kramer, J.; Itzkan, I.; Dasari, R.; Feld, M. *Phys. Med. Biol.* **2000**, *45*, R1.

CHAPTER-4: COBALT OXIDE-COBALT SULFIDE/CARBON HYBRIDS AS EFFICIENT BIFUNCTIONAL ELECTROCATALYST FOR OXYGEN AND HYDROGEN EVOLUTION REACTION

4.1 Overview

Electrocalytic water splitting produces hydrogen, a clean and sustainable source of energy. Hydrogen is considered as a very good alternative to fossil fuel. However, transition metal based low cost, and stable material design and synthesis are still challenging. Herein, cobalt oxide-cobalt sulfide/carbon hybrid material is synthesized for hydrogen evolution and oxygen evolution reaction. The material is characterized by XRD, SEM, TEM, Raman, and XPS. The electrochemical studies are performed by linear sweep voltammetry (LSV) measurements. The result shows that the hybrid material has an excellent activity for HER in acidic medium with an overpotential of 360 mV (vs SCE) at a current density of 10 mA/cm^{-2}.

Abbreviations:

HER: Hydrogen Evolution Reaction

OER: Oxygen Evolution Reaction

LSV: Linear Sweep Voltammetry

SCE: Standard Calomel Electrode

GO: Graphene Oxide

CNT: Carbon Nanotube

MWCNT: Multi-Walled Carbon Nanotube

O-CNT: Oxidized Carbon Nanotube

CoNP: Cobalt oxide Nanoparticle

CoNP-GO: Cobalt oxide Nanoparticle on Graphene Oxide

CoNP-GO-S: Sulfided Cobalt oxide Nanoparticle on Graphene Oxide

CoNP-O-CNT: Cobalt oxide Nanoparticle on Oxidized Carbon Nanotube

CoNP-O-CNT-S: Sulfided Cobalt oxide Nanoparticle on Oxidized Carbon Nanotube

4.2 Background and significance

With increasing energy consumption and energy shortages, intense research has been carried out to find new energy resources and storage techniques. Electrochemical water splitting into hydrogen and oxygen, where electric energy is stored in the form of chemical energy, is an important source of energy since the method is cost-effective, sustainable, and environmentally friendly. The water-splitting reaction can be divided into two half reactions: the oxygen evolution reaction (OER) and the hydrogen evolution reaction (HER). These reactions are thermodynamically unfavorable and require high energy input. Hence, nanoscale catalysts are of great advantage for these reactions since they have a large surface area to volume ratio.[1] However, Pt, Ir, and Ru based materials being the state-of-the-art catalysts, the widespread and commercial applicability of water-splitting have been limited due to their high cost, shortage of reserves and toxicity.[2-4] Therefore, it remains challenging to develop robust, efficient,

inexpensive, non-precious metal catalysts that can rival the performance of Pt, Ru, and Ir. As a result, naturally abundant, less toxic transition metals such as Mn, Co, Cu, Fe, and Ni based materials are widely being used as HER and OER catalysts.[2-5]

The oxygen evolution reaction (OER) takes placed at the anode, where water gets oxidized to molecular oxygen. Moreover, since OER requires four electron transfer steps compared to two for HER, it is responsible for more efficiency loss.[5] Thermodynamic density functional theory (DFT)- based OER studies, a volcano type activity plot was created predicting the binding energy of a surface oxygen species as the activity-controlling parameter.[1] Ru and Ir oxide, lying near the top of the volcano plot, are known as the most promising OER catalysts; hence they are frequently studied. Use of less toxic, cost effective, and readily available non-noble metal based catalysts for the OER in acidic media is hindered mainly due to the acid aggressive and strong corrosive conditions.[1] However, significant progress has been achieved on OER with catalysts made of cheap, earth abundant elements, including $Co^{3+/4+}$, $Ni^{3+/4+}$, $Mn^{3+/4+}$, and $Fe^{3+/4+}$.[6]

Cobalt based materials, especially Co_3O_4 spinel, are intensively studied in OER catalysis owing to their superior activity, earth abundance, long-term stability, low cost, and low toxicity.[2,7,8] In their study Maiyalagan et al. suggest that the presence of Co^{3+} in the Co_4O_4 cubane-like structure enhances its OER activity by facilitating the formation of O-O bonds.[8] According to the work done by Frei and co-workers, there are two active sites for Co_3O_4 nanoparticles in water oxidation: the oxo-bridged Co(III)OH binuclear sites and single Co(III)OH sites.[9]

Cobalt oxide nanoparticles (CoNP) have been studied as cathode materials of the electrochemical cell where the hydrogen evolution reaction (HER) takes place and found to be

very promising.[2,3,10-12] Wang and co-workers reported 3D graphene/cobalt sulfide hybrid materials for HER and supercapacitors.[13] This material is lightweight and flexible, and has a low overpotential of -0.11 V and a Tafel slope of 93 mV dec^{-1} for HER. Miao et al. synthesized reduced graphene oxide supported nickel-manganese-cobalt ternary oxide nanocomposites for water splitting. Their nanocomposites were found to be an efficient HER and OER catalyst. Cobalt sulfide film-like material was prepared by Yujie Sun and co-workers for electrochemical and photochemical hydrogen generation from neutral pH water.[14] For HER catalysis, molybdenum oxide and sulfide materials are also very promising candidates and show very good activities, depending on the structure, morphology, and synthetic techniques.[13,15-18] Recently, carbon nanotube and graphene oxide-based hybrid materials have drawn significant attention for electrocatalytic applications due to their high surface area and high conductivity.[19-22]

Cobalt oxide nanoparticle materials have been synthesized by facile microwave irradiation. After preliminary studies and on the literature, a hybrid material has been designed for HER and OER reactions. The synthesized cobalt oxide-cobalt sulfide/carbon hybrid material shows very close electrocatalytic performance compared to the state-of-the-art Pt catalysts.

4.3. Experimental

4.3.1. Catalyst synthesis

Initially, cobalt oxide nanoparticle (CoNP) was synthesized and then sulfided (CoNP-S) for HER and OER electrocatalytic reactions. After a preliminary survey, graphene oxide (GO) and carbon nanotube based cobalt oxide-cobalt sulfide/carbon hybrid materials were designed and synthesized. The hybrid materials are: cobalt oxide nanoparticles on oxidized carbon

nanotube (CoNP-O-CNT), sulfided cobalt oxide on oxidized carbon nanotube (CoNP-O-CNT-S), cobalt oxide nanoparticles on graphene oxide (CoNP-GO), and sulfided cobalt oxide on graphene oxide (CoNP-GO-S). Sulfided materials were synthesized by *in situ* sulfidations of the corresponding oxide materials. Different synthetic steps are explained in following sections.

4.3.1.1. Synthesis of cobalt oxide nanoparticle (CoNP)

Cobalt oxide (Co_3O_4) nanoparticles were synthesized via a microwave assisted heating process. Dong and coworkers reported a facile, surfactant-free, controlled synthesis of Co_3O_4 nanoparticles in a hydrothermal method.[23] In a typical synthesis, 500 mg of Cobalt (II) acetate tetrahydrate ($Co(CH_3COO)_2.4H_2O$) was dissolved in 25 mL of water/ethanol mixed solvent (10 mL of water and 15 mL of ethanol). 2.5 mL of 25% ammonia was added to the solution under vigorous stirring. The mixture was stirred in air for another 10 min resulting in a black solution. Then 12 mL of this solution was taken in a 20 mL microwave vial, and sealed with a PTFE lined cap. The reaction was performed in a Biotage^{TM} Initiator 2.5 microwave reactor at 150 °C for 35 min. After that, the product was centrifuged and washed with H_2O via centrifugation-redispersion. Finally, the material was dried under vacuum at 60 °C for overnight and labelled as CoNP.

4.3.1.2. Oxidation of carbon nanotube

Multiwall pristine carbon nanotubes (MWCNT) were oxidized with concentrated nitric acid (HNO_3). In a typical oxidation process, 600 mg of pristine CNT were added to 200 mL of conc. HNO_3 in a 250 mL round-bottom flask. Then the mixture of CNT and HNO_3 was sonicated for 2 h in an ultrasonic bath. After sonication, the flask was equipped with a reflux condenser,

magnetic stirrer, and a thermometer in a preheated oil bath. The reaction mixture was refluxed for 24 h at 110 °C. After that, the mixture was cooled to room temperature and centrifuged. The product was washed with acetone three-four times to bring the pH to around 5. After several washing cycles, the material was kept in a vacuum dryer overnight. Finally, the material was ground and labeled as oxidized carbon nanotube (O-CNT).

4.3.1.3. Oxidation of graphene oxide

Graphene oxide (GO) was synthesized from natural graphite using a modified Hummer's method. 1.0 g of graphite powder and 2.0 g of $NaNO_3$ were mixed and added to 48 mL of concentrated H_2SO_4 (98%) in an ice bath. 4.0 g of $KMnO_4$ was gradually added to the reaction mixture under vigorous stirring and the temperature was kept below 20 °C. Then, the reaction mixture was moved from the ice bath to a water bath and was stirred for 6 h at 35 °C. Then, 200 mL of H_2O was slowly added to the mixture in an ice bath. After the dilution, 15 mL of 30% H_2O_2 was added, and the mixture was stirred for another 2 h. Then, the mixture was filtered and washed several times with distilled H_2O and then re-dispersed in H_2O by ultrasonication. Finally, the product was separated by centrifugation and was vacuum dried for 48 h at 45 °C.

4.3.1.4. Synthesis of CoNP on graphene oxide (CoNP-GO), & on O-CNT (CoNP-O-CNT)

3 mg of graphene oxide (GO), or oxidized carbon nanotube (O-CNT) was added to 15 mL of mixed solvent (3:2, 9 mL ethanol + 6 mL water). The resultant mixture was sonicated for 5 min, and then 300 mg cobalt precursor (cobalt acetate, $Co(CH_3COO)_2.4H_2O$) was added to the reaction mixture. The mixture was then stirred for 10 min to dissolve the precursor resulting in a

clear solution. After that, 1.5 mL of 25% ammonia was added to the solution under vigorous stirring. The reaction mixture was stirred for another 20 min and then transferred to a 20 mL microwave vial, and sealed with a PTFE lined cap. The reaction was performed in a Biotage™ Initiator 2.5 microwave reactor at 150 °C for 30 min. After that, the product was centrifuged and washed with H_2O via centrifugation-redispersion. Finally, the material was dried under vacuum at 60 °C overnight.

4.3.1.5. Sulfidation of the cobalt oxide/carbon hybrid materials

The CoNP on graphene oxide (CoNP-GO), and CoNP on oxidized carbon nanotube (CoNP-O-CNT) hybrid materials were converted to their corresponding sulfides. The oxide to sulfide conversion experiments were done in a laboratory-scale sulfurization apparatus (Scheme 1).

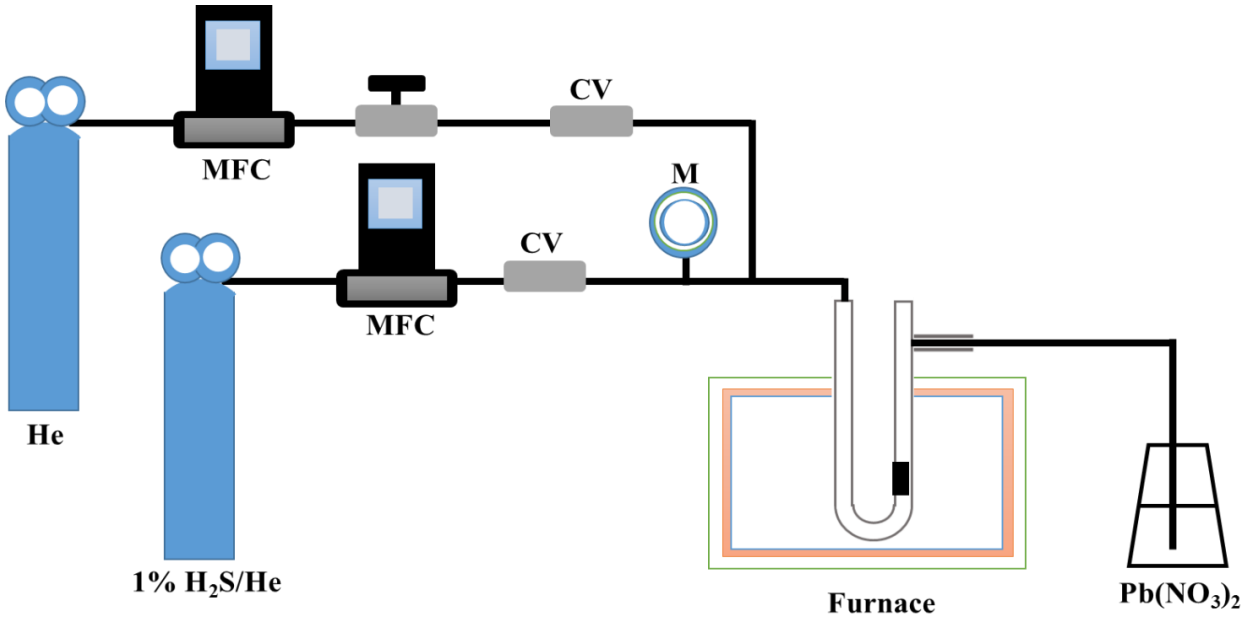

Scheme 4.1: Schematic diagram of the experimental setup for sulfurization.

The experimental setup consists of a fixed bed tubular reactor made of quartz with an internal diameter of 2 mm was oriented vertically in a tube furnace with programmable digital control under atmospheric pressure. The sample (50 mg) was packed in the reactor supported by quartz wool. Prior to each experiment, the sample was heated at reaction temperature and held for 1 h with a He flow of 36 sccm. The sulfidation reaction was carried out using a certified gas mixture of 1% H_2S in He.

4.3.2. Catalyst characterization

4.3.2.1. X-ray diffraction

The powder X-ray diffraction (PXRD) studies were performed with a Rigaku Ultima IV diffractometer using Cu Kα (λ = 0.15406 nm) radiation. The operating beam voltage was 40 kV, and a beam current of 44 mA was used. The data were collected in a range of 2θ, ranges from 5°-75° for wide angle XRD studies with a continuous scan rate of 2 °/min. The XRD patterns of the samples were collected on a glass sample holder. The crystallite size of the materials was calculated using the Debye-Scherer equation.

4.3.2.2. Scanning electron microscopy and energy dispersive X-ray spectroscopy

The morphology of the material was characterized using an FEI Nova NanoSEM FE-SEM with a beam current of 1.0 mA, and a Schottky emitter operating voltage of 2.0 kV. A FE-SEM sample was prepared by suspending the material in ethanol, and then a drop of the suspension was dispersed on Au coated silicon chips mounted onto stainless-steel sample holders with double sided carbon tape. The samples were dried under vacuum prior to analysis. The

EDX analysis was done using an Oxford X-max80 EDX analyzer operating at an electron accelerating voltage of 10 kV.

4.3.2.3. Transmission electron microscopy (TEM)

Transmission electron microscopy (TEM) and high resolution transmission electron microscopy (HR-TEM) studies were done using a JEOL 2010 UHR TEM instrument of an accelerating voltage of 200 kV, equipped with an energy dispersive X-ray analysis (EDS) system. The samples were prepared by dispersing the material in 2-propanol, and then a drop of the suspension was placed onto a carbon coated copper grid, and allowed to dry under infrared light.

4.3.2.4. Raman spectroscopy

Raman measurements were done at room temperature on a Renishaw 2000 Ramascope attached to a charge-coupled device (CCD) camera, with an Ar^+ ion laser (514 nm) as the excitation source. The spectrometer was calibrated with a silicon wafer before each of the measurements.

4.3.2.5. X-ray photo electron spectroscopy (XPS)

X-ray photoelectron spectroscopy (XPS) was done by PHI model 590 spectrometer with multiprobes (Φ Physical Electronics Industries Inc.), using Al-K radiation (λ = 1486.6 eV) as the radiation source. The powder samples were pressed on carbon tape mounted on adhesive copper

tape stuck to a sample stage placed in the analysis chamber. The XPS spectra were analyzed and fitted using CasaXPS software (version 2.3.12).

4.3.3. Electrochemical measurements

All the electrochemical measurements were performed in a three-electrode cell on a CHI 660A electrochemical workstation at room temperature. A standard calomel electrode (SCE) was used as a reference electrode, while a platinum wire was used as a counter electrode. The working electrode was prepared by coating the prepared material on pyrolytic graphitic carbon. First, the pyrolytic graphite (PG) was polished using silicon carbide grinding paper (before coating) to make a clean and smooth PG surface. The catalyst ink was prepared by mixing 4 mg of catalyst and 85 µL of Nafion in 1 mL of DI water/ethanol mixture (4:1). The catalyst ink mixture was then sonicated for 40 min. After sonication, 10 µL of the dispersed suspension was loaded onto the previously cleaned pyrolytic graphite substrate. Finally, the prepared working electrodes were air-dried overnight at room temperature before electrochemical measurements. The active loadings of the catalyst were 0.2 mg cm^{-1}. All electrochemical measurements for HER and OER activity of the catalysts were evaluated using linear sweep voltammetry (LSV) in acidic and basic media. High purity argon gas was purged for 30 min before start running the electrochemical measurements, with flowing the gas in the solution during the data collection.

4.4. Results

4.4.1. Structure

The X-ray diffraction patterns of synthesized cobalt oxide and hybrid materials are shown in Figure 4.1 (A). The wide angle powder XRD patterns of CoNP and CoNP-O-CNT materials can be assigned to cubic phase of Co_3O_4. The diffraction lines at 2θ = 31.2, 36.9, 44.7, 59.2, and 65.3 are indexed to (220), (311), (400), (511), and (440) planes of Co_3O_4 (pdf card number 01-073-1715 for CoNP).

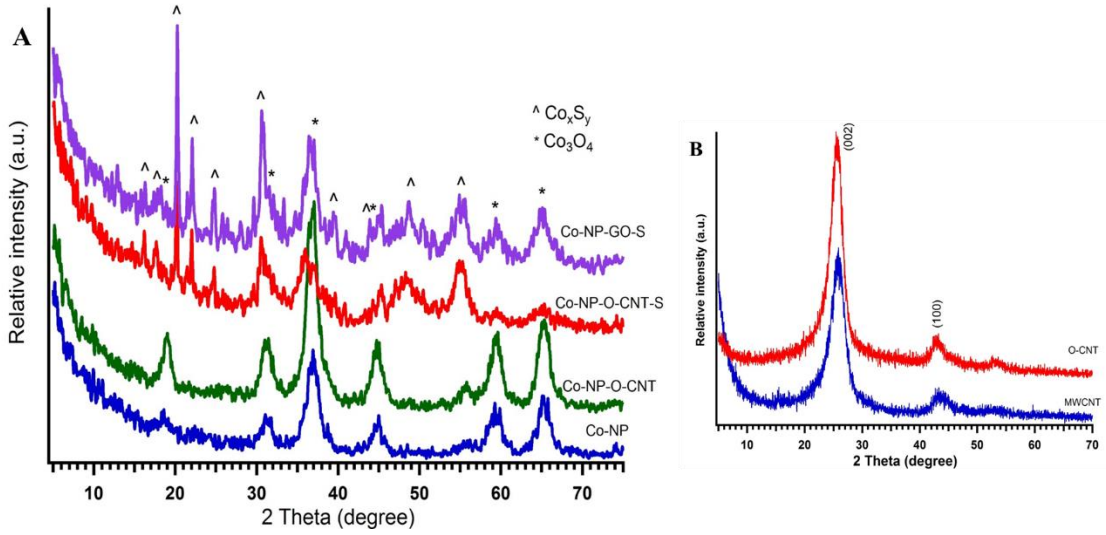

Figure 4.1. (A) Wide angle PXRD pattern of CoNP, CoNP-O-CNT, CoNP-O-CNT-S, and CoNP-GO-S materials; **(B)** Diffraction pattern of pristine, and oxidized carbon nanotube.

However, the Co_3O_4 material converts to Co_3S_4 with similar sulfidation process and previously reported.[24] XRD patterns of the synthesized hybrid materials indicate that, upon sulfidation, the oxide materials transform to corresponding sulfides, and show the mixed phase of Co_3O_4 and Co_xS_y. In Figure 4.1 (a), the cobalt oxide (*) and cobalt sulfide (^) peaks are

separated for the synthesized materials. Upon sulfidation, the intensities of cobalt oxide peaks gradually decrease while the cobalt sulfide peaks increase. Although, both oxide and sulfide peaks are more visible for CoNP-GO-S material, the CoNP-O-CNT-S material primarily shows the diffraction pattern for the cubic Co_3S_4 phase of cobalt sulfide (pdf card number 01-074-6715). However, CoNP-GO-S material shows low intensity peaks of CoS and Co_3O_4, along with the major peaks of the Co_3S_4 phase of cobalt sulfide (pdf card number 03-065-0407). These observations suggest that most of the oxygen in the Co_3O_4 structure was replaced by sulfur to give cobalt sulfide structure. The PXRD pattern of multi-wall carbon nanotube (MWCNT) and oxidized carbon nanotube (Figure 4.1B) indicates two characteristic peaks of (002) and (100) plane for the carbon nanotube. No diffraction peaks for O-CNT or GO were observed in the CoNP-O-CNP-S or CoNP-GO-S materials because of low amount and relatively lower diffraction intensities.

4.4.2. Morphology

Figure 4.2 (A & B) shows the aggregated nanoparticles of cobalt oxide (CoNP) material. The average size of the nanoparticles is ~7-8 nm. The two middle images (Figure 4.2 C & D) show that the nanoparticles are adhered to the oxidized carbon nanotube. In both of these cases, the nanoparticles are Co_3O_4 phase cobalt oxide. Figure 4.2 (E & F) shows the image of sulfided material (CoNP-O-CNT-S). The sulfided nanoparticles aggregated on the carbon nanotube.

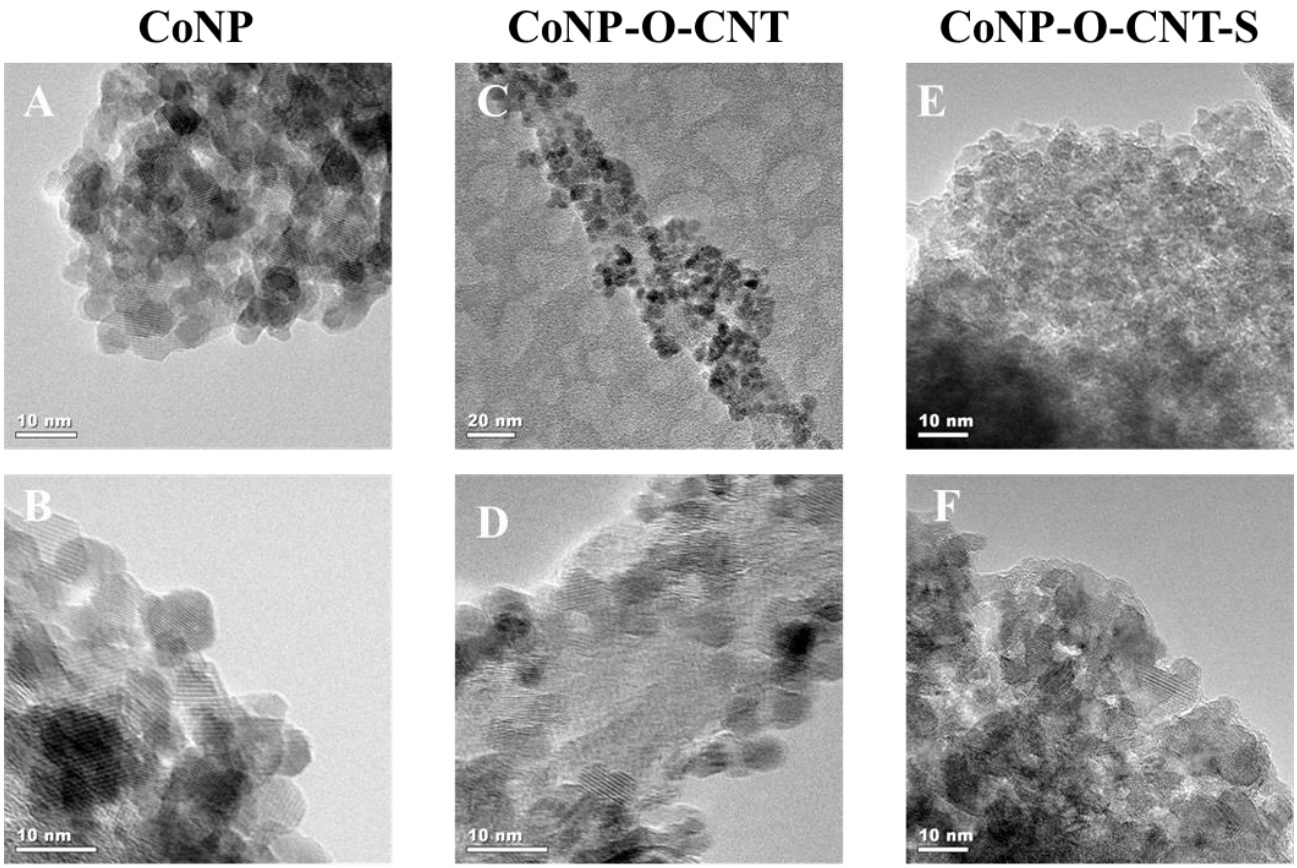

Figure 4.2. TEM images of **(A & B)** CoNP; **(C & D)** CoNP-O-CNT; and **(E & F)** CoNP-O-CNT-S.

SEM images and elemental mapping of CoNP-O-CNT-S material are shown in Figure 4.3. The SEM image of the sulfided material shows that the nanoparticles are aggregated to form big chunks. The elemental mapping obtained by EDX shows a uniform distribution of cobalt, oxygen, and sulfur throughout the material. The presence of oxygen indicates the material possesses both cobalt sulfide and cobalt oxide phases.

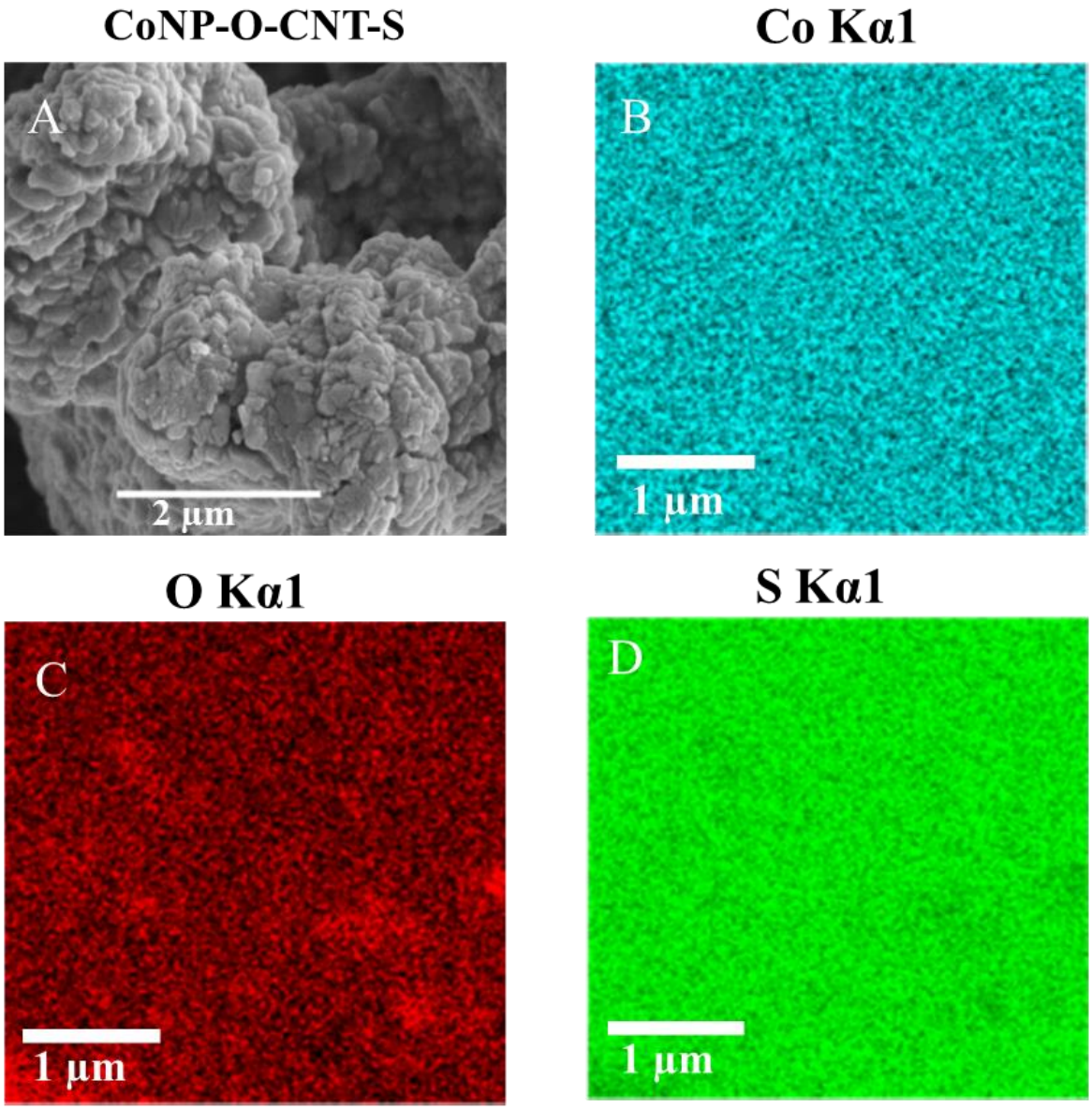

Figure 4.3. (A): SEM image; (**B), (C),** & **(D):** Elemental mapping of sulfided cobalt oxide on oxidized carbon nanotube (CoNP-O-CNT-S).

4.4.3. Raman analysis

The Raman spectra of different materials are presented in figure 4.4 (A-C). Figure 4.4 (A) shows two characteristic bands for pristine and oxidized carbon nanotube. The peaks at ~1354 cm^{-1} and ~1598 cm^{-1} are well-known as D and G bands, respectively, for carbon nanotubes and graphene oxide materials. The second order peak (Figure 4.4 B) at ~2750 cm^{-1} is known as a 2D band. In Figure 4.4 B, in the lower frequency region, every synthesized material shows all four characteristic peaks of Co_3O_4. The cobalt oxide/carbon hybrid materials show the characteristic D and G band peaks of GO and O-CNT along with low frequency cobalt oxide peaks.

In Figure 4.4 (C), the lower frequency region is highlighted for cobalt oxide/carbon hybrid and corresponding sulfided materials. The Raman peaks at ~482 cm^{-1}, ~519 cm^{-1}, ~621 cm^{-1}, and ~690 cm^{-1} are the characteristic peaks of spinel Co_3O_4 structure. The highlighted part of the Figure 4.4 (C) shows the A_{1g} peak shifting towards lower frequency for the CoNP-O-CNT-S material compare to corresponding oxide materials.

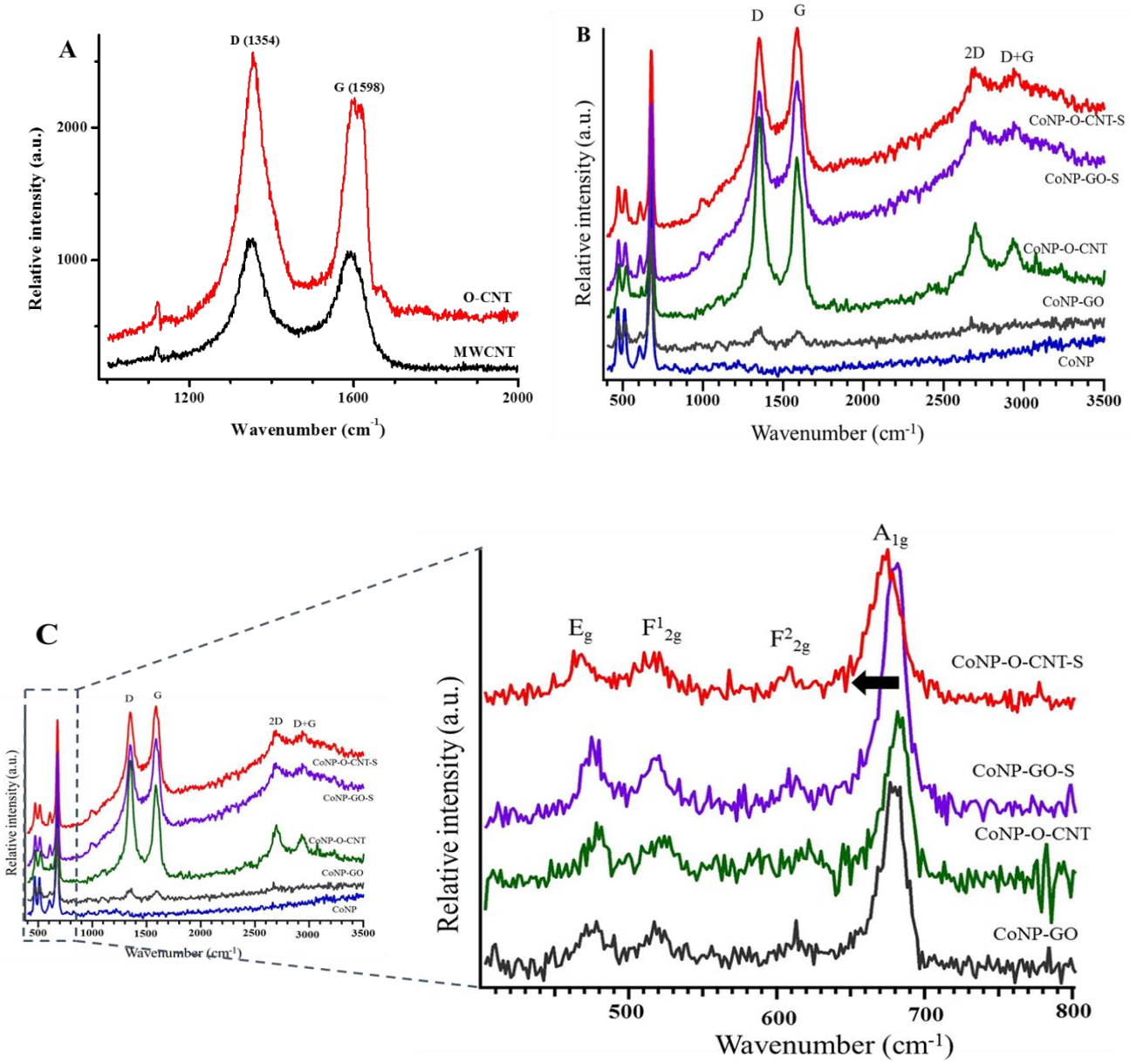

Figure 4.4. Raman spectra of **(A)** Pristine carbon nanotube (MWCNT) and oxidized carbon nanotube (O-CNT); **(B)** full spectrum of CoNP and different hybrid materials, and **(C)** highlighted lower frequency region with full spectrum.

4.4.4. XPS

The X-ray photoelectron spectroscopy (XPS) was employed to study the composition of the CoNP-O-CNT-S material. The XPS survey spectrum is shown in Figure 4.5 (A), which confirms the presence of Co, C, O, and S in the CoNP-O-CNT-S materials. The Co 2p peak at 779.4 eV and the S 2p at 162.5 eV are characteristic of cobalt sulfide. The high-resolution Co 2p XPS spectrum of the material demonstrates a peak at 779.4 eV, corresponding to Co $2p_{3/2}$, which is the characteristic peak of Co_3S_4. This peak also confirms the presence of mixed valences of Co (Co^{2+}, Co^{3+}) in the samples. The peaks at 794.1 eV and 781.8 eV can be ascribed to a Co-O bond, suggesting incomplete sulfidation of the materials. The existence of Co_3S_4 can be further verified by evident peaks at 162.5 eV and 164.4 eV in Figure 4.5 (B), which could be assigned to be the spin–orbit couple of S $2p_{3/2}$ and S $2p_{1/2}$, respectively. The peak S 2p peak at 161-163 eV suggests that the S species exist as S^{2-} in the material, corresponding to the binding energy of Co-S bonds.[25]

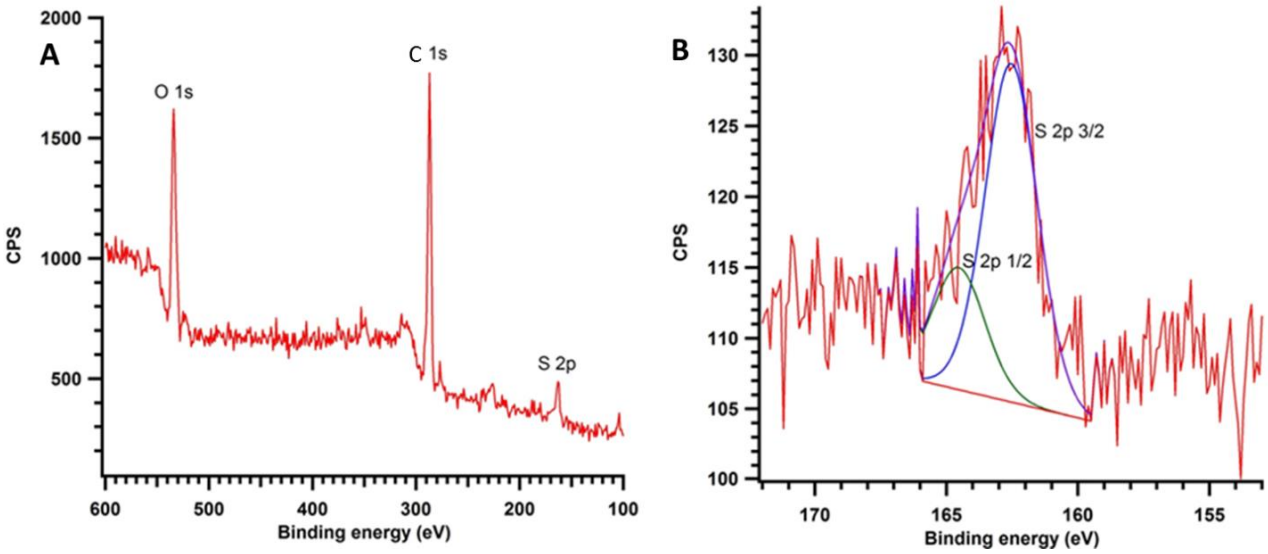

Figure 4.5. (A) XPS survey spectra of CoNP-O-CNT-S material, and **(B)** high-resolution spectra for S 2p.

4.4.5. Electrocatalytic results

4.4.5.1. Initial catalytic activities of as-synthesized materials

Initially, cobalt oxide nanoparticles and sulfided cobalt oxide nanoparticles were synthesized, and their electrocatalytic performance was evaluated in both acidic and basic media.

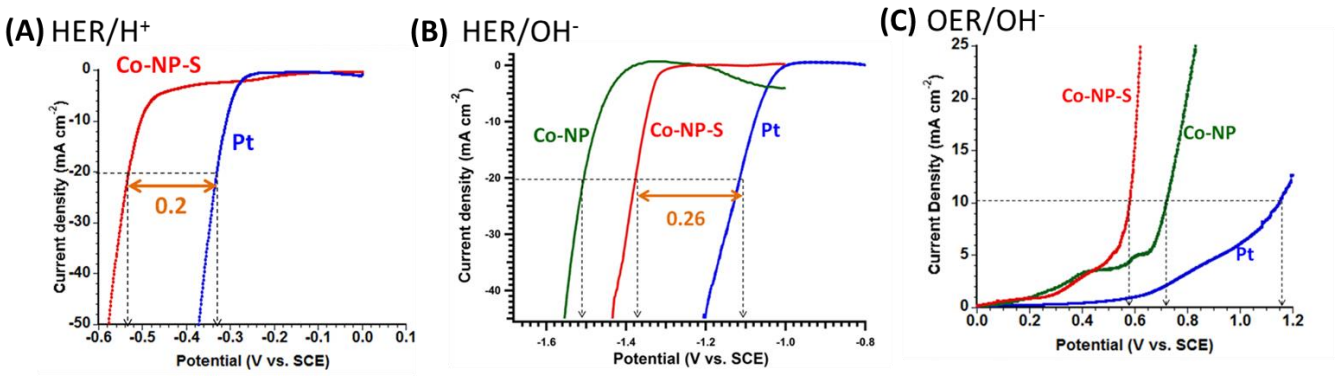

Figure 4.6. LSV curves for (A) HER in 0.5 M H_2O_4; (B) HER in 0.1 M KOH; and (C) OER in 0.1 M KOH for CoNP and CoNP-S materials.

The electrocatalytic performance of the materials was initially evaluated for both HER and OER. The activities were compared to Pt under the same conditions. Figure 4.6 shows the Linear Sweep Voltammetry (LSV) results of catalysts carried out under different pH condition. The HER activities of the CoNP and CoNP-S materials were estimated in both acidic and basic media whereas the OER activities were performed only in basic media. The HER activity of the catalysts in acidic media found better than that of in basic media (Figure 4.6 A & B). The difference in the overpotentials of CoNP-S with Pt (at a current density of 20 mA/ cm^2) in acidic solution was 0.2 volts while that of in basic media was 0.26 volts, indicating better HER activity under acidic conditions for the materials.

4.4.5.2. HER activities of synthesized hybrid materials in acidic media

Figure 4.7 shows the HER polarization curves of CoNP, CoNP-GO, CoNP-GO-S, CoNP-O-CNT, CoNP-O-CNT-S, and a benchmark Pt. The CoNP-O-CNT-S material exhibits the best catalytic behavior with the lowest overpotential (360 mV vs SCE) at a current density of 10 mA/cm^2. HER activities are usually evaluated by comparing the overpotenstials required to reach a current density of 10 mA/cm^2, which is a relevant metric of a practical solar fuel cell. CoNP-O-CNT-S materials display the lower overpotentials to reach a current density of 10 mA/cm^2. The results of HER activity for all the materials are summarized in Table 4.1.

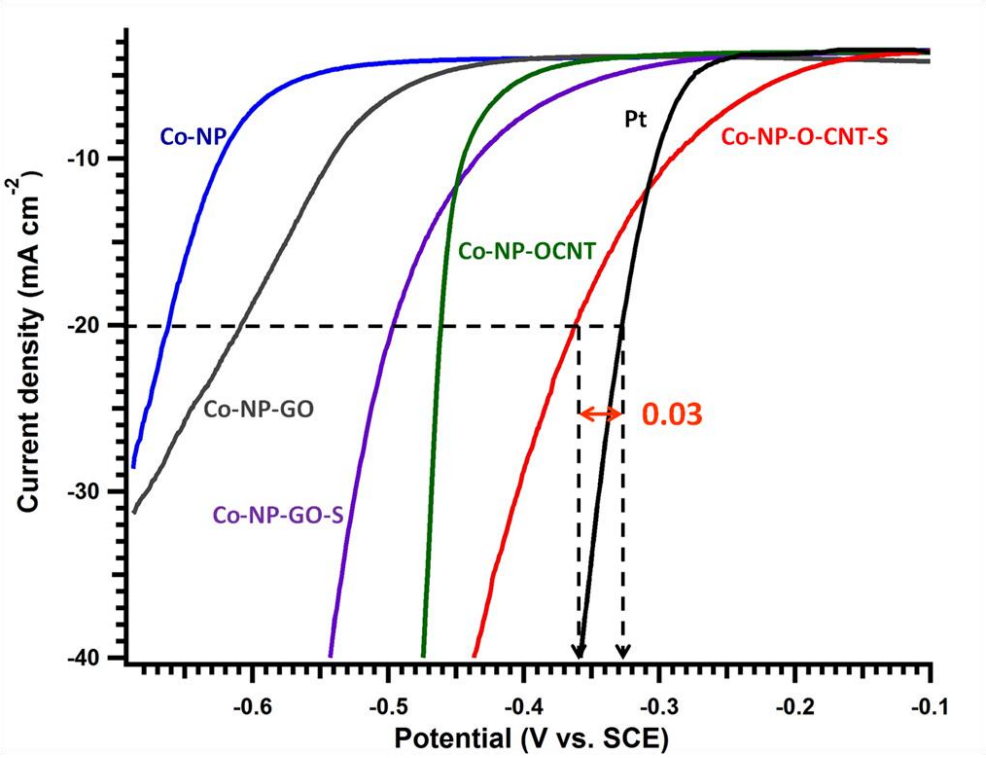

Figure 4.7. Polarization curves for HER on GC electrode modified with different materials.

Table 4.1. Summary of the results of HER activity in acidic media for different materials.

Catalyst	**Potential (V vs SCE) at -20 mA cm^{-2}**	**Onset potential (V vs SCE)**
CoNP	-0.66	-0.55
CoNP-GO	-0.61	-0.44
CoNP-GO-S	-0.49	-0.28
CoNP-O-CNT	-0.46	-0.36
CoNP-O-CNT-S	-0.36	-0.17
Pt	-0.33	-0.25

4.5. Discussion

The electrochemical water splitting consists of two half reactions, oxidation half reaction, which happens at the anode, and reduction half reaction, happens at the cathode. The reduction of hydrogen ion (H^+) at the cathode produces hydrogen gas, and this process proceeds through two different mechanistic steps. First, the adsorption of the H^+ occurs on the cathode (Volmer step); then the adsorbed hydrogens (H_{ad}) combine with each other or react with another H^+ and e^- to form H_2 gas (Heyrovsky/Tafel step) and get desorbed.[26] Therefore, the efficiency of an HER catalyst depends on proton (H^+) adsorption/desorption capability and on the surface electronic environment of the cathode material.

In this work, the HER result shows that the sulfided materials are more active than corresponding oxides. The electronic environment in Co-S bonding is different from Co-O bonding because of the difference in electronegativity difference of S and O. Sulfur makes a moderate bonding with cobalt, which facilitates the H^+ adsorption-desorption step, hence increases the activity. XRD patterns of the synthesized materials indicate that the sulfur is bonded to cobalt as Co_3S_4, CoS, or as CoS_2 in the sulfided materials. Thus all the sulfided materials showed better activity than the corresponding oxides. A TEM image of CoNP material (Figure 4.2 A&B) shows the nanoparticles are aggregated, while the oxide and sulfide nanoparticles are well dispersed on high surface area O-CNT (Figure 4.2 C-D) in the hybrid materials. The element mapping (Figure 4.3 B-D) shows the S, Co and O are well dispersed throughout the material. Thus, well distributed nanoparticles, mixed oxide and sulfide phase create defects on the surface of the material and makes the hybrid material more active towards HER.

Raman studies show that the characteristic Co-O peak of Co_3O_4, shifts towards the lower frequency region for the CoNP-O-CNT-S material, which indicates that relatively longer bonds form between Co-S (as S is bigger in size then O, and O is more electronegative than S). The D and G bands in the hybrid materials also confirm the presence of GO or CNT. The relative intensities of the D and G bands indicate the disorders present in the material. The higher the G band intensity, the higher is the disorder in the system. The I_G/I_D is higher in the hybrid materials compared to I_G/I_D in O-CNT or MWCNT. These defects or disorders enhance the catalytic activity of the sulfided material.

The incorporation of the CNT materials plays a very important role for HER catalytic activity of the hybrid materials. CNT is a very conductive and porous material, which increases

the electronic and ionic transport in the system. The HER reaction is highly dependent on the electron availability on the surface of the materials. In addition, during sulfidation, carbon nanotubes might have also been doped with S atom, and sulfur doped CNT is a highly efficient catalyst for oxygen evolution and reduction reactions.[27]

The results of the HER activities show the following trend CoNP < CoNP-GO < CoNP-GO-S < CoNP-O-CNT < CoNP-O-CNT-S, and the trend is in very good agreement with the structure of the materials. The synergistic effect of the moderate Co-S bond, the presence of S throughout the material, good distribution of the nanoparticles on CNT, and finally, high surface area and conductivity of carbon nanotubes have made the cobalt oxide-cobalt sulfide/carbon hybrid material a promising transition metal oxide-based, low-cost electrocatalyst.

4.6. Conclusion

Cobalt oxide-cobalt sulfide/carbon hybrid materials were successfully synthesized, and their electrocatalytic performance was evaluated by the hydrogen evolution reaction (HER). The cobalt oxide-cobalt sulfide/oxidized carbon nanotube (CoNP-O-CNT-S) hybrid material showed promising activity for the HER reaction. The excellent HER activity of the hybrid material could be attributed to the incorporation of the porous and highly conductive carbon nanotubes, which enhance the transport of electrons and, hence, increase the activity. Furthermore, cobalt oxide-cobalt sulfide nanoparticles could also be uniformly distributed on the high surface area O-CNT, resulting in more exposed active sites. Finally, the synergistic effect of moderate metal sulfide bonding and possible incorporation of sulfur into the carbon network improved the catalytic activity of the sulfided hybrid materials for HER.

Reference list

(1) Reier, T.; Oezaslan, M.; Strasser, P. *ACS Catal.* **2012**, *2*, 1765.

(2) Jin, H.; Wang, J.; Su, D.; Wei, Z.; Pang, Z.; Wang, Y. *J. Am. Chem. Soc.* **2015**, *137*, 2688.

(3) Jahan, M.; Liu, Z.; Loh, K. P. *Adv. Funct. Mater.* **2013**, *23*, 5363.

(4) Meng, Y.; Song, W.; Huang, H.; Ren, Z.; Chen, S.-Y.; Suib, S. L. *J. Am. Chem. Soc.* **2014**, *136*, 11452.

(5) Chemelewski, W. D.; Lee, H.-C.; Lin, J.-F.; Bard, A. J.; Mullins, C. B. *J. Am. Chem. Soc.* **2014**, *136*, 2843.

(6) Du, P.; Eisenberg, R. *Energy Environ. Sci.* **2012**, *5*, 6012.

(7) Hutchings, G. S.; Zhang, Y.; Li, J.; Yonemoto, B. T.; Zhou, X.; Zhu, K.; Jiao, F. *J. Am. Chem. Soc.* **2015**, *137*, 4223.

(8) Maiyalagan, T.; Jarvis, K. A.; Therese, S.; Ferreira, P. J.; Manthiram, A. *Nat. Commun.* **2014**, *5*.

(9) Zhang, M.; De Respinis, M.; Frei, H. *Nat. Chem.* **2014**, *6*, 362.

(10) Zou, X.; Huang, X.; Goswami, A.; Silva, R.; Sathe, B. R.; Mikmeková, E.; Asefa, T. *Angew. Chem.* **2014**, *126*, 4461.

(11) Gong, M.; Zhou, W.; Tsai, M.-C.; Zhou, J.; Guan, M.; Lin, M.-C.; Zhang, B.; Hu, Y.; Wang, D.-Y.; Yang, J. *Nat. Commun.* **2014**, *5*.

(12) Zhang, Z.; Hao, J.; Yang, W.; Tang, J. *RSC Adv.* **2016**, *6*, 9647.

(13) Wang, Y.; Tang, J.; Kong, B.; Jia, D.; Wang, Y.; An, T.; Zhang, L.; Zheng, G. *RSC Adv.* **2015**, *5*, 6886.

(14) Sun, Y.; Liu, C.; Grauer, D. C.; Yano, J.; Long, J. R.; Yang, P.; Chang, C. J. *J.*

Am. Chem. Soc. **2013**, *135*, 17699.

(15) Chen, Z.; Cummins, D.; Reinecke, B. N.; Clark, E.; Sunkara, M. K.; Jaramillo, T. F. *Nano Lett.* **2011**, *11*, 4168.

(16) Jin, B.; Zhou, X.; Huang, L.; Licklederer, M.; Yang, M.; Schmuki, P. *Angew. Chem. Int. Ed.* **2016**, *55*, 12252.

(17) Imran, M.; Yousaf, A. B.; Zaidi, S. J.; Fernandez, C. *Int. J. Hydrogen Energy* **2017**, *42*, 8130.

(18) Jaramillo, T. F.; Jørgensen, K. P.; Bonde, J.; Nielsen, J. H.; Horch, S.; Chorkendorff, I. *Science* **2007**, *317*, 100.

(19) Zhang, L. L.; Zhao, X. *Chem. Soc. Rev.* **2009**, *38*, 2520.

(20) Pham, K.-C.; McPhail, D. S.; Wee, A. T.; Chua, D. H. *RSC Adv.* **2017**, *7*, 6856.

(21) Khan, M.; Yousaf, A. B.; Chen, M.; Wei, C.; Wu, X.; Huang, N.; Qi, Z.; Li, L. *Nano Res.* **2016**, *9*, 837.

(22) Chinnappan, A.; Baskar, C.; Kim, H.; Ramakrishna, S. *J. Mater. Chem. A* **2016**, *4*, 9347.

(23) Dong, Y.; He, K.; Yin, L.; Zhang, A. *Nanotechnology* **2007**, *18*, 435602.

(24) Pahalagedara, L. R.; Poyraz, A. S.; Song, W.; Kuo, C.-H.; Pahalagedara, M. N.; Meng, Y.-T.; Suib, S. L. *Chem. Mater.* **2014**, *26*, 6613.

(25) Huang, K.-J.; Zhang, J.-Z.; Shi, G.-W.; Liu, Y.-M. *Mater. Lett.* **2014**, *131*, 45.

(26) Benck, J. D.; Hellstern, T. R.; Kibsgaard, J.; Chakthranont, P.; Jaramillo, T. F. *ACS Catal.* **2014**, *4*, 3957.

(27) El- Sawy, A. M.; Mosa, I. M.; Su, D.; Guild, C. J.; Khalid, S.; Joesten, R.; Rusling, J. F.; Suib, S. L. *Adv. Energy Mater.* **2015**.

Ongoing work

CHAPTER 5. SYNTHESIS OF BLACK TITANIA (TIO_2) NANOMATERIALS FOR VISIBLE LIGHT PHOTOCATALYTIC ACTIVITY

5.1. Overview

Titanium dioxide (TiO_2) nanomaterial was synthesized by an inverse micelle templated sol-gel synthesis method and then hydrogenated to obtain black titania nanomaterials. The materials were characterized with XRD, and TEM and applied in photocatalytic applications of degradation under visible light irradiation. The results show that in 4 h ~ 93% of a methylene blue dye was degraded by *in situ* black titania under visible light. The *in situ* black titania was synthesized by direct hydrogenation during calcination, whereas the post treated black titania was synthesized by hydrogenation of the calcined TiO_2. Both *in situ* and post treated black titania materials showed crystalline anatase phase, while the *in situ* material was less crystalline compared to the post hydrogenated black TiO_2. Further study is needed to investigate the relationship between the photocatalytic activity and the structure of the materials.

5.2. Introduction

Over the past decades, photocatalysis has been regarded as one of the best solutions to important chemical process such as environmental remediation and solar fuel production. Among photocatalysts, titanium dioxide (TiO_2) is a widely used material because of it's abundance, low-

cost, photostablility, and widespread applications.[1] Two of the most important applications are photocatalytic water splitting to produce hydrogen and removal of organic pollutants from the environment.[2,3] TiO_2 semiconductor photocalysts have three major crystal phases: anatase, rutile, and brookite. All of these phases have an electronic band gap of 3.0-3.2 eV and absorb solar energy from the UV-region of the solar spectrum.[4] The UV region is less than 5% of the total solar energy, which limits the application of the TiO_2 as a photocatalyst.[5] However, numerous methods have been developed to narrow the band gap and make titania a visible light active photocatalyst. Among these techniques, doping with metals and non-metals is a common method to prepare visible light active colored TiO_2.[6-8] Although these colored TiO_2 materials are more active than typical white TiO_2 materials under visible light, they absorb only a small part of the visible light and get excited to be active in photocatalytic reactions. In 2011, a new type of TiO_2 photocatalyst was introduced as black titania, which has better activity compared to all titania materials in visible light.[9] Since it's activity has been revealed, black titania has drawn huge attention in photocatalysis. However, in most cases the synthetic process requires long preparation time and high pressure hydrogenation treatment.[10]

In photocatalytic processes, active materials absorb light with greater energy than its band gap and create vacancies in the valance band and excited electrons in the conduction band.[11,12] These excited charges migrate to the surface of the material to perform the photocatalytic reactions. The photocatalytic activity depends on the number of holes created in the valence band and number of electrons in the conduction band of the material. The lower the band gap of the photocatalysts, the higher are the chances to absorb sunlight, leading to more excited charged species (holes and electrons) on the surface of the materials. While creating the excited species, some of the holes and electrons may recombine and disappear. Therefore, the

more light is being absorbed by TiO_2, the more active sites will be on the surface of the material, resulting in the enhancement of the overall catalytic activity. Recently, black TiO_2 materials prepared by hydrogenating the white TiO_2 nanocrystals has drawn attention due to having a narrow band gap (~1.5 eV) and high photocatalytic performance.[9] In hydrogenated black titania, hydrogen inserts into the crystal lattice of the TiO_2 and introduces an intermediate electronic state, which facilitates increased solar absorption.[9,13]

During the effort of making colored TiO_2 material for high optical absorption, a series of metal ions have been used to replace Ti^{4+} ions and also non-metals to replace the O^{2-} ions in the TiO_2 lattice.[14-17] Oxygen vacancies and Ti^{3+} can introduce defects on the surface of the material and enhance the catalytic activity. Mao and co-workers are one of the pioneers in reporting this excellent photocatalytic behavior of hydrogenated black titania nanomaterials.[9] In their study, they introduced disorder in the surface of nanophase titania through hydrogenation at high pressure (20 bar H_2 pressure, 5 days), which dramatically changed the structure and properties of the TiO_2 nanoparticles. The Zhao group reported ordered mesoporous black TiO_2 for efficient hydrogen evolution photocatalysts.[18] They synthesized high surface area ordered mesoporous TiO_2 as the precursor for subsequent hydrogenation at 500 °C under H_2 flow for 3 h. Shunhang and co-workers reported a one-step synthetic approach for core-shelled anatase black titania with high visible light photocatalytic performance.[19] Wang and Chou compare the photocatalytic activity of black titania prepared by hydrogen plasma and hydrogen thermal treatment.[20] They synthesized the TiO_2 nanowire array by hydrothermal methods for hydrogenation. Recently, hydrogen plasmas have been used by different research groups to make black titania for increased absorption.[21-23]

In this study, black titania was prepared by hydrogenation at atmospheric pressure. Prior to that, mesoporous titanium dioxide was synthesized by University of Connecticut (UCT) mesoporous material synthesis method.[24] This synthetic approach has been applied for many materials with exceptional catalytic activities.[25-27] The synthesized black titania nanomaterials exhibit the anatase crystal structure and show high photocatalytic performance in organic dye degradation.

5.3. Experimental

5.3.1. Chemicals

Titanium (IV) isopropoxide (≥ 97%), 1-butanol (anhydrous, 99.8%), and poly(ethylene glycol)-*block*-poly(propylene glycol)-*block*-poly(ethylene glycol), PEO_{20}-PPO_{70}-PEO_{20} (Pluronic P123, MW: 5750 $gmol^{-1}$) were purchased from Sigma-Aldrich. Concentrated nitric acid (HNO_3, 68-70%) was purchased from J. T. Baker. Methylene blue, the model dye, was purchased from Sigma-Aldrich. All chemicals and reagents were used as received.

5.3.2. Synthesis of catalysts

Three different titanium dioxide (TiO_2) materials were synthesized for this work. First, the mesoporous TiO_2 was synthesized and calcined at 500 °C for 4 h under air, which was labeled as BT-0. Then, the mesoporous titania was further hydrogenated by 5% H_2 in Ar mixture at different temperatures for 48 h to observe the color change of the materials. For the *in situ* material, the as synthesized TiO_2 film like material was calcined under the H_2/Ar gas mixture

flow at 500 °C for 4 h at a heating ramp rate of 1 °C/min, and the material was labeled as '*in situ* B. TiO_2'.

5.3.2.1. Synthesis of mesoporous TiO_2

Mesoporous TiO_2 materials were synthesized using the inverse micelle templated sol-gel method.[28] In a typical synthesis, 7.0 g (0.094 mol) of 1-butanol, 1.0 g (0.016 mol) of HNO_3 and 1.0 g (1.72×10^{-4} mol) of P123 were mixed in a 150 mL beaker at room temperature. Titanium isopropoxide (2.84 g, 0.01 mol) was added dropwise to the above mixture under magnetic stirring. Before addition, the titanium isopropoxide was bubbled with N_2 for 2-3 min. Then the reaction mixture was stirred for 20 min to obtain a clear gel and afterward placed in oven for 4 h at 120 °C. Film like titanium dioxide material was obtained after ~ 4 h, which was further calcined at different conditions. The as synthesized material was calcined at 500 °C under air for 4 h with a heating rate of 1 °C/min. Finally, the calcined white TiO_2 powder was labeled as BT-0, and this material was used as the starting material for the further hydrogenation. The *in situ* black titanium dioxide (labeled as *in situ* B. TiO_2) material was obtained by calcining the as synthesized film like material under H_2/Ar gas mixture at 500 °C for 4 h with a similar heating rate of 1 °C/min.

5.3.2.2. Hydrogenation of TiO_2

The reduction was performed under a gas mixture of 5% H_2 in Ar with a flow rate of 20 sccm. The following setup was used for all the reduction experiments:

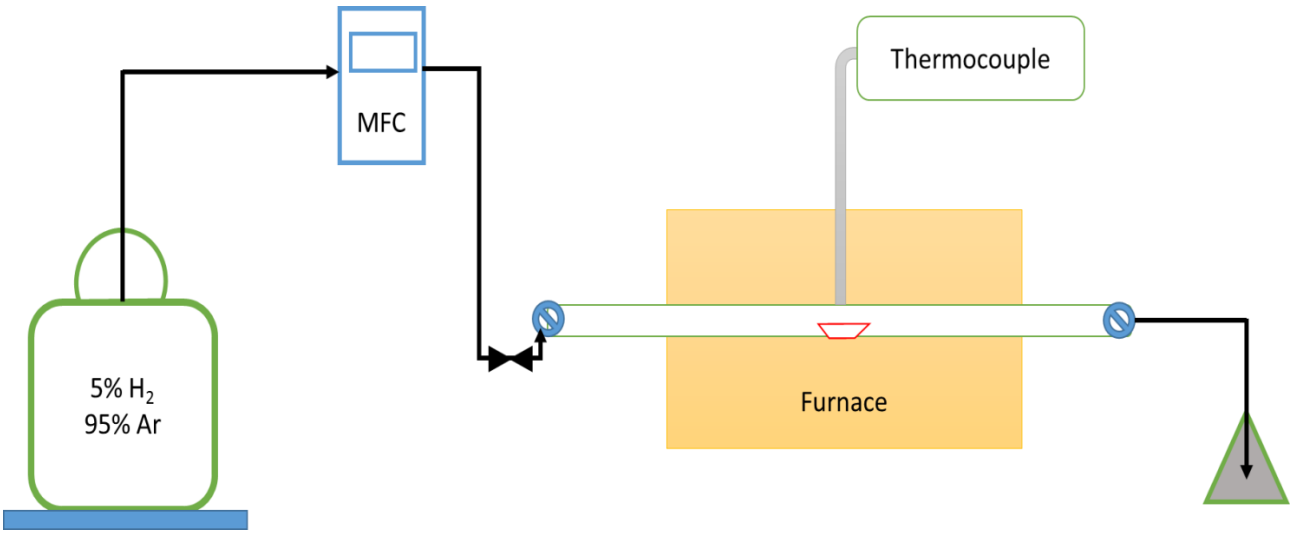

Scheme 5.1. Setup for the reduction (hydrogenation) experiments of the synthesized titanium dioxide materials.

The 500 °C calcined white titanium dioxide material (BT-0) was hydrogenated at different temperatures of 300, 400, 450, and 500 °C for 48 h. Based on the hydrogenation temperature, the 300, 400, 450, and 500 °C samples were labeled as BT-1, BT-2, BT-3, and BT-4 respectively. The colors of the samples were monitored after each heating cycle. TiO_2 (100 mg) sample (BT-0) was loaded on a crucible and was put into a tube furnace (Scheme 5.1). The temperature of the furnace was controlled by a thermocouple, and the hydrogenation was performed at atmospheric pressure.

5.3.3. Characterization

5.3.3.1. X-ray diffraction

Powder X-ray diffraction (PXRD) studies were performed with a Rigaku Ultima IV diffractometer (Cu Kα radiation, λ = 1.5406 Å) with an operating voltage of 40 kV and a current of 44 mA. The wide-angle PXRD were collected over a 2θ range of 5-75° with a continuous scan rate of 2° per min.

5.3.3.2. Transmission electron microscopy

Transmission electron microscopy (TEM) was also used to study the morphology and structure of the catalysts. High-resolution transmission electron microscopy (HR-TEM) and scanning transmission electron microscopy (STEM) measurements were carried out using a Talos F200X microscope operating at 200 kV equipped with an energy dispersive X-ray spectroscopy (EDS) detector.

5.3.4. Photocatalytic reaction

Methylene blue (319.85 g/mol) was used as a model dye to study the photocatalytic activity of the synthesized black TiO_2 materials. White light lamps (λ_{peak} = 575 nm, 8 W) were used as constant, separate, and intense sources of visible light, and sixteen of those lamps were installed equally spaced on a Rayonet Model RPR-200 photochemical chamber reactor. The reactor and lamps were purchased from Southern New England Ultraviolet Co., CT. This type of photochemical reactor has been recently used to mimic sunlight for pollutant degradation.[29]

Methylene blue dye solution of 10 ppm concentration was prepared by dissolving relative amounts of dye in DDW. This dye solution (20 mL) and 10 mg of the prepared catalyst taken in a 120 mL beaker and was stirred for 2 h in dark to eliminate adsorption effect. Then the reaction mixture was stirred under visible light irradiation for the next 4 h in the photoreactor. The beaker was covered with a watch glass to minimize water evaporation and interference from the atmosphere. Finally, samples were centrifuged and uv-visible spectra were collected for all samples.

5.4. Results

5.4.1. Color of the synthesized material

The color of the hydrogenated samples changed with reduction time and temperature. The synthesized film like material was calcined at 500 °C under air, and the sample was white in color (BT-0). This white sample was the starting material for the hydrogenation process. Another calcination of the film like material was also done under 5% H_2 in Ar gas mixture, and the sample was black after calcination and labelled as *in situ* black titania (*in situ* B. TiO_2).

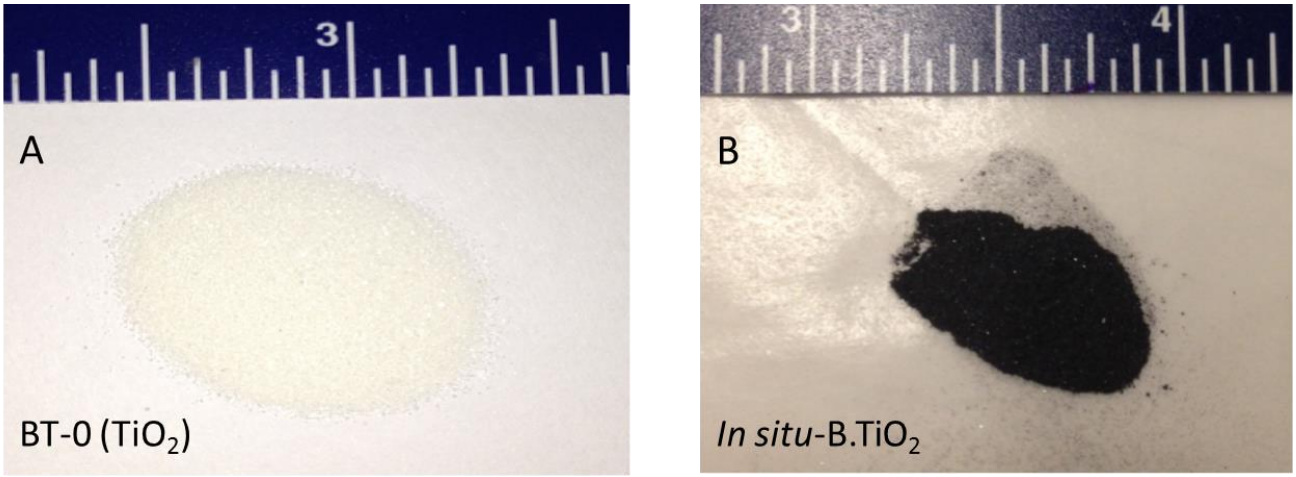

Figure 5.1. Sample (A) is the white titanium dioxide material, calcined at 500 °C for 4 h, which is the starting material for hydrogenation; (B) *In situ* back TiO_2, the as-synthesized material calcined under H_2/Ar gas mixture.

The 500 °C calcined white sample (BT-0) was hydrogenated at different temperatures. After 48 h, the sample was brown at 300 °C temperature (BT-1), and at 400 °C the sample became gray (BT-2). Then the white sample (BT-0) was hydrogenated at 450 °C; the color became dark gray after 48 h (BT-3). The sample was black after 48 h, when hydrogenated at a temperature of 500 °C (BT-4). Hence, 500 °C is the lowest temperature to make black titanium dioxide after 48 h of hydrogenation.

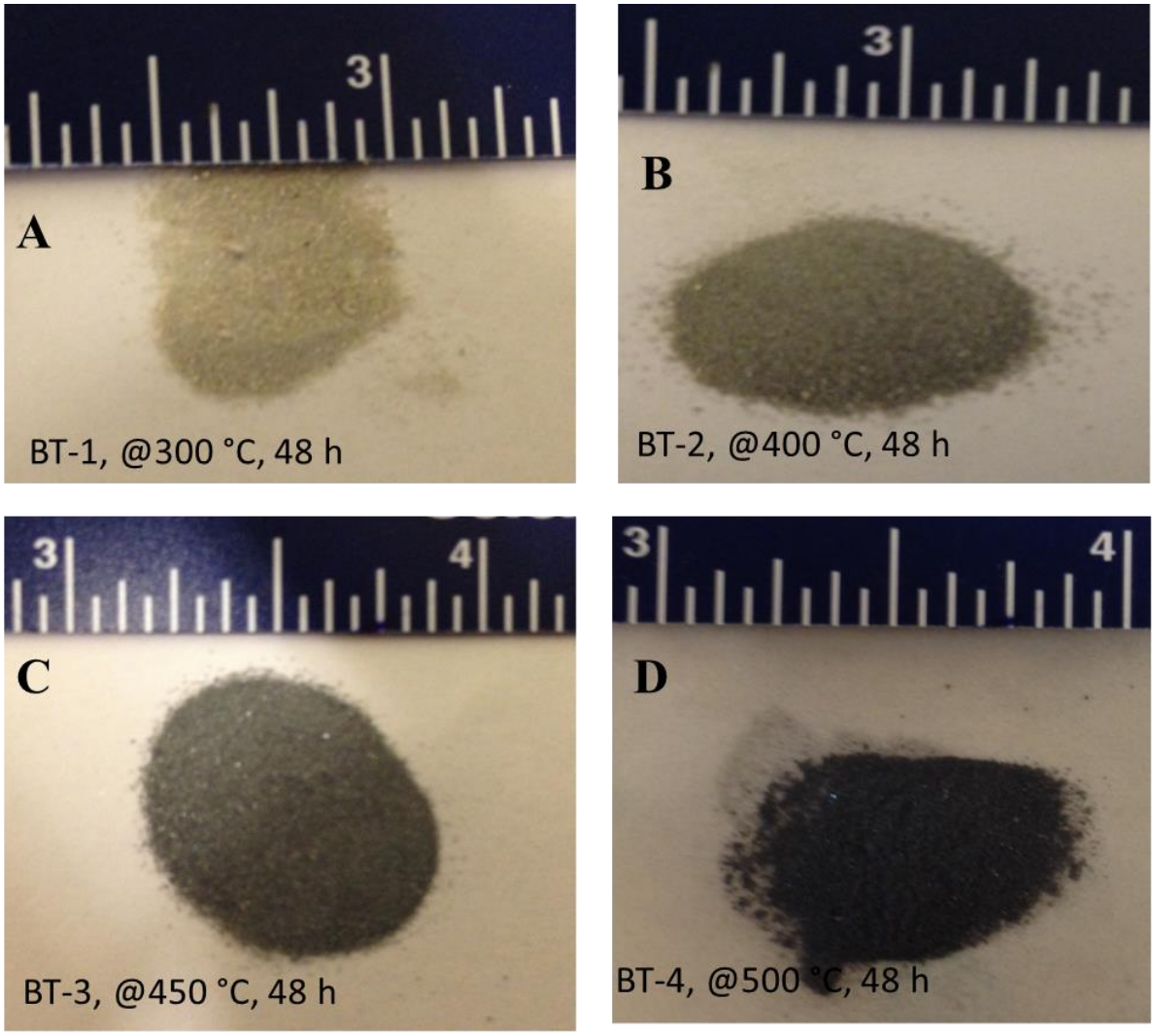

Figure 5.2. Hydrogenated samples after 48 h, (A) at 300 °C, (B) at 400 °C, (C) at 450 °C, and (D) at 500 °C.

5.4.2. Structure of the materials

Wide angle PXRD was used to identify the crystal phase of the synthesized TiO_2 materials. The *in situ* material (*in situ* B. TiO_2) shows lower crystallinity compared to the other samples. The X-ray diffraction patterns of the all three synthesized materials represent the

anatase crystalline phase of titanium dioxide (PDF card numbers, for BT-0: 01-089-4203, for BT-4: 01-076-3177; and for *in situ* B. TiO_2: 01-075-2544). The crystallite size of the *in situ* material (46 nm) is also smaller compared to the post hydrogenated black titania (BT-4, 166 nm).

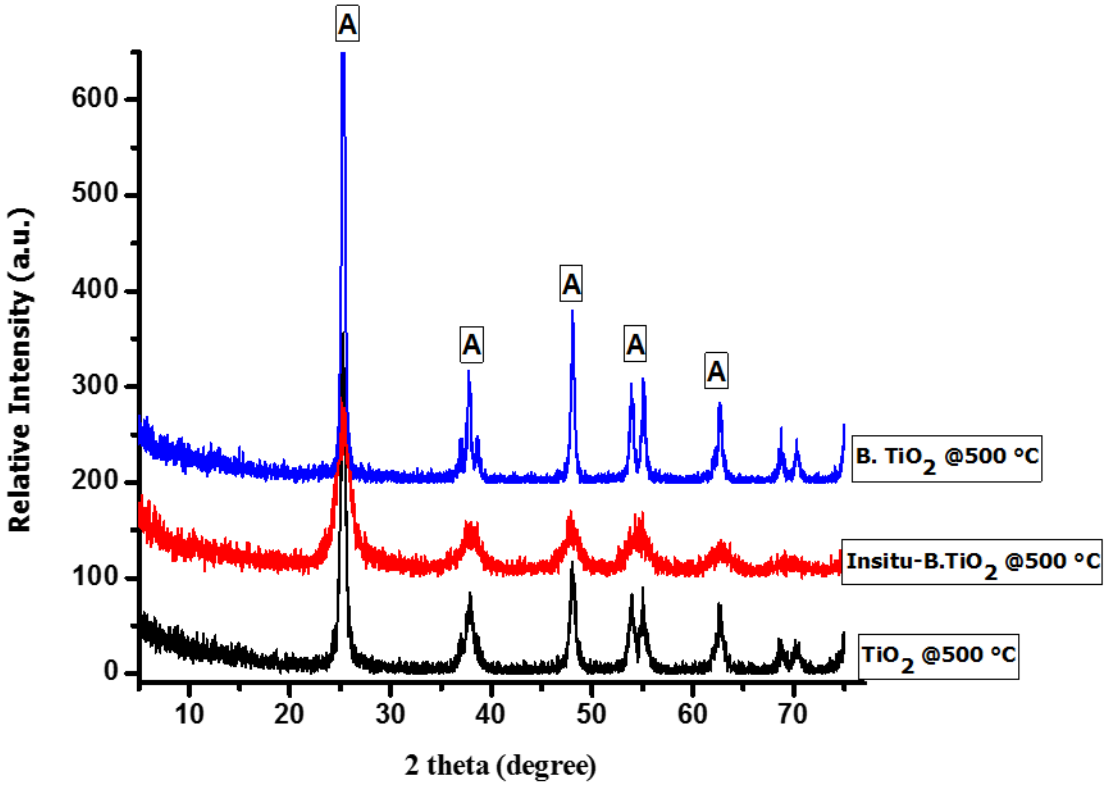

Figure 5.3. X-ray diffraction pattern of different titanium dioxide materials.

5.4.3. Morphology of the materials

The morphologies of the synthesized black TiO_2 nanomaterials are shown in Figures 5.4 and 5.5. All the images in Figure 5.4 show the aggregation of the nanoparticles and the crystallinity of the materials. Whereas in Figure 5.4. (C), the *in situ* material shows less crystallinity, which is a good agreement with the X-ray diffraction patterns.

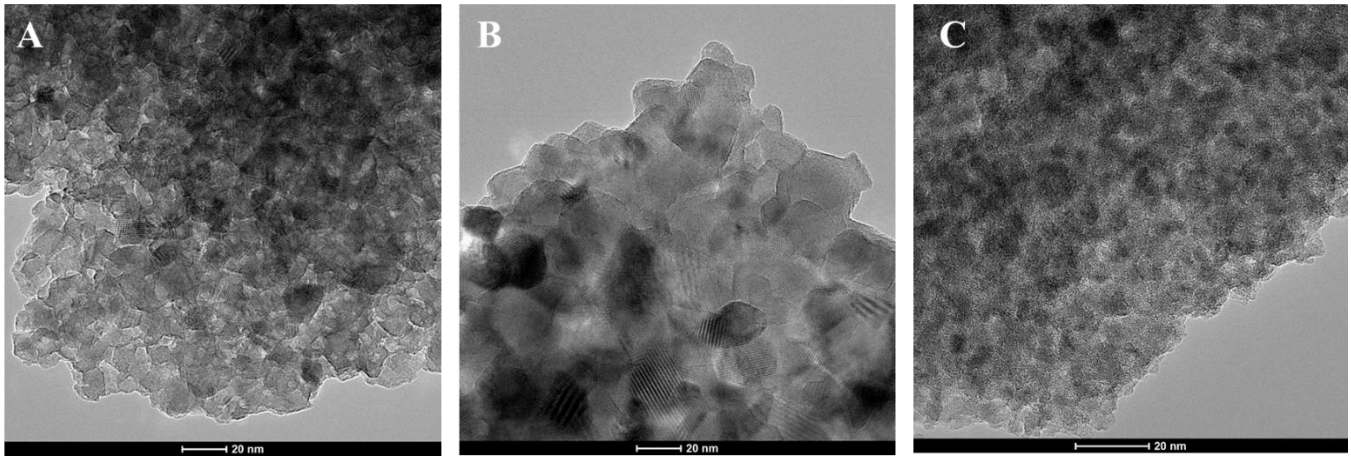

Figure 5.4. Transmission electron microscopic image of (A) BT-0, 500 °C calcined white sample, (B) BT-4, 500 °C hydrogenated sample, and (C) *in situ* B. TiO_2 material.

High resolution TEM images show that the materials are anatase crystalline phase of TiO_2. Figure 5.5 (A) is the black titania synthesized from the mesoporous titanium dioxide (BT-4) which is highly crystalline. However, the *in situ* black TiO_2 (figure 5.5. B) has comparatively low crystallinity and also represent the anatase phase. The small crystallite size of the *in situ* material is also in very good agreement with the XRD results.

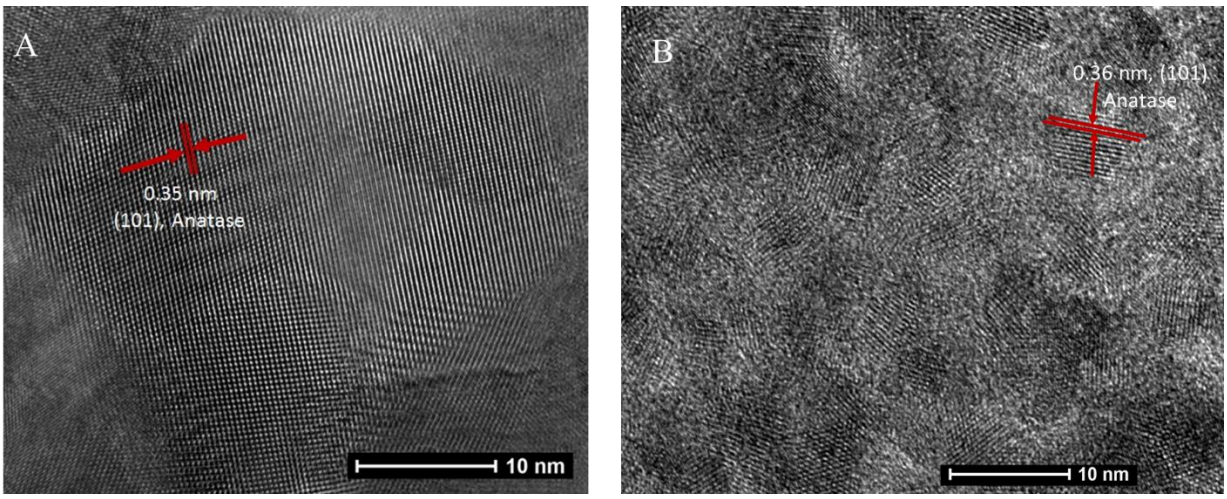

Figure 5.5. HR-TEM image of (A) BT-0, and (B) *in situ* B. TiO_2.

5.4.3. Photocatalytic dye degradation

The photochemical performances of the synthesized black titania nanomaterials were studied by measuring the percent degradation of the model dye methylene blue (MB) in aqueous solution under visible light and at room temperature. The major absorption peak of methylene blue dye is around 668 nm. The percent degradations of the MB dye with different samples are tabulated in Table 5.1.

Table 5.1. Photocatalytic degradation result of the methylene blue dye with different materials.

Material	**% Degradation of MB**
BT-0	64%
BT-4	64%
In situ B. TiO_2	93%

Figure 5.6 shows the UV-vis spectra of the dye after reaction with different materials. Among all the materials, *in situ* black titania shows the highest degradation (93%) after 4 h visible light irradiation. Mesoporous titanium dioxide (BT-0) and the 500 °C hydrogenated materials showed similar activity.

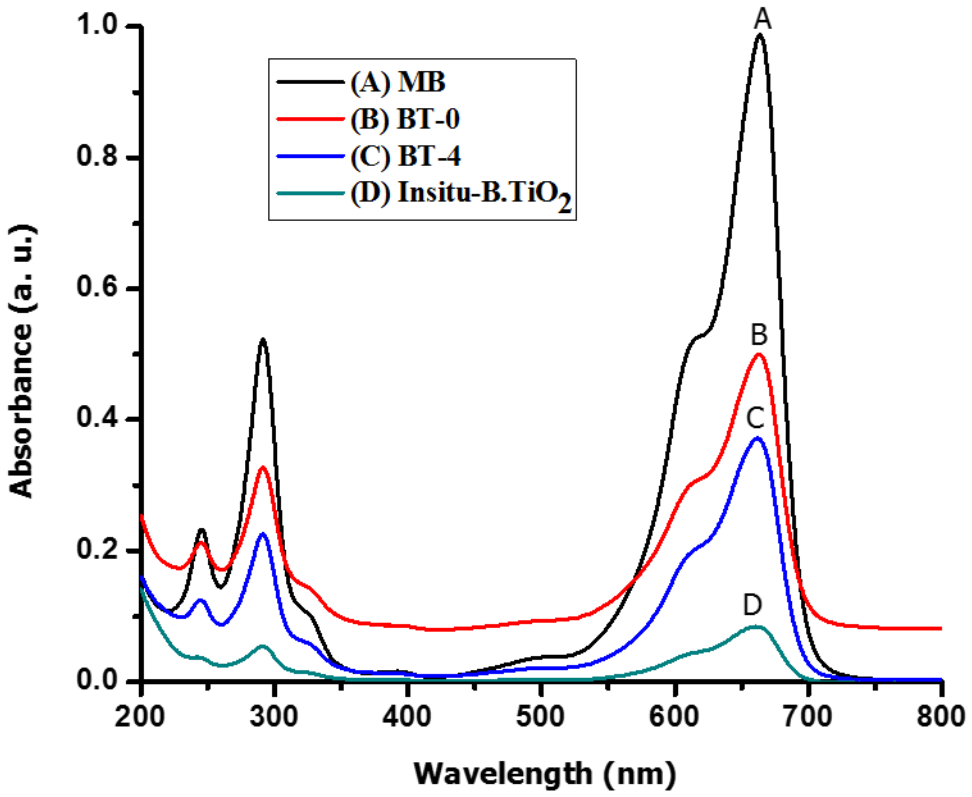

Figure 5.6. UV-Vis spectra of methylene blue after 4 h visible light irradiation with different material: **(A)** Methylene blue (MB) dye, **(B)** MB with BT-0, **(C)** MB with BT-4, and **(D)** MB with *in situ* B. TiO_2.

5.5. Discussion

In this study, anatase phase black TiO_2 nanomaterial was synthesized by a facile hydrogenation process under atmospheric pressure. Initially, mesoporous TiO_2 was prepared by an inverse templated sol-gel method. The mesoporous material was then calcined under air at 500 °C for 4 h, followed by hydrogenation at different temperatures for 48 h. The black TiO_2 nanomaterials are normally prepared under high pressure hydrogenation for an extended period. After 48 h of hydrogenation at 300, 400, and 450 °C the sample became brown, gray, or dark

gray color, which means they partially absorb the visible light. At 500 °C hydrogenation, after 48 h the sample become black in color. Therefore, 500 °C is the lowest temperature to make black titanium dioxide at atmospheric pressure. All these hydrogenated materials lost their mesoporosity due to a long hydrogenation process (48 h). The mesoporous materials are very active compared to their nonporous counterpart. Hence, in this experiment, the mesoporous TiO_2 (BT-0) also exhibited good photocatalytic activity. However, the hydrogenated black titanium dioxide (BT-4) show similar performance as the mesoporous titania, although the material is no longer mesoporous. This catalytic performance can be explain by high solar absorption of the black material.

The *in situ* black TiO_2 was obtained by calcining the as-synthesized material under H_2/Ar gas mixture, lost their mesostructure. The inverse micelle is a soft templated method and the mesoporosity obtained from the intra-particle voids. Poyraz et al. explained the mechanism of the formation of mesoporosity of the materials.[24] However, in the *in situ* synthesis process due to the presence of H_2/Ar mixture instead of air, the normal calcination process hindered and the material lost their mesostructured, and result smaller crystallite size. In the *in situ* calcination, when the as-synthesized film like material is heated under H_2 and Ar mixture, during the surfactant removal step hydrogen can easily enter the crystal lattice. Thus hydrogen can make the intermediate electronic state between the valence band and conduction band, which extends the solar absorption and enhances the photocatalytic activity of the materials.

Commercial titanium dioxide photocatalyst (P25) is a mixture of anatase and rutile phase of the material (80% anatase and 20% rutile). The X-ray diffraction pattern of the synthesized materials suggests the formation of the active anatase phase of the materials. From TEM, the calculated d-spacings of the materials are close to 0.35 nm which are representative for the

anatase (101) plane. The TEM image shows that the *in situ* materials have more disordered surfaces, and the crystallite size is also smallest among all other synthesized materials. Therefore, the decreased crystallinity, smaller crystallite size, and the disordered surface have made the *in situ* material best in catalytic performance.

5.6. Conclusion

In conclusion, black titanium dioxide nanomaterial has been successfully synthesized by both *in situ* and post treatment method. The structure (active anatase phase) and morphology of the synthesized titanium dioxide were confirmed by X-ray diffraction and transmission electron microscopy. The *in situ* black TiO_2 showed excellent photocatalytic performance in dye degradation (environmental pollution removal). For this study, additional characterization is needed to confirm the structure activity relation and to check the origin of the active sites. X-ray photoelectron spectroscopy (XPS) and electron paramagnetic resonance (EPR) need to be done to check the Ti^{3+} ions in the sample. ESR spectroscopy is required to check the oxygen vacancies in the materials. Scanning electron microscopy (SEM) will be done to see the morphology of the materials. The initial adsorption amount also need to measure before the degradation starts. After complete characterization and understanding the origin of the activity, the material could be an outstanding advanced material for various practical applications.

Reference list

(1) Ma, Y.; Wang, X.; Jia, Y.; Chen, X.; Han, H.; Li, C. *Chem. Rev.* **2014**, *114*, 9987.

(2) Li, R.; Weng, Y.; Zhou, X.; Wang, X.; Mi, Y.; Chong, R.; Han, H.; Li, C. *Energy Environ. Sci.* **2015**, *8*, 2377.

(3) Lai, C. W.; Juan, J. C.; Ko, W. B.; Bee Abd Hamid, S. *Int. J. Photoenergy* **2014**, *2014*.

(4) Chen, X.; Selloni, A.; ACS Publications: 2014.

(5) Dette, C.; Pérez-Osorio, M. A.; Kley, C. S.; Punke, P.; Patrick, C. E.; Jacobson, P.; Giustino, F.; Jung, S. J.; Kern, K. *Nano Lett.* **2014**, *14*, 6533.

(6) Deng, L.; Wang, S.; Liu, D.; Zhu, B.; Huang, W.; Wu, S.; Zhang, S. *Catal. Lett.* **2009**, *129*, 513.

(7) Zheng, Z.; Huang, B.; Qin, X.; Zhang, X.; Dai, Y.; Whangbo, M.-H. *J. Mater. Chem.* **2011**, *21*, 9079.

(8) Chen, X.; Burda, C. *J. Am. Chem. Soc.* **2008**, *130*, 5018.

(9) Chen, X.; Liu, L.; Peter, Y. Y.; Mao, S. S. *Science* **2011**, *331*, 746.

(10) Liu, N.; Schneider, C.; Freitag, D.; Hartmann, M.; Venkatesan, U.; Müller, J.; Spiecker, E.; Schmuki, P. *Nano Lett.* **2014**, *14*, 3309.

(11) Chen, X.; Shen, S.; Guo, L.; Mao, S. S. *Chem. Rev.* **2010**, *110*, 6503.

(12) Chen, X.; Li, C.; Grätzel, M.; Kostecki, R.; Mao, S. S. *Chem. Soc. Rev.* **2012**, *41*, 7909.

(13) Wang, Z.; Yang, C.; Lin, T.; Yin, H.; Chen, P.; Wan, D.; Xu, F.; Huang, F.; Lin, J.; Xie, X. *Energy Environ. Sci.* **2013**, *6*, 3007.

(14) Hoa, N. T. Q. *Int. J. Nanotechnol.* **2015**, *12*, 426.

(15) Nishikawa, T.; Nakajima, T.; Shinohara, Y. *J. Mol. Struc. THEOCHEM* **2001**, *545*, 67.

(16) Wu, Q.; Zheng, Q.; van de Krol, R. *J. Phys. Chem. C* **2012**, *116*, 7219.

(17) Livraghi, S.; Paganini, M. C.; Giamello, E.; Selloni, A.; Di Valentin, C.; Pacchioni, G. *J. Am. Chem. Soc.* **2006**, *128*, 15666.

(18) Zhou, W.; Li, W.; Wang, J.-Q.; Qu, Y.; Yang, Y.; Xie, Y.; Zhang, K.; Wang, L.; Fu, H.; Zhao, D. *J. Am. Chem. Soc.* **2014**, *136*, 9280.

(19) Wei, S.; Wu, R.; Xu, X.; Jian, J.; Wang, H.; Sun, Y. *Chem. Eng. J.* **2016**, *299*, 120.

(20) Wang, C.-C.; Chou, P.-H. *Nanotechnology* **2016**, *27*, 325401.

(21) An, H.-R.; Park, S. Y.; Kim, H.; Lee, C. Y.; Choi, S.; Lee, S. C.; Seo, S.; Park, E. C.; Oh, Y.-K.; Song, C.-G. *Sci. Rep.* **2016**, *6*.

(22) Teng, F.; Li, M.; Gao, C.; Zhang, G.; Zhang, P.; Wang, Y.; Chen, L.; Xie, E. *Appl. Catal. B Environ.* **2014**, *148*, 339.

(23) Lepcha, A.; Maccato, C.; Mettenbörger, A.; Andreu, T.; Mayrhofer, L.; Walter, M.; Olthof, S.; Ruoko, T.-P.; Klein, A.; Moseler, M. *J. Phys. Chem. C* **2015**, *119*, 18835.

(24) Poyraz, A. S.; Kuo, C.-H.; Biswas, S.; King'ondu, C. K.; Suib, S. L. *Nat. Commun.* **2013**, *4*.

(25) Song, W.; Poyraz, A. S.; Meng, Y.; Ren, Z.; Chen, S.-Y.; Suib, S. L. *Chem. Mater.* **2014**, *26*, 4629.

(26) Biswas, S.; Dutta, B.; Mullick, K.; Kuo, C.-H.; Poyraz, A. S.; Suib, S. L. *ACS*

Catal. **2015**, *5*, 4394.

(27) Mosa, I. M.; Biswas, S.; El-Sawy, A. M.; Botu, V.; Guild, C.; Song, W.; Ramprasad, R.; Rusling, J. F.; Suib, S. L. *J. Mater. Chem. A* **2016**, *4*, 620.

(28) Luo, Z.; Poyraz, A. S.; Kuo, C.-H.; Miao, R.; Meng, Y.; Chen, S.-Y.; Jiang, T.; Wenos, C.; Suib, S. L. *Chem. Mater.* **2014**, *27*, 6.

(29) Genuino, H. C.; Hamal, D. B.; Fu, Y.-J.; Suib, S. L. *J. Phys. Chem. C* **2012**, *116*, 14040.

Future Work

The development of catalyst materials for different applications is a field of great interest. In this thesis, advanced nanomaterials have been developed and reported for environmental and energy applications. The design of these materials is generic and has been applied for the particular type of reactions. Optimization of synthesis method and different physicochemical properties can provide a wide class of materials for various applications. Thus, as a future perspective, the developed materials can be further optimized to improve the physicochemical properties (surface area, porosity, crystallinity) to tune the catalytic applications. Apart from heterogeneous catalysis, the developed materials could also be potential materials for electronic, optical, and biomedical related specific applications.

The inverse micelle templated single step synthesis process of the developed mesoporous solid acid material could be a unique synthetic approach for the synthesis of various sulfate containing super acids (such as sulfated titanium oxide, tin oxide, and mixed oxides). The unique facet of the materials is a high number of acid sites, uniform porosity, and two types (Brønsted and Lewis) of acid sites in the material. Besides biodiesel production, the material could be a promising candidate for different acid catalyzed reactions (short chain alkane isomerism, esterification, glucose conversion). Synthesized black titanium dioxide nanomaterial showed a low band gap and good photocatalytic activity under visible light irradiation. The mesoporosity of the black titanium dioxide nanomaterials is a big challenge. However, the mesoporosity of our synthesized materials can be retained by a slow hydrogenation process and heating rate. For the long-term perspective, developing methodologies for water splitting for hydrogen generation is

highly desirable to meet the increasing demand for clean energy. Therefore, mesoporous black titanium dioxide material and the carbon based hybrid materials could be a solution for future energy problems. Since carbon nanotube based synthesized hybrid materials showed promising activity, the use of framework doped carbon nanotube or reduced graphene oxide could enhance the catalytic performance. Synthetic technique for the artificial antibody, the molecular imprinting technique, could be used to synthesize nanomaterials for target specific applications, such as sensors, solid phase extractions, and medical diagnosis.

Finally, this thesis highlights the design, synthesis and applications of various active, low-cost, and stable advanced nanomaterials for environmental and energy related applications. Moreover, these materials are versatile as they can be applied towards the photocatalytic and portable energy storage devices.